ISTANBUL TECHNICAL UNIVERSITY ★ GRADUATE SCHOOL OF SCIENCE ENGINEERING AND TECHNOLOGY

HIGH TEMPERATURE WEAR PERFORMANCE OF ALLOYED AND CARBIDE REINFORCED STELLITE 12 COATINGS

Ph.D. THESIS

Amir MOTALLEBZADEH
(506102401)

Department of Metallurgical and Materials Engineering

Metallurgical and Materials Engineering Program

Thesis Advisor: Prof. Dr. Hüseyin ÇİMENOĞLU
Thesis Co-Advisor: Assoc. Prof. Dr. Erdem ATAR

SEPTEMBER 2015

İSTANBUL TEKNİK ÜNİVERSİTESİ ★ FEN BİLİMLERİ ENSTİTÜSÜ

ALAŞIMLANDIRILMIŞ VE KARBÜR TAKVİYELİ STELLITE 12 KAPLAMALARIN YÜKSEK SICAKLIKTA AŞINMA DAVRANIŞI

DOKTORA TEZİ

Amir MOTALLEBZADEH
(506102401)

Metalurji ve Malzeme Mühendisliği Anabilim Dalı

Metalurji ve Malzeme Mühendisliği Programı

Tez Danışmanı: Prof. Dr. Hüseyin ÇİMENOĞLU
Tez Eş Danışmanı: Doç. Dr. Erdem ATAR

EYLÜL 2015

Amir Motallebzadeh, a **Ph.D.** student of ITU **Graduate School of Science, Engineering and Technology** student ID **506102401**, successfully defended the **dissertation** entitled "**HIGH TEMPERATURE WEAR PERFORMANCE OF ALLOYED AND CARBIDE REINFORCED STELLITE 12 COATINGS**", which he prepared after fulfilling the requirements specified in the associated legislations, before the jury whose signatures are below.

Thesis Advisor : **Prof. Dr. Hüseyin ÇİMENOĞLU** ....
Istanbul Technical University

Co-advisor : **Assoc. Prof. Dr. Erdem ATAR** ....
Gebze Technical University

Jury Members : **Prof. Dr. Eyüp Sabri KAYALİ** ....
Haliç University

Prof. Dr. Sakin ZEYTİN ....
Sakarya University

Prof. Dr. Lütfi ÖVEÇOĞLU ....
Istanbul Technical University

Assoc. Prof. Dr. Uğur MALAYOĞLU ....
Dokuz Eylül University

Assoc. Prof. Dr. Murat BAYDOĞAN ....
Istanbul Technical University

Date of Submission : 14 September 2015
Date of Defense : 5 November 2015

To my beloved wife and my family,

FOREWORD

I wish to express special gratitude to my advisors Prof. Dr. Hüseyin ÇİMENOĞLU and Assoc. Prof. Dr. Erdem ATAR for their invaluable advice, support, inspiration and excellent guidance they have given me throughout the completion of my study.

Financial support provided to this project by the Scientific and Technological Research Council of Turkey (under the Grant number of 212M035) and Istanbul Technical University (under the Grant number of 37062) is gratefully acknowledged.

I also would like to thank Assoc. Prof. Dr. Murat BAYDOĞAN for his advice and contribution during my graduate studies.

Special acknowledgment is given to Mr. Hüseyin SEMERCİ, general manager of Şenmak Makina San.Tic.A.Ş, for the technical support and allowing me to use their PTA welding facilities.

I would like to thank M.Sc. Farid SIYAHJANI, M.Sc. Dilek TEKER AYDOĞAN, Dr. Onur MEYDANOĞLU and M.Sc. Faiz MUHAFFEL who as good friends were always willing to help me.

My parents, Fariba and Aliakbar, receive my deepest gratitude for their support and patience during my studies.

I would like to thank my wife, Saman, for her understanding and love during the past few years. Her support and encouragement was in the end what made this dissertation possible.

September 2015 — Amir Motallebzadeh (M.Sc)

TABLE OF CONTENTS

Page

ABBREVIATION

CVD	**:** Chemical Vapor Deposition
DC	**:** Direct Current
EDX	**:** Energy Dispersive X-ray
FCC	**:** Face-Centered Cubic
GMAW	**:** Gas Metal Arc Welding
GTAW	**:** Gas Tungsten Arc Welding
HAZ	**:** Heat Affected Zone
HVOF	**:** High Velocity Oxygen Fuel
IBAD	**:** Ion Beam Assisted Deposition
MMC	**:** Metal Matrix Composite
PTA	**:** Plasma Transferred Arc
PVD	**:** Physical Vapor Deposition
SEM	**:** Scanning Electron Microscopy
XRD	**:** X-Ray Diffractometer

LIST OF TABLES

LIST OF FIGURES

Page

HIGH TEMPERATURE WEAR PERFORMANCE OF ALLOYED AND CARBIDE REINFORCED STELLITE 12 COATINGS

SUMMARY

The aim of this study is to investigate the influence of the addition of molybdenum and nickel alloying elements and also WC/W_2C, TiC and Cr_7C_3 reinforcement hard particles on the wear behavior of Stellite 12 coatings deposited by the plasma transferred arc (PTA) method. Single layer coatings were deposited on AISI 4140 steel under constant PTA parameters. Present study mainly focused on room and high temperatures wear behavior of the coatings produced from the feedstocks prepared by mixing Stellite 12 powder with 2, 6 and 10 (wt%) of Mo and Ni powders and 2, 6 and 10 (vol%) WC/W_2C, TiC and Cr_7C_3 particles separately.

Phase analysis and microstructure of the coatings were examined by X-ray diffractometer (XRD) and field emission scanning electron microscope equipped with energy dispersive X-ray (EDX) spectrometer. Vickers microhardness measurements were performed on the surfaces of examined coatings. Furthermore, depth sensing indentation test was conducted on the matrices of Mo and Ni added samples. Dry sliding wear behavior of deposited coatings were determined on a ball-on-disc type tribometer by rubbing alumina ball under normal load of 3 N at RT, 300, 500 and 700 ºC. Sliding speed and distance were kept constant at 0.1 m/s and 500 m, respectively. For determining wear mechanism of tested samples, their worn surfaces were examined by EDX equipped SFEG SEM and Raman spectroscopy.

The microstructural analyses of PTA deposited Stellite 12 revealed that the coating was composed of Cr-rich carbides Co/W-rich complex carbides and intermetallics embedded in primary α-Co solid solution dendritic matrix.

Addition of Mo up to 10 wt% induced different solidification characteristics in the microstructure evolution of the PTA deposited Stellite 12 coating as volume fraction of Co/Mo-rich complex carbide and intermetallic compounds increased and formation of Cr_7C_3 was suppressed. Increasing volume fraction of Co/Mo-rich complex carbide and intermetallic compounds and solid solution hardening effect of Mo dissolved in the matrix contribute to increasing hardness of Stellite 12 coating from 490 ± 10 HV_2 to 621 ± 8 HV_2 upon addition of 10 wt% Mo.

Microstructural analyses showed that added Ni into Stellite 12 totally dissolved in Co-rich solid solution matrix without changing the type of microstructural constituents. Addition of Ni element promoted stabilization of α-Co phases and increased its volume fraction in the microstructure at room temperature which led to reduction in hardness of examined coating. The hardness value decreases from 490 ± 10 HV_2 to 458 ± 5 HV_2 as the Ni content increases up to 10 (wt%).

Full or partial melting of WC/W_2C particles during PTA deposition process and enrichment of the melt pool in W and C resulted in development of more Co/W-rich complex carbides (Co_3W_3C and Co_6W_6C) and intermetallic (Co_3W) compounds in

microstructure and also dissolution of W in Co-rich solid solution matrix. Generation of more Co/W-rich compound in addition to Cr-rich carbides in the microstructure of the Stellite 12+WC/W_2C coating contribute to increasing hardness as the it reaches 642±5 HV_2 in 10 vol% WC/W_2C containing Stellite 12 coating.

Microstructural surveys showed that when TiC was added into the Stellite 12, the basic dendritic matrix and eutectic solidification features of deposited coatings was maintained almost the same but volume fraction of constituents formed during solidification was altered. Undissolved TiC particles in the melt pool act as suitable sites for nucleation of eutectic compounds during solidification and therefore contributed to the refinement of dendritic matrix and development of more eutectic compounds in microstructure which led to increase in hardness of TiC containing coatings.

In the case of Stellite 12+Cr_7C_3 coatings, microstructural investigations indicate that total of Cr_7C_3 particles were completely melted and dissolved in Stellite 12 melt pool due to its lower melting point. Enrichment of melting pool in Cr and C contributed to development of Cr_7C_3 and $Cr_{23}C_6$ in the microstructure. Formation of more Cr-rich carbide resulted in enhancement of hardness in Stellite 12+Cr_7C_3 coatings and it reaches to 636±6 HV_2 upon addition of 10 vol% Cr_7C_3.

SEM micrographs taken from the worn surfaces of all examined coatings indicated that at RT (25 °C) and 300 °C the wear progressed by the plasticity dominant mechanism. At testing temperature of RT, the worn surfaces of the coatings were characterized by accumulated plastic deformation resulting from cyclic sliding contact. The sliding action of the Al_2O_3 ball at 300 °C imposed plastic deformation along with scratches aligned in the direction of motion on the worn surfaces of the coatings. Since hardness play a crucial role on tribological performance of Stellite alloys at RT and moderate temperature, enhancement in wear resistance of Stellite 12+Mo, Stellite 12+WC/W_2C, Stellite 12+TiC and Stellite 12+Cr_7C_3 coatings at RT and 300 °C can be attributed to the formation and increasing volume fraction of eutectic carbides and/or intermetallic compounds upon addition of alloying element or reinforcement particles. Furthermore, work hardening of cobalt-rich solid solution matrix at the contact surface during wear testing contributed to the wear resistance at RT. With increasing testing temperature from RT to 300 °C, remarkable decreases in wear resistance of examined coating was observed which can be related to reduction in the work hardening rate and mechanical strength and/or easy destruction of thin and less adherent oxide films covering the worn surfaces. Addition of Ni in to Stellite 12 increased the wear loss of examined coatings at RT and 300 °C. The reduction of wear resistance in Ni containing examined coatings can be attributed to decrease of work hardening rate, hardness and volume fraction of hard carbides or intermetallic compounds in microstructure.

Oxidative mechanism was identified as the main wear mechanism of examined coatings at 500 and 700 °C. SEM analyses indicated that formation of protective and continuous oxide film on won surfaces at elevated temperature reduced direct contact of sliding surface and alumina ball and improved the wear resistance in comparison with testing temperature of 300 °C. Raman spectroscopy signals of the Stellite 12 coating worn at 500 and 700 °C corresponded to CoO and mainly a mixture of Co_3O_4 and Cr_2O_3, respectively. Therefore good tribological characteristics of Cr_2O_3 contributed to reduction of weal loss when testing temperature increased from 500 to

700 °C. Under oxidation dominated wear mechanism, the Stellite 12+Mo coating exhibited better wear resistance than the Stellite 12 coating.

Addition of Mo in to Stellite 12 coating favored formation of Cr_2O_3 and $CoMoO_4$ at 500 and 700 °C respectively. Formation of Cr_2O_3 and $CoMoO_4$ can be attributed to the dissolution of Mo in solid solution matrix and development of more $Cr_{23}C_6$ in the microstructure. Increasing testing temperature from 500 to 700 °C led to decrease in wear loss of examined coatings. Protective and lubricious nature of $CoMoO_4$ complex oxide efficiently decreased the wear loss of molybdenum containing Stellite 12 coatings at 700 °C.

Addition of Ni into the Stellite 12 coating did not caused significant changes in wear loss of examined coatings tested at 500 and 700 °C. Although at elevated testing temperature increasing Ni contents can favor development of oxide films on the worn surfaces but decreasing hardness and consequently increasing plastic deformation of zone beneath the sliding ball led to break-down and removal of oxide films formed on the surfaces.

The wear tests results at 500 and 700 °C showed that addition of WC/W_2C into Stellite 12 improved wear resistance. The oxide film formed on the worn surface of examined coating tested at 500 °C was composed of mainly Co_3O_4, Cr_2O_3 and also WO_3. The dissolution of W atom in Co-rich solid solution matrix contributed to the development of protective Cr_2O_3 and WO_3 on the worn surface. Comparing with testing temperature of 500 °C, wear tests conducted at 700 °C was accompanied by generation of $CoWO_4$ complex oxide on worn surfaces which played crucial role on reduction of wear loss. It should be noted that oxidation and consequently volatilization of WC/W_2C reinforcement particles at 700 °C led to their decomposition and fragmentation during sliding wear.

In the case of Stellite 12+TiC coatings while addition of 2 and 6 vol% TiC improved the wear resistance at 500 °C, significant diffidence was not observed between wear loss of Stellite 12+10 vol % TiC coating and Stellite 12 coating. Introducing TiC particles reduced the wear resistance of Stellite 12 coating at 700 °C as wear loss increase more than two times upon addition of 10 vol % TiC. The oxide film formed on worn surface of Stellite 12+10 vol% TiC coating tested at 500 and 700 °C was composed of CoO and mainly Co_3O_4, respectively. Higher hardness of 2 and 6 vol% containing TiC coatings was beneficial in reducing plastic deformation of zone beneath the sliding ball and preventing break-down and removal of oxide films formed on worn surfaces. However in the case of Stellite 12+10 vol% TiC coating formation of more Cr-rich carbides and decreasing volume fraction of Co-rich solid solution matrix inhibited the development of continuous protective CoO film on the worn surface. Also due to formation of more Cr-rich carbides, chromium atoms do not afford quite as much protection as might be expected if they were free to migrate from dendritic solid solution matrix to the surface and form a continuous Cr_2O_3 layer at 700 °C. Therefore introducing more TiC particles into Stellite 12 was accompanied by reduction of wear resistance at 700 °C.

The results of wear tests at 500 and 700 °C indicated that introducing Cr_7C_3 particles up to 10 vol% resulted in increasing wear loss of examined coatings. Addition of 10 vol% Cr_7C_3 remarkably increased wear loss at 500 °C and Stellite 12+Cr_7C_3 coatings exhibited worse wear performance than Stellite 12 coatings at 700 °C. Deficiency in development of continuous CoO and adequate Cr_2O_3 on the worn surfaces tested at 500 and 700 °C were determined as the main reasons of increment in wear loss.

ALAŞIMLANDIRILMIŞ VE KARBÜR TAKVİYELİ STELLITE 12 KAPLAMALARIN YÜKSEK SICAKLIKTA AŞINMA DAVRANIŞI

ÖZET

Adhesif, abrazif veya korozif ortamlar ile temas halinde olan yüzeylerin aşınma direnci ve sertliklerini arttırmak konusunda artan ilgi, koruyucu kaplamalar oluşturmak için çeşitli yöntemlerin gelişimine ilham kaynağı olmuştur. Plasma Transferred Arc (PTA) kaynak işlemi yüksek enerji yoğunluğu, yüksek çökelme hızı ve düşük ısı girişi sayesinde, çok çeşitli metal tabanlı malzemelerin üzerine erimiş bağlantı ile kalın metalik kaplamalar üretilmesine olanak sağlayan yeni bir kaplama yöntemidir.

PTA kaynak yönteminde, çok-bileşenli sert dolgu alaşımları (Co-, Ni- veya Fe-esaslı alaşımlar) nispeten yumuşak malzemelerin yüzeyleri üzerinde kaplana bilir. Diğer Ni- ve Fe- esaslı sert kaplama alaşımları ile karşılaştırıldığında, Co-esaslı sert kaplama alaşımları havacılık, gaz türbinleri, enerji santralleri, kimya ve petrokimya sanayinde kullanılan parçaların aşınma, korozyon ve ısı direnci özelliklerinin iyi bir kombinasyonunu gerektiren bileşenlerin korunması için uygundur. Stellite alaşımı, en popüler kobalt esaslı sert kaplama grubu, yüksek sertlik ve mukavemet, üstün adhesif ve abrasif aşınma direnci ve mükemmel kavitasyon-erozyon direnci gibi mekanik ve tribolojik özelliklerin benzersiz bir bileşimini gösterir. Stellite alaşımında temel unsur olan krom ağırlıkça %20-30 aralığında korozyon direncini arttırmak, Cr-zengin karbürleri oluşturmak ve katı çözelti güçlendirmesi için ilave edilir. Ayrıca, tungsten veya molibden ve bir miktar (ağırlıkça < %3) karbon da ihtiva edebilir. Stellite alaşımlarının mekanik ve tribolojik özelliklerinin çoğu, kobaltın doğal kristalografisinden, krom, tungsten ve molibdenin katı çözelti sertleştirme etkisinden ve karbür veya intermetalik bileşenlerin oluşmasından ortaya çıkmaktadır. Stellite sert kaplama alaşımları arasında, nominal bileşimi ağırlıkça % Co–29.5Cr–8.5W–1.65C olan Stellite 12, yağlanmamış çalışma koşulları altında 700 $^{\circ}$C'ye kadar iyi bir aşınma ve oksidasyon direncine sahip olduğundan farklı uygulamalar için oldukça çekicidir. Stellite alaşımların başarısına rağmen, servis ömrünün ve yüksek yükler ve/veya sıcaklıklar altında performansının daha da artması amacıyla özelliklerini daha da geliştirmek için bazı girişimlerde bulunulmuştur. Bu bağlamda, alaşım elementleri ve takviye parçacıkların eklenmesinin Stellite 6 ve düşük karbonlu Stellite alaşımının sürtünme ve abrasif aşınma davranışı üzerindeki etkisi oda sıcaklığında incelenmiş ve ümit verici gelişmeler bildirilmiştir. Fakat eklenen alaşımların ve sert parçacıklarla güçlendirilmiş Stellite 12 kaplamaların yüksek sıcaklıklardaki tribolojik davranışı hakkında bilgi eksikliği bulunmaktadır.

Bu çalışmanın amacı, oda sıcaklığında ve yüksek sıcaklıkta Stellite 12 kaplamaların aşınma davranışına molibden ve nikel alaşım elementlerinin ve ayrıca WC/W_2C, TiC ve Cr_7C_3 takviye sert parçacıkların ilave etkisini araştırmaktır. Stellite 12 tozu Mo, Ni tozları ve WC/W_2C, TiC ve Cr_7C_3 parçacıklar ile besleme malzemeleri yapmak

için ayrı ayrı karıştırılmıştır ve daha sonra tek bir tabaka halinde ve sabit kaplama şartlarında PTA kaynak makinesi kullanılarak AISI 4140 çelik üzerine kaplanmıştır. Mo, Ni ağırlıkça % 2, 6 ve 10, WC/W_2C, TiC ve Cr_7C_3 hacimce %2, 6 ve 10 oranlarında eklenmiştir.

Kaplamaların mikroyapı ve faz analizleri X-ışınları kırınımı ve alan-emisyonlu taramalı elektron mikroskobu ve ona bağlı enerji dağılımlı X-ışınları spektrometresi ile incelenmiştir. Vickers sertlik ölçümleri incelenen kaplama yüzeyi üzerinde gerçekleştirilmiştir. Ayrıca, derinlik algılama girinti testi Mo ve Ni ekli numunelerin matrisleri üzerinde yapılmıştır. Kaplamaların kuru ortamda sürtünmeli aşınma davranışı ball-on-disc tipi tribometre ile alümina top sürtünmesi kullanılarak 3 N'luk yük altında sırasıyla oda sıcaklığında, 300, 500 ve 700 ºC'de incelenmiştir. Sürtünme hızı ve mesafesi sırasıyla 0,1 m/s ve 500 m' de sabit tutulmuştur. Test numunelerinin aşınma mekanizmasını anlamak için aşınmış yüzeyler EDS donanımlı SFEG SEM ve Raman spektrometresi ile incelenmiştir.

PTA yöntemi ile kaplanan Stellite 12'nin mikroyapısal analizi, primer α-Co katı çözelti dentritik matriks içine gömülü kromca zengin karbürler, Co/W zengin kompleks karbürler ve intermetaliklerin oluşturduğu bir kaplamayı göstermiştir.

Ağırlıkça %10' a kadar Mo eklenmesiyle PTA yöntemi ile yüzeyde oluşturulan Stellite 12 kaplamaların farklı katılaşma karakteristikleri mikro yapıda değişikliğe neden olurken Co/Mo-zengin kompleks karbür ve intermetalik bileşenlerin hacimsel oranı artmış ve Cr_7C_3 oluşması önlenmiştir. Tungsten'e göre atomik ağırlığı daha hafif ve atomik boyutu daha küçük olan molibden ayrıca ergime havuzundaki karbon içeriğinin tükenmesi ve Mo içeriğinin artması mikroyapı içinde Cr_7C_3 yerine Co/Mo-zengin bileşikler ve $Cr_{23}C_6$' nın oluşumunu teşvik eden kritik bir rol oynamaktadır. Co/Mo-zengin kompleks karbür ve intermetalik bileşiklerin hacimsel oranının artması ve matrix içinde çözünen Mo'nin katı çözelti sertleştirme etkisi, Stellite 12 kaplamaların sertlik değerlerinin ağırlıkça %10' a kadar Mo ilavesi ile 490 ± 10 HV_2'den 621±8 HV_2'ye artmasına katkı sağlamıştır.

Mikro yapısal analizler göstermiştir ki, Stellite 12 içine eklenen Ni, Co-zengin katı çözelti matrix içinde mikro yapısal bileşenlerin türünü değiştirmeden tamamen çözünmüştür. Ni elementinin eklenmesi ile α-Co fazının kararlılığı artmış ve oda sıcaklığında mikro yapıdaki hacimsel oranı yükselmiştir ki bu durum incelenen kaplamanın sertliğinde bir azalmaya sebep olmuştur. Ni içeriğinin ağırlıkça %10'a kadar yükselmesi ile sertlik değerleri 490±10 HV_2'den 458±5 HV_2' ye düşmüştür. Stellite 12 kaplamaların nikel ilavesi ile dayanımının zayıflaması nedeni katı çözelti matrisinin mekanik yükler altındaki matriks deformasyonu FCC→HCP martensitik faz dönüşümü yerine ikizlenme veya kayma ile gerçekleşmesi olabilir. Ayrıca Ni eklenmiş kaplamalarda geliştirilen Cr zengin karbürler ve Co/W zengin intermetalik bileşiklerin düşük hacimsel oranı, sertliğin düşmesine yol açar.

PTA kaplama işlemi sırasında WC/W_2C parçacıkların tamamen veya kısmen ergimesi ve ergitme havuzu içindeki W ve C zenginleştirmesi yapı içinde daha fazla Co/W zengin kompleks karbürlerin (Co_3W_3C ve Co_6W_6C) ve intermetalik (Co_3W) bileşiklerin geliştirilmesi hem de Co zengin katı çözelti matriks içinde W' ın çözünmesi ile sonuçlanmıştır. Buna ek olarak, eriyik havuzu içinde kısmen ergimiş WC/W_2C parçacıkları dentritik matrisin çekirdeklenme ve katılaşma paternlerindeki değişikliklerden dolayı ötektik bileşiklerin gelişimine katkı sağlar. Stellite 12+WC/W_2C kaplamaların mikroyapısında bulunan Cr zengin karbürlere ek oarak Co/W bakımından daha zengin bileşiğin üretimi sertliğin yükselerek hacimce %10

WC/W_2C içeren Stellite 12 kaplamalarda 642±5 HV_2'ye kadar ulaşmasına katkıda bulunmuştur.

Mikroyapısal araştırmalar, Stellite 12 içerisine TiC eklendiğinde kaplamanın temel dendritik matris ve ötektik katılaşma özelliklerinin hemen hemen aynı şekilde korunduğunu fakat katılaşma sırasında oluşan bileşenlerin hacimsel oranlarının değiştiğini göstermiştir. Kobalt esaslı alaşımlar içindeki TiC' ün yüksek termal kararlılığı ve çok sınırlı çözünürlüğü nedeniyle, PTA işlemi sırasında eriyik havuzu içinde kolayca ayrışmaz ve çözünmez. Eriyik havuzu içinde çözünmeyen TiC parçacıkları katılaşma sırasında ötektik bileşenlerin çekirdeklenmesi için uygun bir yer görevi görür, bu nedenle, dentritik matrisin arıtılmasına ve yapı içerisinde daha fazla ötektik bileşenin gelişimine katkı sağlayarak TiC içeren kaplamaların sertlik değerlerinin artmasına sebep olur.

Stellite 12+Cr_7C_3 kaplamalara ait mikroyapısal araştırmalar göstermektedir ki, düşük ergime sıcaklığı nedeniyle Stellite 12 eriyik havuzu içerisinde bütün Cr_7C_3 parçacıkları tamamen eriyerek çözünmüştür. Cr ve C ile zenginleştirilen eriyik havuzu mikroyapı içindeki Cr_7C_3 ve $Cr_{23}C_6$ oluşumuna katkı sağlamaktadır. Cr bakımından daha zengin karbürlerin oluşumu Stellite 12+Cr_7C_3 kaplamaların sertliğini arttırmaktadır ve hacimce %10' luk Cr_7C_3 eklenmesiyle sertlik 636±6 HV_2' ye ulaşmaktadır.

Oda sıcaklığında ve 300 °C' de aşınmış kaplama yüzeylerinden alınan SEM mikrograflarında aşınma ilerleyişinde plastik deformasyonun dominant olduğu belirlenmiştir. Oda sıcaklığında aşınan kaplama yüzeyi, periyodik sürtünme sonucunda biriken plastik deformasyon ile karakterize edilmiştir. 300°C' de kayma hareketi yapan Al_2O_3 bilye kaplamalar üzerindeki aşınmış yüzey üzerinde hareket yönünde hizalanan çizgiler boyunca plastik deformasyona maruz kalmıştır. Sertlik, oda sıcaklığında ve orta dereceli sıcaklıklarda Stellite alaşımlarının tribolojik performansı üzerinde kritik bir rol oynadığından, oda sıcaklığında ve 300 °C'deki Stellite 12+Mo, Stellite 12+WC/W_2C, Stellite 12+TiC ve Stellite 12+Cr_7C_3 kaplamaların aşınma direncinin artışı, güçlendirici parçacıkların veya alaşım elementlerinin eklenmesi ile ötektik karbürlerin ve/veya intermetalik bileşenlerin oluşması ve hacimsel oranındaki artış şeklinde açıklanabilir. Ayrıca aşınma testi sırasında temas yüzeyinde kobalt zengin katı çözelti matrisinin işleme esnasında sertleşmesi oda sıcaklığındaki aşınma direncine katkıda bulunur. Uygulama sıcaklığının oda sıcaklığından 300 °C' ye yükselmesi ile incelenen kaplamanın aşınma direncinde dikkat çekici bir düşüş gözlemlenmiştir Bu durum, işleme sertleşmesi hızı ve mekanik sertliğin azalması ve/veya aşınma yüzeyi üzerindeki ince oksit tabakasının kolay tahribatı ile bağlantılı olabilir. Stellite 12'ye Ni'in eklenmesi oda sıcaklığında ve 300 °C'de incelenen kaplamaların aşınma kayıplarını arttırmıştır. Ni içeren numunelerdeki aşınma direncindeki azalma, işleme sertleşmesi hızı, sertlik ve mikroyapı içindeki sert ötektik karbürler veya intermetalik bileşenlerin hacimsel oranının azalması ile açıklanabilir.

Oksidasyon mekanizması, kaplamaların temel aşınma mekanizması olarak 500 ve 700 °C'de tanımlanmıştır. SEM analizleri göstermiştir ki yüksek sıcaklıkta aşınma yüzeyleri üzerinde sürekli ve koruyucu oksit film oluşumu alümina bilye ve sürtünme yüzeyinin direkt temasını azaltarak 300 °C'deki aşınma direncini iyileştirmiştir. 500 ve 700 ° C de Stellite 12 kaplamanın Raman spektroskopisi sinyalleri sırasıyla CoO ve Co_3O_4 ve Cr_2O_3'e karşılık gelmiştir. Cr_2O_3'ün iyi tribolojik karakteristiği uygulama sıcaklığı 500 °C'den 700 °C'ye çıktığında aşınma izinin azalmasına sebep olmaktadır.

Dominant oksidasyon mekanizması altında Stellite 12+Mo kaplamalar Stellite 12 kaplamalara göre daha iyi bir aşınma direnci sergilemişlerdir. Stellite 12 kaplamalara Mo eklenmesi ile 500 ve 700 °C'de sırasıyla istenilen Cr_2O_3 ve $CoMoO_4$ oluşmuştur. Cr_2O_3 ve $CoMoO_4$ oluşumu, katı çözelti matris içindeki Mo'nun çözünmesine ve mikroyapı içinde daha fazla $Cr_{23}C_6$'nın oluşmasına katkı sağlamış olabilir. Uygulama sıcaklığının 500' den 700 °C' yükselmesi kaplamaların aşınma kaybında bir azalmaya yol açmıştır. Koruyucu ve kaygan bir doğaya sahip olan $CoMoO_4$ kompleks oksidi, molibden içeren Stellite 12 kaplamaların 700 °C'deki aşınma kaybını önemli ölçüde azaltmıştır.

Stellite 12 kaplamalara Ni'in eklenmesi, 500 ve 700 °C'de işlem gören kaplamaların aşınma kaybı üzerinde önemli bir değişime sebep olmamıştır. Ayrıca, yüksek sıcaklık uygulamalarında artan Ni içeriğinin aşınma yüzeyi üzerindeki oksit filmlerin gelişmesine yardımcı olsa da sertliğin düşmesine ve buna karşın bilye altındaki zonun plastik deformasyonunun artmasına ve yüzey üzerinde oluşan oksit filmlerin kırılarak kaldırılmasına neden olmaktadır.

Stellite 12 içerisine katkılanan WC/W_2C'nin 500 and 700 °C' deki aşınma testi sonuçları aşınma direncinin arttığını göstermiştir. 500 °C'de incelenen kaplamaların aşınma yüzeyi üzerinde oluşan oksit film temel olarak Co_3O_4, Cr_2O_3 ve ayrıca WO_3'ten oluşmaktadır. Cr bakımından zengin katı çözelti matris içinde çözünün W atomu aşınma yüzeyi üzerindeki koruyucu Cr_2O_3 ve WO_3'ün gelişimine katkı sağlamıştır. 500°C'deki uygulama sıcaklığı ile karşılaştırıldığında, 700 °C'de yapılan aşınma testlerine, aşınma kaybının azalmasında önemli bir rol oynayan aşınma yüzeyi üzerindeki $CoWO_4$ kompleks oksidinin oluşumu eşlik etmiştir. 700 °C'de WC/W_2C takviye partiküllerin oksidasyon ve buharlaşması sonucu sürtünmeli aşınma boyunca partiküllerin ayrışmasına ve parçalanmasına sebep olduğu unutulmamalıdır.

Hacimce %2 ve %6 oranında TiC ekli Stellite 12+TiC 500 °C'deki aşınma direncini arttırmasına karşın, Stellite 12 ve Stellite 12+hac.% 10 TiC kaplamalarla yapılan incelemede kayda değer bir aşınma kaybı gözlemlenmemiştir. Hacimce %10'a kadar TiC eklenmesi Stellite 12 kaplamaların 700 °C'deki aşınma direncini azaltırken aşınma kaybı 2 katına çıkmıştır.

500 and 700 °C' de işlem gören Stellite 12+ hac.% 10 TiC kaplamaların aşınma yüzeyleri üzerinde oluşan oksit film CoO ve Co_3O_4'ten oluşmuştur. Hacimce %2 ve 6 TiC içeren kaplamaların daha yüksek sertliği, sürtünen bilye altındaki bölgenin plastic deformasyonunu azaltmak ve aşınma yüzeyi üzerinde oluşan oksit filmin kırılarak ayrılmasını engellemekte faydalı olmuştur. Bununla birlikte, Stellite 12+ hac.% 10 TiC durumunda oluşan daha fazla Cr bakımından zengin karbürlerin ve Co bakımından zengin katı çözelti matrisinin hacimsel oranının azalması aşınma yüzeyi üzerindeki sürekli koruyucu CoO filmin gelişimini engellemektedir. Ayrıca, daha fazla Cr bakımından zengin karbürlerin oluşumu yüzünden, krom atomları dentritik katı çözelti matrisinden yüzeye serbest bir şekilde taşınır ve 700°C'de sürekli bir Cr_2O_3 tabakası oluşturursa, beklenildiği gibi fazla korumacılık sağlamaz. Bu nedenle, Stelite 12 içerisine daha fazla TiC katkılanması 700 °C'deki aşınma direncinin azalmasına sebep olmuştur.

500 ve 700 °C'de yapılan test sonuçlarına göre, hacimce %10'a kadar eklenen Cr_7C_3 partiküllerin incelenen kaplamaların aşınma kaybını arttırdığı sonucuna varılmıştır. Hac.% 10 Cr_7C_3' eklenmesi ile 500 °C'deki aşınma kaybı önemli ölçüde artmıştır ve Stellite 12+Cr_7C_3 kaplamalar Stellite 12 kaplamalara göre 700 °C'de daha kötü bir

aşınma performansı sergilemiştir. 500 ve 700 °C aşınma deneylerinde aşınan yüzeylerde yeterli CoO ve Cr_2O_3 oluşmaması aşınmanın bu derece yüksek olmasının ana sebebi olarak belirlenmiştir.

1. INTRODUCTION

Wear is a serious problem that influences the life of engineering components in a large number of industries such as aerospace, power generation and metal working and fails their intended use due to loses dimension and functionality. Therefore, reduction of components or equipment precision and efficiency because of wear and the cost of replacement of parts, down-time and lost-labor will be reflected as financial loss.

In an effort to increase the life and improve the function of components, several attempts are made to alter and enhance their surface properties by metallurgical, mechanical, chemical or physical means which imposes different properties, advantages and disadvantages when compared with each other. Surface treatments that cause microstructure changes on the surface of bulk material include heating and cooling/quenching through induction, flame, laser, and electron beam techniques, or mechanical treatments (such as cold working). Surface treatments that alter the chemistry of a surface and enhance its properties include carburizing, nitriding, carbonitriding, nitrocarburizing, boriding, siliconizing, chromizing and aluminizing.

Another surface modifying method is coating or covering of components with a layer of wear and/or corrosion resistance materials. There is a wide range of coating processes for depositing many different types of material at thicknesses ranging from just a few microns, up to several millimeters. A good coatings needs to be well-matched with substrate in physical and chemical means, continues, non-porous and well adherent. Generally deposition process are divided into the following categories [1]:

1.) Gaseous state processes (e.g. CVD, PVD, IBAD),
2.) Solution state processes (e.g. electroless deposition, electrodeposition, sol-gel),
3.) Molten or semi-molten state processes (e.g. weld overlaying, laser cladding, thermal spray).

Factors affecting the choice of a deposition process include service environment, life expectancy, substrate material compatibility, component shape and size, and cost. Under the aggressive working condition at high temperature and loads, thin coatings formed by gaseous and solution state process do not meet required properties. Hardfacing technique which are based on covering the bulk materials with a relatively thick protective surface layers via molten or semi-molten processes, offers attractive technical solutions to fulfill these requirements and enhance the performance of the engineering components utilized in harsh environments [2-6]. In this method wear and corrosion resistance alloys can be deposited on the surface of a soft material by using high energy density sources such as the electric arc, plasma, laser or combustion of chemical means [7]. The most common deposition methods are arc welding techniques (weld overlaying), laser cladding and thermal spray. Different kinds of iron-, nickel- and cobalt-based hardfacing alloys have been developed for use in various aggressive environments where abrasion, sliding, erosive, impact and corrosion type of wear occurs [8]. Cobalt-based alloys have been used in wear-related engineering applications for more than 90 years due to their inherent high-strength, corrosion resistance, and ability to retain hardness at elevated temperatures [9, 10]. Stellite alloys, the most common and popular cobalt-based hardfacing group are commercially available in several modifications and grades. It contains chromium, tungsten or molybdenum and a small amount of carbon. The main differences between these Stellite alloys are their carbon and refractory element (W or Mo) contents and thus the carbide volume fraction formed during solidification [11]. As the highest carbon containing Stellite alloy, Stellite 1 (2.5 wt% carbon) is the most wear resistant one but it has a high risk of cracking during deposition. Stellite 6 with 1.2 % carbon content possess the least wear resistant owing to the formation of relatively low amount of hard carbides during solidification [12]. Stellite 12 with 1.6 % carbon content can be considered as an intermediate alloy between Stellite 6 and Stellite 1 and has become more attractive in the last few years for hardfacing applications [13]. Generally Stellite alloys are resistant to wear, galling and corrosion and retain their properties at high temperatures. But the largest application for cobalt-based alloys is for wear resistance. Their exceptional wear resistance is due mainly to the unique inherent characteristics of the hard carbides or intermetallic compounds dispersed in a CoCr solid solution matrix. The main type of wear that cobalt-based hardfacing alloys are applied on surface of engineering components to withstand against them are sliding, abrasive and erosive wear. Depending on the type of wear encountered in a particular application various kind of hardfacing alloys can be selected. The typical application area of some cobalt-based hardfacing alloys and related type of the wear that degrade them are illustrated in Table 1.1.

Table 1.1 : Typical application of some cobalt-based wear resistance alloys [14].

Applications	Alloy	Forms	Mode of degradation
Automotive industry			
Engine valve seating surfaces	6, F	Weld overlay	Solid-particle erosion, hot corrosion
Power industry			
Control valve seating surfaces	6, 21	Weld overlay	Sliding wear, cavitation erosion
Steam turbine erosion shields	Alloy 6B	Wrought sheet	Liquid-droplet erosion, particulate erosion
Marine industry			
Rudder bearings	306	Weld overlay	Sliding wear
Steel industry			
Hot shear edges	6	Weld overlay	Sliding wear, impact, abrasion
Bar mill guide rolls	12	Weld overlay	Sliding wear, impact, abrasion
Electrogalvanizing rolls	Ultimet	Wrought sheet	Erosion-corrosion
Chemical processing industry			
Control valve seating surfaces	6	Weld overlay	Sliding wear, cavitation erosion
Plastic extrusion screw flights	1, 6, 12	Weld overlay	Sliding wear, abrasion
Pump seal rings	6, 12	Weld overlay	Sliding wear
Dry battery molds	4	Casting	Abrasion
Pulp and paper industry			
Chain saw guide bars	6, alloy 6B	Weld overlay, wrought sheet	Sliding wear, abrasion
Textile industry			
Carpet knives	6K, 12	Wrought sheet, weld overlay	Abrasion
Oil and gas industry			
Rotary drill bearings	190	Weld overlay	Abrasion, sliding wear

Of the three major types of wear, sliding is perhaps the most complex, not in concept, but in the way different materials respond to sliding conditions such as load, speed and ambient temperature. Sliding wear is a possibility whenever two surfaces are forced together and moved relative to one another. Plastic deformation and fatigue and oxidation and fatigue which occur during direct contact and moving against of two surfaces govern the wear mechanism and tribological behavior of cobalt-based hardfacing alloy in dry sliding condition.

Abrasive wear which take place when hard particles, or hard projections (on a counter-face) are forced against, and moved relative to a surface, is strongly influenced by the size and shape of the abrading species and the size and shape of the hard phase or components presented in the microstructure of cobalt-based wear resistance alloys.

Erosive wear is caused by impingement of particles (solid, liquid or gaseous), which remove fragments of materials from the surface due to momentum effect. Generally, the erosive resistance of cobalt-based hardfacing alloys, like other wear resistant alloys, depends on the hardness of the carbides and/or the metal matrix phases.

Despite the successful applications of Stellite 12 alloy, wear still appears as a serious problem that influences the service life and performance of engineering components under high load and/or temperature working conditions. The need to increase the hardness, enhance the wear resistance and increasing corrosion resistance of deposited hardfacing alloys has encouraged scientists and engineers to develop and modify hardfacing alloys. Several attempts have been made to enhance wear resistance of Stellite 6 and low-carbon Stellite alloys by adding alloying elements or reinforcing with hard ceramic particles and promising results have been obtained which show enhancement in their abrasive and sliding wear resistance at room temperature [4, 7, 15-21]. While tribological performance of modified aforementioned Stellite hardfacing alloys at ambient temperature has been investigated, published information on the effect of addition of alloying elements and reinforcing particles on the sliding wear behavior of Stellite 12 alloy at high temperatures is scarce. In this dissertation work, structural characteristics, hardness, room and high temperature tribological performance of Stellite 12 coatings deposited by plasma transferred arc (PTA) welding technique on 4140 steel have examined upon systematically altering its composition by addition of molybdenum and nickel as alloying elements and reinforcing by WC/W_2C, TiC and Cr_7C_3 particles.

2. HARDFACING ALLOYS AND APPLICATION METHODS

2.1 Hardfacing Alloys

Hardfacing alloys consist of hard phases or compounds such as carbides, intermetallics, borides and silicide phases embedded in a strengthened cobalt-, nickel- and iron-based matrix [22, 23]. These multicomponent hardfacing alloys in the form of powder, rod, wire and electrode are homogeneously deposited on the surface of a carbon and low alloy steels by utilizing various welding deposition process, laser cladding or thermal spray techniques [7]. The essential characteristics of hardfacing alloys include superior tribological properties, excellent mechanical strength, good surface stability, superior oxidation and corrosion resistance and good phase stability at high temperatures [11]. Physical and mechanical properties of these alloys at room and elevated temperature strongly depend on their chemical composition as well as the crystal structure of matrix and the type and volume fraction of hard phases formed during deposition process. The deposited hardfacing layer may be a homogenous single component layer, a multilayer structure with different properties in each layer, a gradient structure with gradually changing material properties or a composite layer typically including a matrix of one hardfacing alloy and hard particles such as WC, VC, TiC and etc. [24, 25].

2.1.1 Nickel-based hardfacing alloys

Nickel-based hardfacing alloys have been used in industrial applications such as oil and rock drilling tricone bits, mining components, power plant boilers and gas turbine blades where a combination of high wear, corrosion and high temperature oxidation resistance is required [26-30]. Nickel-based hardfacing alloys mainly contain chromium and iron and are varied in the additive components such as carbon, boron and silicon. Based on the microstructure, nickel-based hardfacing alloys can be divided into three types: carbide type (Nistelle alloys), boride type (Deloro and Colmonoy alloys) and silicide type (Nucalloy alloys) [31]. Although the presence of silicon and boron can provide hard phases such as nickel and chromium borides and nickel silicide and consequently improve wear resistance of nickel-based hardfacing alloys but increase brittleness and crack susceptibility in deposited layer [32]. In general, carbide and silicide type alloys have lower sliding wear properties than cobalt- and iron-based hardfacing alloys, whereas boride type alloys have better abrasion resistance than cobalt-based alloys due to presence of hard phases (CrB, Cr_7C_3, $Cr_7(CB)_3$, Ni_3B and Ni_5Si_2) in their microstructure [33]. In addition to providing hard particles, Si and B are added to improve their wetting to the steel substrate during welding and provide them with self-fluxing characteristics [34-36]. The melting point of the NiCrBSi alloys is reduced by the addition of boron in concentrations up to 2.5 wt.% whereas silicon does not have an important influence on the melting point [32, 34].

2.1.2 Iron-based hardfacing alloys

Iron-based hardfacing alloys which contain various amounts of Cr, C, W, Mn, Mo, Ni, Si and B, depending on microstructure can be classified to austenitic manganese, martensitic and carbide type alloys [32]. Low carbon austenitic manganese hardfacing alloys are widely used under impact wear working conditions. Transformation of austenite to ferrite and martensite or mixture of them under repetitive plastic deformation increases work hardening rate and can be beneficial to impact wear resistance of these alloys [37-40]. Inexpensive martensitic iron-based hardfacing alloys are a good alternatives to applications where high stress abrasion, sliding wear and moderate corrosion resistance is needed [41-43]. In carbide type iron-based hardfacing alloy, high chromium and carbon contents provide a large volume fraction of chromium carbides which enhance sliding and low stress abrasion wear resistance [44, 45]. Carbide type iron-based hardfacing alloys are rarely used in high stress abrasive working condition due to formation of hard and brittle carbides in these alloys [46].

2.1.3 Cobalt-based hardfacing alloys

The commercial wear resistant cobalt-based alloys are derived from the cobalt-chromium alloys which were developed by Elwood Haynes in early 1900s [14, 47, 48]. Cobalt-based hardfacing alloys have been used widely in many industries due to their good wear, oxidation, and corrosion resistance and ability to retain hardness at elevated temperatures [9, 30, 45, 47]. Cobalt-based hardfacing alloys exist in several commercial grades and modifications which fulfill most of the industry requirements

[48]. Stellite alloys are most popular and important cobalt-based hardfacing alloys that due to their unique combination of excellent corrosion and oxidation resistance, mechanical and tribological properties at both room and elevated temperatures are used as a surface coating of components in aerospace, gas turbines, chemical, petrochemical industries and power plants [15, 48-52].The major constituents of Stellite alloys belong to the quaternary systems Co–Cr–W–C or Co–Cr–Mo–C that main difference between these alloys are their carbon and refractory elements (tungsten or molybdenum) contents. The compositions of various Stellite powders used in PTA deposition process are shown in Table 2.1.

Table 2.1 : Chemical compositions (wt%, Co in Balance) of various Stellite alloy powders used in PTA deposition process [53].

ALLOY	NOMINAL ANALYSIS OF POWDER[1]								Others	UNS	Hardness (HRC)[2]
	Co	Cr	W	C	Ni	Mo	Fe	Si			
COBALT-BASED ALLOY (GAS-ATOMIZED POWDERS)											
Stellite™ alloy 1	Bal.	30	13	2.5	<2.0	<1.0	<2.0	<2.0	<1.0	R30001	51–60
Stellite™ alloy 4	Bal.	30	13.5	0.7	<2.5	<1.0	<2.5	<1.0	<1.0	R30404	40–50
Stellite™ alloy 6	Bal.	28.5	4.6	1.2	<2.0	<1.0	<2.0	<2.0	<1.0	R30106	40–46
Stellite™ alloy 6LC	Bal.	29	4.5	1.1	<2.0	<1.0	<2.0	<2.0	<1.0	–	38–44
Stellite™ alloy 6HC	Bal.	28.5	4.6	1.35	<2.0	<1.0	<2.0	<2.0	<1.0	–	43–53
Stellite™ alloy 156	Bal.	28	4	1.7	<2.0	<1.0	<0.5	<2.0	<1.0	–	46–54
Stellite™ alloy 12	Bal.	30	8.5	1.45	<2.0	<1.0	<2.0	<2.0	<1.0	R30012	43–53
Stellite™ alloy 20	Bal.	32.5	17.5	2.55	<2.0	<1.0	<2.0	<1.0	<1.0	–	52–62
Stellite™ alloy 21	Bal.	27.5	–	0.25	2.6	5.4	<2.0	<2.0	<1.0	R30021	27–40 *
Stellite™ alloy 22	Bal.	28	–	0.30	1.5	12	<3.0	<2.0	<0.5	–	41–49 *
Stellite™ alloy 25	Bal.	20	15	0.1	10	<1.0	2	<1.0	1.9%Mn	–	20–45 *
Stellite™ alloy 31	Bal.	26	7.5	0.5	10.5	<1.0	<2.0	<1.0	<0.5	R30031	20–35 *
Stellite™ alloy F[3]	Bal.	26	12.5	1.8	22	<1.0	<2.0	1.1	<0.5	R30002	40–45
Stellite™ alloy 190	Bal.	26	14	3.4	<2.0	<1.0	<2.0	<1.0	<1.0	R30014	55–60
Stellite™ alloy 250	Bal.	28	<1.0	0.1	<1.0	<1.0	20	<1.5	<1.0	–	20–28
Stellite™ alloy 694	Bal.	28.5	19.5	0.9	5	–	<3.0	<1.0	1%V	–	46–52
Stellite™ alloy 706	Bal.	29	–	1.25	<2.0	4.5	<2.0	<1.0	<1.0	–	39–44
Stellite™ alloy 712	Bal.	29	–	2.0	<2.0	8.5	<2.0	<1.0	<1.0	–	46–53

Stellite alloys can be broadly classified into two main categories: low-carbon (0.1–0.50%) alloys intended for use in severely corrosive environments or where ductility is an important consideration and high-carbon (1-3%) alloys which exhibit high hardness and can provide resistance to abrasive and sliding wear [14, 54]. Generally high carbon containing Stellite alloys have a typical microstructure of dendritic Co-rich solid solution matrix with a FCC (α-Co) and HCP (ε-Co) crystal structure surrounded by lamellar eutectic phases. Eutectic phase consisted of Co-rich solid solution phase, Cr-rich carbides and refractory metals (tungsten or molybdenum) containing complex carbides and intermetallic compounds [55]. For carbon contents lower than 2 wt%, these alloys show hypo-eutectic solidification characteristic in which primary Co-rich solid solution matrix surrounded by a network of eutectic phases (as shown in Figure 2.1). For carbon contents higher than 2 wt%, they are hyper-eutectic and the first phases which form are primary carbides or intermetallics compounds and then interdendritic eutectic matrix solidified [11].

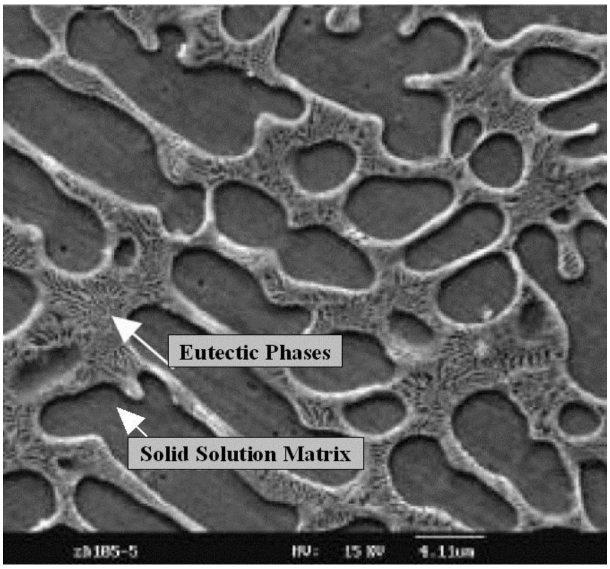

Figure 2.1 : SEM micrograph of laser cladded Stellite 6 alloy [17].

Chromium as a main element is added in the range of 20-30 wt% to increase strength, corrosion and oxidation resistance by formation of solid solution with cobalt. Also it is predominant carbide former and plays a crucial role in increasing mechanical properties via the formation of Cr_7C_3 and $Cr_{23}C_6$ carbides [7, 18, 47, 49, 56-58]. Tungsten and molybdenum which have been known as solid solution hardening elements provide additional strength because of their large atomic size [4, 18, 59-61]. More addition of these elements contributes to the strength due to formation of (W, Mo)C carbides (with hexagonal crystal structure) and complex carbides such as $Co_3(W, Mo)_3C$ and/or $Co_6(W, Mo)_6C$ (with cubic crystal structure) and $Co_3(W, Mo)$ intermetallic compound (with hexagonal crystal structure) [48, 62, 63]. Nickel and diluted iron from substrate without forming any phases or compounds in the microstructure dissolve in solid solution matrix. Presence and amount of elements dissolved in matrix can alert crystal structure of matrix. Pure cobalt has two allotropic modifications; HCP form (ε-Co), stable at temperatures below 417 °C, and a FCC form (α-Co), which is stable between 417 °C and its melting point of 1495 °C. Transformation temperature depends critically on cooling rate and alloying elements [9, 64]. Cobalt-rich solid solution matrix in cobalt-based hardfacing alloys exists in the form of an unstable FCC and a stable HCP crystal structure at room temperature. The instability arises from the fact that if cobalt cooled extremely slowly, transforms from FCC to a HCP crystal structure completely at 417°C. Because of the sluggish nature of the transformation, the FCC structure in cobalt and its alloys is usually retained to room temperature, and HCP transformation is initiated and progressed by mechanical stress at room temperature or time at elevated temperature. This strain-induced phase transformation process involves the coalescence of stacking faults, which is achieved by the passage of a Shockley partial dislocation. Dissociation of a full dislocation owing to the low stacking fault energy on every second $\{111\}$ plane in an FCC crystal results in passage of a Shockley partial dislocation. Therefore the mechanism of the phase transformation occurs by shear with the following crystallographic relationships between the two phases [9]:

$$\{111\}_{\alpha} \parallel \{0001\}_{\varepsilon} : \langle 110 \rangle_{\alpha} \parallel \langle 11\bar{2}0 \rangle_{\varepsilon}$$

This transformation is classified as martensitic, arising from the mobility of partial dislocations along the close-packed planes. As shown in Figure 2.2 alloying addition of Ni and Fe promotes the stability of FCC structure of cobalt whilst Mo and W tends to stabilize HCP crystal structure [7].

$$ABCABC \Rightarrow ACBACB$$

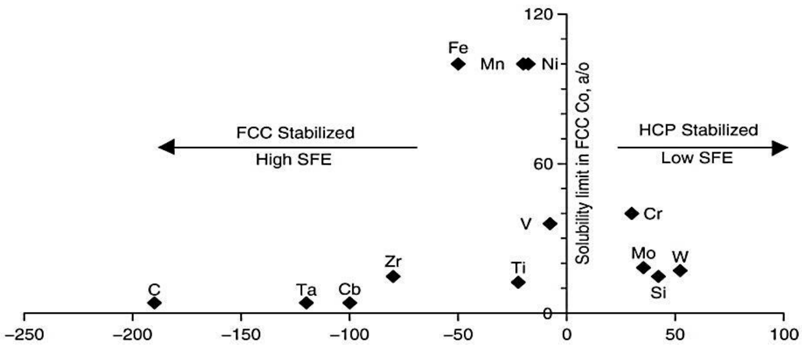

Figure 2.2 : Changing in the HCP-FCC transformation temperature (°C) by addition of 1 wt% of different elements [9].

Refractory metals such as tungsten and molybdenum, by reducing the stacking fault energy, enhance the plastic deformation induced FCC to HCP crystal structure transformation in the cobalt-rich solid solution matrix [49, 62, 65].

2.2 Hardfacing Methods

Various processes are currently applied to deposit hardfacing alloys on surface of components which are prone to wear and/or corrosion in the field of aerospace, petrochemical, mining, steel and iron industries, cement industries and power plants in order to increase their service life or to restore a worn-down surface [66, 67].

The mostly used hardfacing techniques are [49, 68-77]:

PTA Welding

Laser Cladding

Thermal Spray

Welding is one of hardfacing deposition technologies that fulfill these requirements. The most common welding processes are shielded metal arc welding (SMAW), gas metal arc welding (GMAW), gas tungsten arc welding (GTAW) and PTA [2, 7, 48, 77-79]. Selection of suitable welding process for this purpose depends on a number of parameters like coating thickness and compatibility with base metal, size and shape of component, accessibility of weld equipment and number of same or similar items to be hardfaced etc. [66, 67]. Among the arc welding techniques, PTA is very attractive and represents a very good alternative to other conventional welding processes in terms of high deposition rate, lower heat input, excellent arc stability and most importantly the wide range of choices of materials [3, 6, 78]. In this process heat obtained from a constricted plasma arc between a tungsten electrode and the water-cooled nozzle and work piece is used for heating and melting filling materials in the form of powder. Inert gases to form the plasma arc, carry feedstock materials and the shield the arc are employed.

Laser cladding is another hardfacing technique that uses a high power, focused and controlled laser beam to melt the feeding material and deposit surface coating on the selected area of metal substrates with controlled thickness, excellent metallurgical joint and minimum dilution [17, 80, 81]. For producing protective layer hardfacing alloy can be introduced on the surface of components either before laser processing (pre-deposition or replaced powders) or during processing (co-deposition or blown powder) [82]. In co-deposition process the feeding materials in the form of wire or powder can be supplied either laterally (off-axis) and coaxially toward the laser beam. In Figure 2.3 different feeding systems in laser cladding process are schematically illustrated.

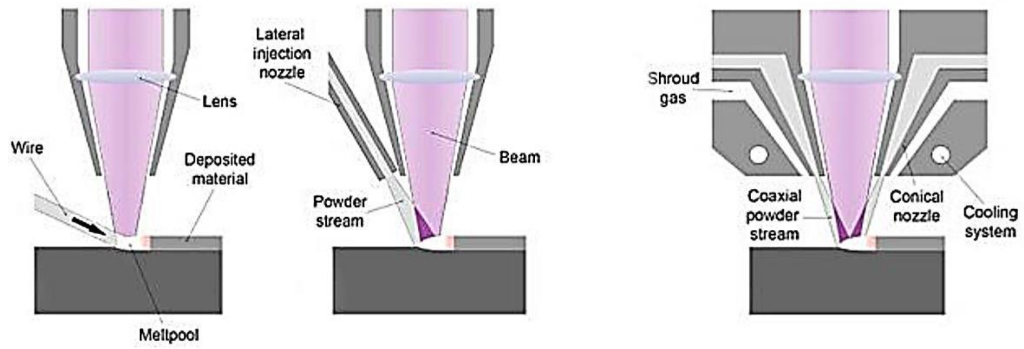

(a) (b)

Figure 2.3 : Schematic illustration of a) lateral and b) coaxial feeding systems in laser cladding process [83].

The most advantages of the laser cladding process over conventional welding deposition methods are minimum heat input on the part which decrease heat-affected zone (HAZ), lower dilution and eliminate distortion [84-86]. Also because of high cooling rate in laser cladding process, fine grain structure can be obtained which is beneficial to increase hardness and wear resistance of deposited layer [80]. Nevertheless the advantages of laser cladding, a number of features such as lower capital and maintenance costs, higher thickness capability, higher deposition efficiency and rate and easier to integrate into some production setting due to small size favor PTA over laser cladding [3, 87-93].

Thermally spray coating process is one of major hardfacing techniques that produce protective layer by rapidly heating feedstock (metallic or non-metallic material) in the form of powder, wire or ceramic rod in order to fully or partially melt and simultaneously projecting them at a high velocity onto a prepared surface. In this coating method feedstock is heated in a hot gaseous medium by arc, plasma or chemical means [94].

There are several different processes used to apply a thermal sprayed coating such as conventional flame spray process, electric arc wire spray, plasma spray and high velocity oxy fuel spray (HVOF). As the most popular thermal spraying technique, HVOF has been widely adopted by many industries due to its low heat input, flexibility (utilizing with a wide variety of substrate and coating materials), convenient and cost effectiveness [94-97]. Figure 2.4 shows schematic of HVOF combustion chamber.

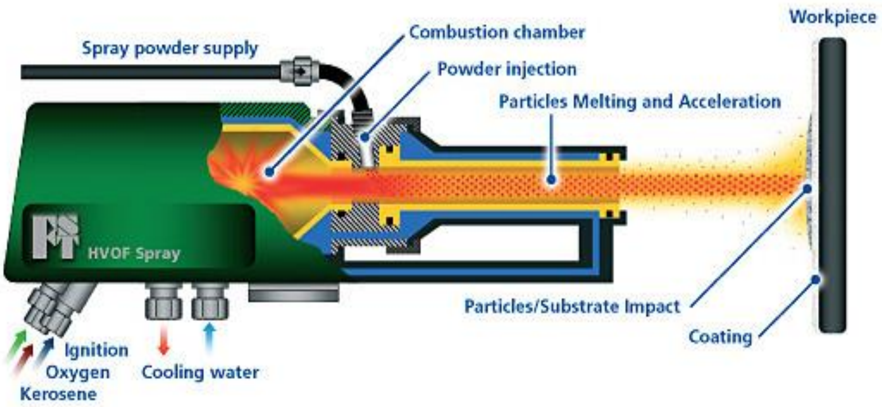

Figure 2.4 : Schematic of HVOF combustion chamber [98] .

In spite of advantages of this technique, interconnected porosities which generally formed during thermally sprayed coating processes (as shown in Figure 2.5), impair the mechanical properties and reduce corrosion resistance of deposited layer [94, 99, 100].

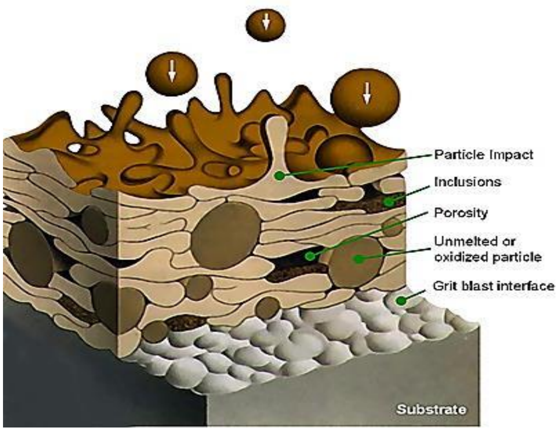

Figure 2.5 : Schematic cross-section of thermally sprayed layer [101].

Also reinforcement of HVOF coatings with hard ceramic particles can lead to increase porosity, provide low metallurgical bonding and cohesive strength within these coatings [102]. Another common disadvantage of thermal spraying techniques is poor adhesion between deposited layer and substrate that is primarily mechanical not metallurgical [102-104]. The technological differences between the hardfacing processes are listed in Table 2.2.

Table 2.2 : Comparison of hardfacing methods [87].

Parameter	PTA Deposition	Laser Cladding	Thermal Spray
Particle deposition velocity (m/s)	----	0.2-6	100-250
Coating rate (g/min)	8-250	6-30	8-50
Coating thickness (mm)	1-6	0.25-3	1.5-2.5
Heat affected zone depth (mm)	2-4	0.4-2	0.2-0.5
Powder efficiency (%)	80-90	60-70	40-50
Substrate surface temperature (°C)	400-600	60-600	100-900
Cooling rate (K/s)	10^2-8×10^3	10^3-10^6	10^4-10^5

2.2.1 Plasma transferred arc welding

PTA welding developed in1960's is an extension of the GTAW process which utilizes shielding gas for protection of the molten pool and formation of plasma arc between non-consumable tungsten electrode and a substrate [74, 78, 105]. Although PTA is derivation of the GTAW there are distinct differences between these two processes which arise from plasma arc and filler materials. A schematic of PTA process used for deposition of hardfacing layer is shown in Figure 2.6.

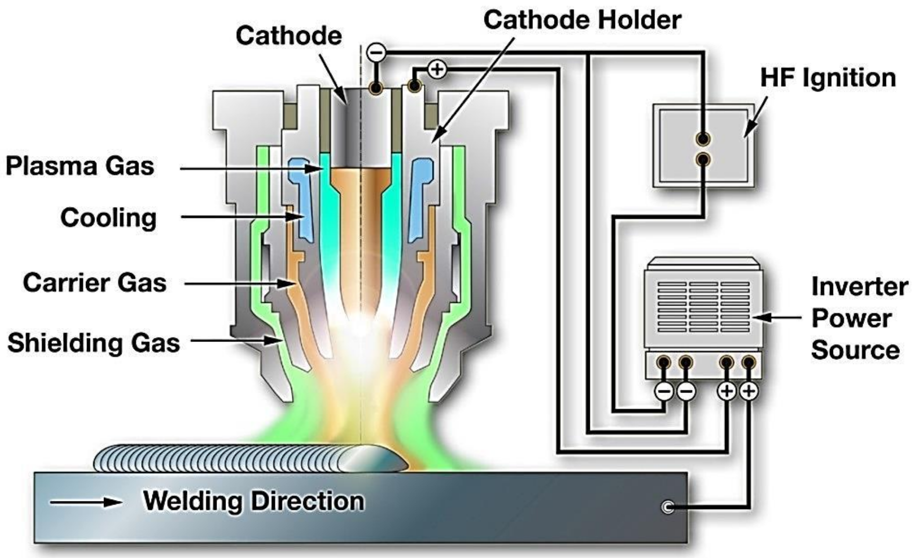

Figure 2.6 : Schematic of the PTA process used for depositing hardfacing layer [106].

In PTA two DC power suppliers are utilized to stablish non-transferred (also known as pilot arc) and transferred arc [87]. A non-transferred arc produced and constricted between non-consumable tungsten cathode and water-cooled copper anode placed within the body of torch and transferred arc are initiated between tungsten electrode and the work piece [69]. When the transferred arc is ignited, the work piece becomes part of the electrical circuit and the plasma arc which is generated inside the torch is directed and focused through the torch orifice into the work piece. Physical constriction between anode and cathode induced high density and more stable plasma arc forced through a fine orifice at high velocities and temperature and leads to columnar shaped and stable arc, greater penetration and deposition rate [93, 107, 108]. In the PTA process the powder is continuous transported from the hopper through flexible tubes to the torch by an inert carrier gas and introduced into the plasma arc and heated and accelerated to the substrate surface. Transferred arc produces the energy density needed to melt both the base metal and the feedstock materials. A molten weld pool formed on the surface of substrate is protected against oxidative atmosphere by a curtain of active or inert gas as shielding gas [107]. Plasma arc temperatures differ in any position of plasma column and depend on type of plasma gas and welding parameters. Argon, helium and hydrogen or mixture of them can be used as plasma gas. Generally temperature at the exit of the plasma nozzle can exceed 10000 °C and work piece temperature may reaches to approximately 300 ºC when arc current and voltage is about 120 A and 30 V respectively [93, 109]. In the deposition process that argon is used as plasma gas and current of 200 A and voltage of 29 V are applied, temperature of top surface, 4 mm below the top surface of the weld pool and weld pool were estimated to be 2700, 1700 and 1650-1700 °C, respectively [109]. Figure 2.7 shows the arc temperature distribution and its difference between PTA and GTAW under constant welding parameters of current and voltage (argon is plasma gas, arc current and voltage is 200 A and 29 V respectively). In GTAW non-constricted arc leads to ball shape plasma and a lack of concentrated power in the work piece, which results in a bigger seam and a larger heat-affected zone (Figure 2.8). One of the most important advantages of PTA over GTAW process is its low amount of dilution [89]. Typically PTA produces dilution as low as 10% compared to 20-25% obtained by GTAW hardfacing method [70]. Another difference between PTA and GTAW lies in the nature of the filler material which powder is used instead of wire. Since in PTA powder can be used as deposit materials, it has far more flexibility than GTAW in terms of ability to produce relatively free of defects hardfacing layer with any desired composition by mixing of powders [69].

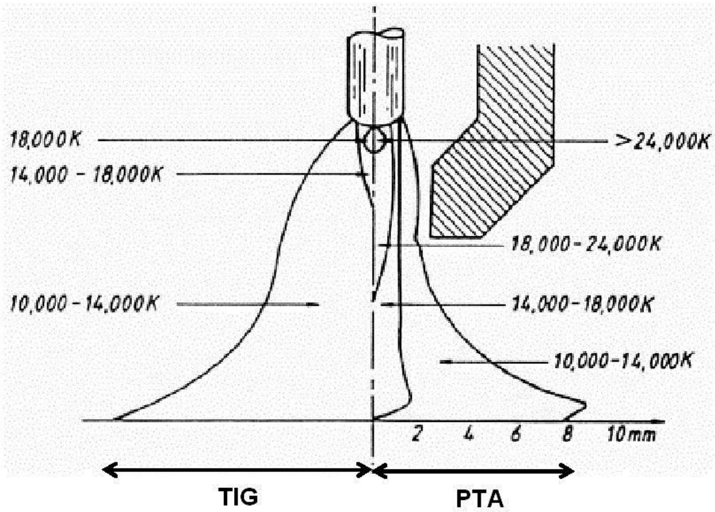

Figure 2.7 : Arc temperature distribution and its difference between PTA and GTAW under constant welding condition [109].

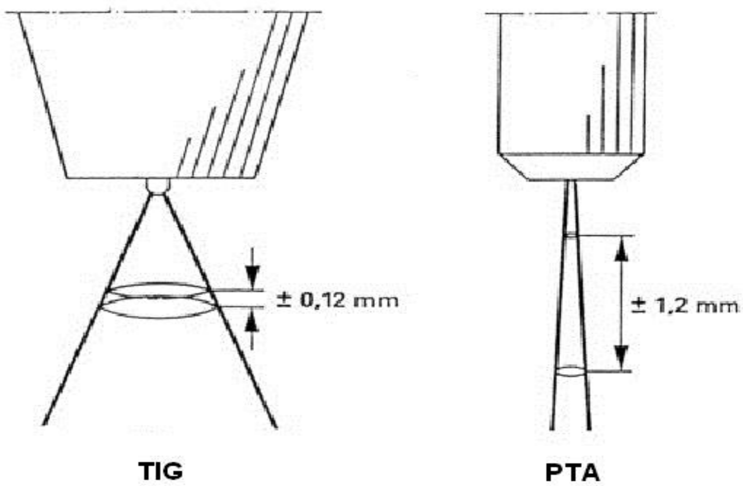

Figure 2.8 : Effect of arc shape on intensity of arc and heated affected area in GTAW and PTA welding process [109].

The mechanized PTA welding unit in addition to plasma torch consists of the pilot and plasma arc power supplies, mechanized torch oscillation unit or robot, component manipulator or rotating table, hopper for feedstock powder and torch cooling unit. In automated PTA process deposition rates in industrial uses range from approximately 1–15 kg/h. It is noticeable that this value can reach up to 25 kg/h by using specialty torches [69]. In PTA process excellent coating substrate adhesion can be achieved due to metallurgical bonding and the coating thickness can varied between 2-10 mm in one pass.

The main applications for PTA welding are valve seats and cones in combustion engines, cladding of tools, turbine blades, injection and extruder screws, sliding and sealing surfaces of armatures (gas, water and acid), plungers and moulds in the glass industry and pump parts, etc.

The welding parameters in PTA which strongly influence microstructure and mechanical properties of deposited layer are: current, voltage/stand-off distance, plasma gas and its flow rate, powder feeding and carrier gas flow rate, shielding gas, torch travel speed, oscillation speed and powder size distribution and morphology. To achieve soundness and high quality deposited layer with desired properties, a different set of operating parameters which are determined experimentally can be applied during deposition process.

2.2.1.1 Current

Transferred arc current is one of the essential parameters in controlling heat input of plasma arc during deposition process. For yielding the maximum powder utilization efficiency and obtaining defect free deposited layer with excellent adhesion with the substrate an optimum arc current should be applied. Working in an arc current level above the optimum value causes the addition of more heat into the process and raises the temperature of both deposited layer and the substrate that consequently leads to dilution of layer from substrate and vaporization of smaller powder particles [87, 107, 110]. Vaporization of small powder particles reduces the powder efficiency. At lower currents than optimum value, insufficient heat is generated to melt the powder or the substrate and there is poor adherence of the layer with the substrate [107]. Effect of variation of arc current on the temperature distribution of plasma arc formed between the torch nozzle and piece work are shown in Figure 2.9. As it is obvious in this figure increasing current leads to increase in temperature and plasma penetration depth in to substrate. Deeper plasma penetration increases dilution effect during deposition process.

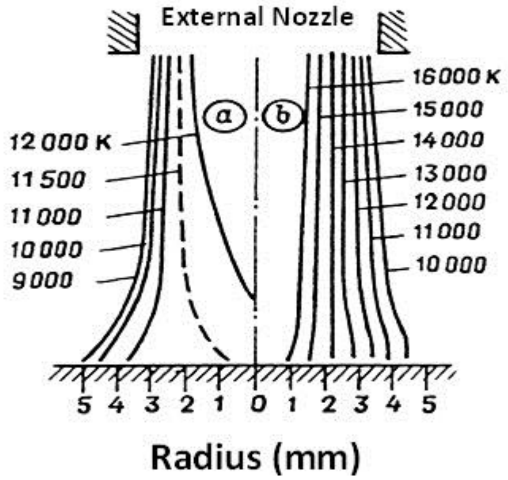

Figure 2.9 : Distribution of plasma arc temperature when argon as a plasma gas and: a) 100 A and b) 220 A are applied during welding [109].

2.2.1.2 Voltage and stand-off distance

Another welding parameter that should be considered for efficient deposition is voltage. Increasing in voltage leads to increase in amount of heat input. As show in Figure 2.10, the welding voltage value is directly related to the distance between the torch and the work piece which is labeled the stand-off distance [107].

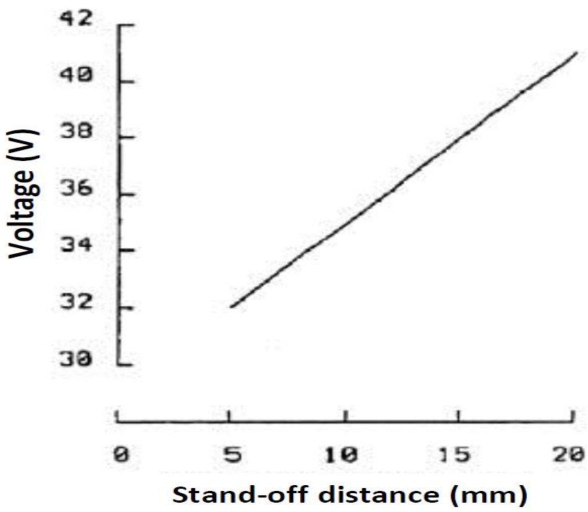

Figure 2.10 : Effect of stand-off distance on plasma voltage with plasma arc current 140 A [109].

In the closer stand-off distance, voltage should be kept low to diminish the dilution effect in deposited layer. Dilution of iron from the substrate decreased with increasing the stand-off distance. On the other hand the stand-off distance has an upper limit which above this range, shielding gas efficiency is reduced significantly and melting pool can be contaminated by environment [87].

2.2.1.3 Plasma gas and its flow rate

Ionized Ar, Ar-H_2, Ar-He or He as plasma gas can be used in PTA process and their physical properties such as density and ionization energy and also their flow rate dictates the heat input, shape of plasma arc and magnitude of the arc collimation and plasma velocity. Density and ionization energy of Ar, He, and H_2 gases are 1.784, 0.178, 0.090 kg/m^3 and 15.8, 24.6, and 13.6 eV, respectively [109, 111, 112]. Ar is the most common plasma gas in the PTA welding method. It is inert and it does not oxidize or react with the weld pool. While Ar is used as plasma gas it ionizes easily, which determines the ease of the plasma arc ignition and its stability.

Ar-H_2 (5-10% H_2) gas mixture has excellent deoxidizing and focusing effects therefore it is preferred to be used as shielding gas rather than plasma gas. Low amount of H_2 in the plasma arc increases thermal intensity, heat input, penetration, and welding speed.

He content in the Ar-He plasma gas can be between 30 and 100 %. He has high ionization energy, which offers increased welding speed, penetration, and improved weld quality when compared to Ar gas.

When the higher plasma gas flow rate and main arc current are applied during the deposition process, the formation of pores and oxides, higher penetration into the substrate, more dilution and vaporization of both the substrate and powder occurs [87, 107]. By reducing plasma gas flow rate and controlling arc current aforementioned defects can be avoided due to homogenous distribution of plasma arc [107].

2.2.1.4 Powder feeding and carrier gas flow rate

The powder feeding rate in PTA machine can be altered by the carrier gas flow rate and the bucket wheel speed of hopper [107]. Because carrier gas and the feedstock powder are feed straight into the plasma arc, properties of carrier gas can influence on plasma arc characteristics. Generally, the carrier gas consists of Ar, Ar-H_2 or Ar-He [87]. An increase in carrier flow rate without changing the other parameters cools the plasma arc column. Insufficient heating of powders leads to the formation of porosity within layer or weak bonding between layer and substrate [113]. Also higher carrier gas flow rate transport the powder beyond the plasma column and results in powder wastage. Decreasing powder feeding rate (if all other parameters are held constant) would increase the dilution content due to overheating of substrate and powders [87].

2.2.1.5 Shielding gas

Primary function of shielding gas is to produce neutral or reducing atmosphere and protect molten pool from contamination. Also shielding gas plays a crucial role in providing a medium for stable arc operation. In these respect density, thermal conductivity and non-reactive properties of shielding gas play a crucial role on quality of deposited layer. The first shielding medium used was the gaseous products of oxyacetylene or hydrogen combustion and usually consisted of hydrogen, carbon monoxide and carbon dioxide. However in modern welding process Ar, He, CO_2 or N_2 gases are used as shielding medium [112]. Ar due to its lower thermal conductivity, high density and low burning of alloying elements are frequently used in PTA process.

2.2.1.6 Torch travel speed

Torch travel or welding speed by altering the heat input amount affects the quality of deposited layer. Penetration depth, weld width and dilution decrease when travel speed is increased [114, 115]. On the other hand reducing travel speed gives better deposition of feedstock materials and bonding between deposited layer and substrate [116].

2.2.1.7 Oscillation speed

The thickness of the deposited layer in PTA is influenced by oscillation speed. Also the oscillation speed should be modified to surface properties of component and deposited alloy. For instance in the small components, like the valve heads, lower oscillation speed of torch can cause too high heat input to the surface of component and, thus, the valve head can be overheated and distorted [109]. The most common oscillation modes are zigzag and rectangular wave oscillation modes which are presented in Figure 2.11.

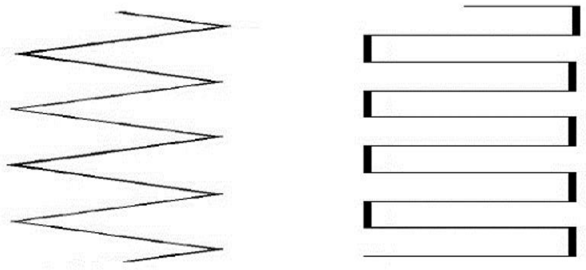

(a) (b)

Figure 2.11 : The most common oscillation wave modes used in the PTA welding process a) zigzag wave b) rectangular wave [109].

2.2.1.8 Powder size distribution and morphology

Particles for PTA welding deposition process are limited to a narrow size range (50-150 pm) to reduce feeding problems. Particles larger than 150 μm or smaller than 50 μm promotes obstructions in feeding system [87]. Maximum particle sizes for PTA have been recorded as 250 μm [107]. In the case of metal matrix composite layers that ceramic particles (WC, TiC, Cr_2C_3, VC, TiB etc.) are added to hardfacing alloys, reinforcement morphology is also restricted to spherical or angular shaped particles. Whisker or fiber shaped particles are not used in PTA welding process due to their poor feeding characteristic [87]. Spherical reinforcing particles are preferred over particles with irregular morphology. However, the production costs of spherical particles are higher, as they are made by an atomization process [87].

3. IMPROVEMENTS IN STELLITE HARDFACING ALLOYS

In recent years many investigations have been done to further strengthen and improve the wear resistance properties of Stellite alloys by addition of various alloying elements such as molybdenum and yttrium [4, 7, 15, 19, 117, 118] and reinforcing with ceramic particles such as WC, WC/W_2C and VWC [16-18, 20, 32]. Alloying elements or reinforcing ceramic particles can be partially or fully melted and alter chemical composition of hardfacing alloys which leads to significant solidification characteristics and microstructure and consequently affect their physical and mechanical properties.

3.1 Alloying Elements Added Stellite Hardfacing Alloys

Kuzucu et al investigated the effect of addition of 6 wt% molybdenum to Stellite 6 alloy [15]. As cast molybdenum containing Stellite 6 alloys consisted of cobalt rich solid solution matrix (α-Co and ε-Co) and Cr_7C_3, $Cr_{23}C_6$, (Mo,W)C, $Co_3(Mo,W)_3C$ carbides and Co_3Mo intermetallic compound. Further microstructural analysis revealed that rapid cooling of samples in water and liquid nitrogen after annealing at 950 °C encourage martensitic transformation of α-Co to ε-Co phase which lead to increase in hardness of samples from 40 HRC to 49 HRC.

Microstructure and abrasion wear resistance of Stellite 6 alloy with different contents of molybdenum was investigated by Shin et al [7]. In this research Stellite 6 alloy was mixed with 3 and 6 wt% molybdenum and deposited by PTA process under the constant welding condition. Microstructural characterizations show that increasing the molybdenum contents leads to formation of $Cr_{23}C_6$ and M_6C complex carbide instead of Cr_7C_3 carbide. Also addition of molybdenum to Stellite 6 resulted in refinement of cobalt-rich solid solution matrix and $Cr_{23}C_6$ carbide formed in interdendritic region. While abruptly increases was observed in the particle size and volume fraction of M_6C type complex carbide with increasing molybdenum content, volume fraction of $Cr_{23}C_6$ carbides increased slightly. Molybdenum containing

Stellite 6 hardfacing alloys showed superior abrasive wear resistance compared to molybdenum free Stellite 6 alloy at room temperature.

Wang and Li studied structure, hardness and high temperature wear performance of Stellite 6 alloy which was melted with 1, 2 and 5 wt% of yttrium [117]. Yttrium free Stellite 6 mainly consisted of chromium carbide as Cr_7C_3 and $Cr_{23}C_6$ and Co_3W intermetallic phase. Addition of yttrium leads to finer microstructure and formation of Co_2Y phase which was useful to improve the hardness and wear resistance of 1 and 2 wt% yttrium containing alloys. Increasing the content of yttrium to 5 wt% diminish its beneficial effect on the hardness and wear resistance at room temperature due to formation of brittle $Co_{17}Y_2$ intermetallic phase in addition to Co_2Y. Also alloying Stellite 6 alloy with yttrium enhanced its wear resistance at elevated temperatures because of formation of more adherent oxide layer.

Addition of yttrium to Stellite 21 and Stellite 712 and its effect on their tribological performance were investigated in details by Radu et al [4, 118] . Results showed that addition of yttrium (0.5 and 5 wt%) to remelted Stellite 21 improved wear resistance of Stellite 21 alloy at 600 °C and under low load in air [118]. Addition small amount of yttrium (e.g. 0.5 wt%) to Stellite 712 did not result in the formation of new phases but enhanced the mechanical properties of the oxide scale and its adherence to the substrate. However Co_2YSi_2 phases was formed when yttrium contents increased to 5 wt% [4].

Huang et al modified casting low-carbon containing Stellite 21 alloy by doubling the molybdenum content [19]. Increasing molybdenum content from 5.5 wt% to 11 wt% in Stellite 21 alloy leads to changes in the microstructure and formation of Co_3Mo and Co_7Mo_6 intermetallic compounds which was beneficial to its wear resistance and hardness.

The effect of different amount of tantalum on microstructure of Stellite 6 hardfacing alloy in laser cladding process was investigated by Farnia et al [119]. Microstructural analysis show that with an increase in Ta content, in addition to Cr_7C_3 carbides observed in the Ta-free Stellite 6 alloy in interdendritic regions, $Ta_4C_{3.04}$ type carbides are formed as well as individual bulky TaC type carbides in eutectic area. Furthermore, the Co-rich dendrites become much finer. With further increase of Ta, Cr_7C_3 carbides are formed at the interface of $Cr_{23}C_6$ carbides. These microstructural changes are responsible for the improvement of the hardness of the Ta modified Stellite 6 hardfacing alloy.

Liu et al developed novel high tungsten Stellite alloy (increased to 32 wt% from the normal 4–18 wt% in Stellite alloys) and studied its microstructure and wear resistance [120]. Investigation shows that excessive W content promoted formation of primary W-rich carbide phase, consisting of $(W, Co)_6C$ and Co_4W_2C, in the alloy. These carbides are present in large quantities and have large sizes. They possess comparable hardness to the Cr-rich carbides in Stellite alloys. The large amounts of large-size W-rich carbides provide this new alloy with excellent resistance to sliding wear and solid-particle erosion, better than well-known wear-resistant Stellite 3 and Stellite 6.

3.2 Hard Particle Reinforced Stellite Hardfacing Alloys

Metal matrix composites (MMC) commonly have a good combination of hard ceramic reinforcements and ductile metallic matrix, which make them a promising candidate for being used in wear resistance applications such as rock and trash crushers, excavator teeth, teeth of rock bits, chutes, dies, extrusion and cutting tools, grinding tools, metal-forming tools and road construction equipment [32, 121, 122]. Hard reinforcements are preferably chosen among high melting point and low solubility ceramic carbides, borides, nitrides or oxides in order to mix with the molten matrix without fully melting or dissolving in it during deposition process. Frequently used hard particles are WC, WC/W_2C, Cr_3C_2, Cr_7C_3, TiC, SiC, VC, B_4C, TiB_2, TiN and Al_2O_3 [32, 69, 75, 123, 124]. In spite of high melting point of hard reinforcements, some part of particles may fully or partial melted due to high heat of deposition process which leads to formation of new phases. Type of these phases are a function of the chemical composition of the matrix and the reinforcement particles and their reactivity, solubility and melting ranges [107]. Hard reinforcement particles differ in, physical, mechanical and chemical properties and their amount, morphology and size and distribution influencing the choice of metal matrix, deposition method and properties of MMC layers.

3.2.1 Physical and chemical properties of reinforcement particles

Crystallographic, physical and mechanical properties of most frequently used hard reinforcement particles used for deposition MMC layer are presented in Table 3.1.

Table 3.1 : Properties of reinforcement particles used for producing MMC layers [32, 107, 125, 126].

Particles	Hardness (HV)	Density (g/cm^3)	Melting Point (°C)	Crystal Structure
WC	2200	15.8	2870	Hexagonal
W_2C	3000	17.2	2730	HCP
TiC	3100	4.9	3100	FCC
Cr_2C_3	1400	6.7	1810	Orthorhombic
Cr_7C_3	1630	6.9	1755	Orthorhombic
TiB_2	3000	4.5	2980	HCP
VC	2700	5.7	2830	FCC

For some common particles change of Gibbs free energy of formation which governs the thermal stability are presented in Figure 3.1. The higher the negative value of energy, the more stable the particle. As it is obvious in this figure, TiB_2 and TiC are the most table particles and W_2C is more stable at high temperatures than WC.

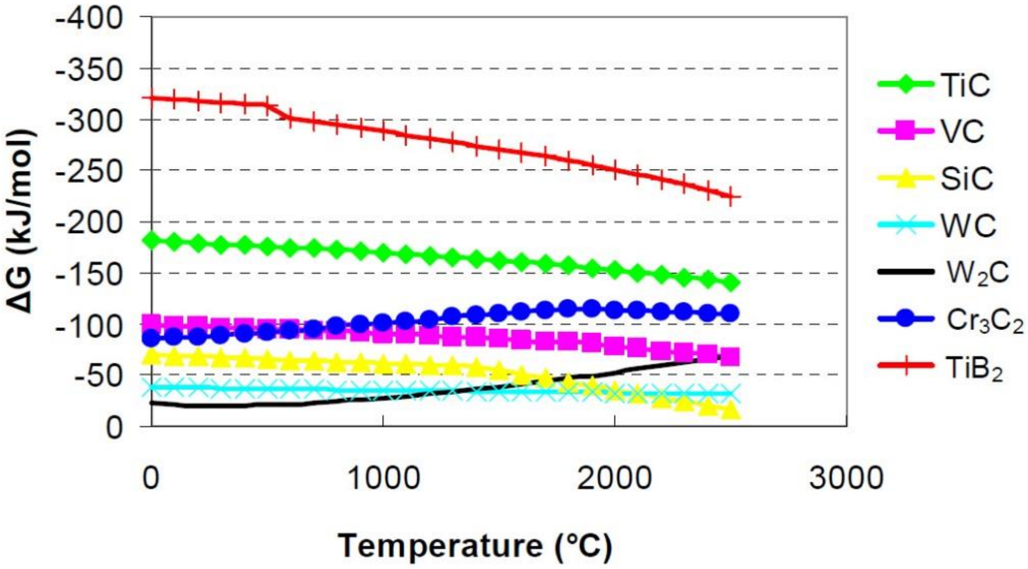

Figure 3.1 : Changes of Gibbs free energy of some particles used in producing MMC layers [32].

Addition to Gibbs free energy, the kinetics of dissolution of the reinforcement particles with respect to metal matrix should be taken into account when the risk of dissolution is considered [32]. Solubility of some common hard particles in nickel, cobalt and iron are shown in Table 3.2. Studies show that nickel-based hardfacing alloys dissolved WC less than cobalt-based hardfacing alloys [32, 127]. Also WC dissolved more heavily in cobalt-based alloys than in iron-based alloys [128]. Dissolution of carbides embrittle the matrix and decrease abrasive wear resistance of MMC layer.

Table 3.2 : Solubility of some hard particles in Ni, Co and Fe at 1250 °C [32].

	Solubility [wt% (mol%)]		
Carbide	Cobalt	Nickel	Iron
WC	22 (7.9)	12 (3.9)	7 (2.2)
TiC	1 (1.0)	5 (4.9)	<0.5 (<0.5)
VC	6 (5.6)	7 (6.6)	3 (2.7)
NbC	5 (2.9)	3 (1.7)	1 (0.53)
TaC	3 (0.93)	5 (1.6)	0.5 (0.15)

Tungsten carbide exists as WC, W_2C and WC_{1-x}. Tungsten mono-carbide has a very narrow range of homogeneity ($WC_{0.98}$-$WC_{1.00}$). If dissolution takes place, it forms Co_6W_6C, Co_3W_3C, Fe_3W_3C and $Ni2W_4C$ mixed carbides during cooling, depending on the used metal matrix [32].

TiC is more stable than WC or W_2C and has lower tendencies to dissolve in matrix. Solubility of TiC in cobalt-based hardfacing alloys is least when compared to those of it in nickel- and iron-based hardfacing alloys.

Chromium carbides (Cr_3C_2 and Cr_7C_3) have the lowest melting temperature between reinforcement particles. They usually melt and dissolve partly or fully into the melt pool, and precipitates in various forms (usually as needles) of CrC, Cr_7C_3 or $Cr_{23}C_6$ during cooling. Dissolution and formation of carbides promote brittleness of the matrix, which increases cracking tendency [32].

If there is a significant density difference between the reinforcement particle and the matrix, the solidified deposit will exhibit non-homogeneous properties. The low density of TiC caused the particles to float in cobalt-, nickel- and iron-based deposited hardfacing alloys, whereas WC or WC/W_2C particles sink in melt pool and segregated to the bottom of hardfacing layer the due to their higher density [107].

3.2.2 Volume fraction

It is well known that hardness and wear resistance of MMC hardfacing layers is directly related to the volume fraction of reinforcement particles. Increasing volume fraction of these particles decrease the mean free path between them and the area of soft matrix exposed to wear becomes smaller. High volume fraction of hard reinforcement particles leads to undesirable embrittlement, pores and uneven distribution in matrix [129]. Also by increasing volume fraction of particles the probability of their melting and dissolution and formation of new phases is increases during deposition process [130]. It was assumed that the formation of new phases which act as nucleation sites, contribute to a higher solidification rate and result in a smaller size solid solution matrix and eutectic phases [32, 107].

3.2.3 Particle size

The main contribution to excellent wear resistance of MMC hardfacing layers is provided by a homogeneous distribution of the reinforcement particles. Studies show that reinforcement with narrow particle size distribution gave the most homogeneous and uniform structure in deposition process. Wear resistance of MMC hardfacing layer depending on the wear mechanism can be influenced by reinforcement particle size. While coarse particles are better than fine ones in abrasive wear conditions, fine particles are beneficial in sliding wear conditions. The probability of melting of coarse reinforcement particles due to their smaller surface area to volume fraction is lower than the small particles during deposition process [32, 107] .

3.2.4 Morphology

Morphology of the powder particle depends on producing methods can be divided to angular and spherical particles. It is obvious that angular particles due to their sharp edge increase the cracking tendency compared to spherical ones [32].

3.2.5 Recent development in producing MMC hardfacing coatings

Frenk and Kurz added 5 wt% Cr_3C_2 into Stellite 6 alloy and deposited on steel by laser cladding method [131]. Microstructure analyses showed that Cr_3C_2 carbide was completely dissolved and altered the microstructure by formation of Cr_7C_3 carbide during the deposition process.

Zhong et al investigated the microstructural evolution in laser cladding of steel with Stellite 6+ WC powder mixture which WC particle was 0, 9, 18, 27, 36, 45, 54, 72 and 100 vol% [17]. In this study WC was introduced to melting pool by separate feeding hopper. In samples contacting 0 to 36 vol. % WC, the microstructure analyses show that added WC was completely melted in melt pool and re-solidified structure contained α-Co, σ-CoCr and Cr_7C_3 carbide. Increasing WC from 45 to 100 vol% which melted and dissolved in melt pool resulted in formation of various faceted dendrites in block, flower, butterfly and star shapes phases in addition to re-solidified WC, various type of complex carbides and Co-rich solid solution matrix.

The effect of addition of 20% SiC on microstructure of low carbon Stellite alloy hardfacing alloy (Co-28.6Cr-4.5W- 0.27C) deposited by laser cladding method is studied by Li et al [132]. Surveying microstructure showed that SiC is dissolved completely during laser cladding process under constant condition and leads to formation of Si_2W, CoWSi, Cr_3Si, $CoSi_2$ phases as a result of reacting C and Si with other elements existed in the alloy.

The microstructures and mechanical properties of PTA deposited hardfacing Stellite 21 mixed with 5, 10, and 20 wt% of VWC reinforcement particle was studied by Liu et al [20]. Addition of VWC depressed the FCC to HCP transformation of the Co-rich solid solution and also hindered the formation of $Cr_{23}C_6$ phase. Nano-indedntation test done on Co-rich solid solution showed that dissolution of V and W strengthened Stellite 21 matrix.

Xu et al used laser cladding technique for depositing mild steel with powder mixtures of Stellite 6 and vanadium carbide changing in the range of 0 to 100 wt% [16]. The microstructure and wear performance of hardfacing layer was investigated. Depending on the weight fraction of VC in the coating powder, two distinct microstructures can be formed. Hypoeutectic structures consisted of FCC Co-rich solid solution matrix and eutectic phases were found when the powder mixture contains less than 10 wt% VC. Hypereutectic structures were obtained with powders containing 20 to 100 wt% VC. These structures consist of primary VC grains and eutectic phases. The amount of the primary solidified VC phase increases and the eutectic structure becomes richer in complex carbides upon increasing weight fraction of VC. Although reinforcing Stellite 6 with VC particles enhanced its hardness and wear performance crack susceptibility is increased for the hardfacing layer deposited with VC contents higher than 80 wt%.

Chiang et al cladded Stellite 12 hardfacing alloy with different content of WC (10, 15, 20, 30 and 40 wt%) on carbon tool steel and studied the behavior of reinforcement particles [18]. The XRD analyses indicated the existence of α-Co, M_7C_3, $M_{23}C_6$ and M_6C (M=W, Cr, Co) in the Stellite 12 alloys with different WC contents when deposited on substrates by laser cladding. But depending on laser energy density different solidified microstructures were characterized. In cladding process with high laser energy density, WC particles were completely melted and fully dissolved in Stellite 12 melt pool and formed tungsten-rich carbides in addition to chromium-rich carbides and matrix. The EDX analyses indicated that the faceted dendrites (third phases) contain a majority of tungsten as well as some chromium, and cobalt, while the matrix contains more chromium and cobalt. In lower laser density energy in addition to α-Co, M_7C_3, $M_{23}C_6$ and M_6C phases, unmelted or partially melted WC were observed in microstructure.

Nurminen at al deposit Stellite 21 reinforced with WC, VC and TiC hard particle by laser cladding methods [133]. In this research abrasive wear behavior of MMC coating were investigated and microstructural analyses were not done in details.

Microstructure and hardness of laser cladded Stellite 6 reinforced with WC particles were investigated by Bartkowski et al [134]. Two different powder mixtures containing 30 wt% and 60 wt% of WC and three different values of laser beam power were used. In deposited MMC coatings WC, W_2C, M_7C_3, $M_{23}C_6$ and M_6C phases were detected. EDX analyses indicated that he chemical composition of these phases is most likely $(Co, W, Cr, Fe)_7C_3$, $(Co, W, Cr, Fe)_{23}C_6$ and $(Co, W, Cr, Fe)_6C$. Microhardness values of deposited layer showed increment by increasing amount of WC from 30 wt% to 60 wt%. Using high laser beam power resulted in decrease in hardness of layers due to melting and reduction of WC particles and dilution of iron from substrate.

4. WEAR PROPERTIES OF STELLITE ALLOYS

Stellite alloys are subjected to several distinct types of wear, which can fall into the following three categories: sliding wear, abrasive wear and erosive wear [14].

In sliding wear which two surfaces are in loaded contact, stresses are imposed on both solids as a result of normal and tangential forces. Frictional heat is also generated at the contact surfaces [14, 135]. In this respect the imposed stresses and frictional heating are the key driving forces for the occurrence of wear at a sliding surfaces of Stellite alloys so that their resistance depends on their ability to resistance deformation and fracture under contact pressure and their oxidation behavior at various working temperature [11, 136]. Sliding wear generally occurs by one or more of two mechanisms.

The first mechanism of sliding wear, which can also produce substantial metallic damage, is plastic deformation and fatigue. This mechanism is associated with cyclic stress conditions caused by materials periodically pressing on one another. Material is worn through remarkable plastic deformation and fatigue crack nucleation [14, 19, 60, 137].

The second mechanism, which oxide controls the sliding wear process, is experienced when surface temperatures are high due to frictional heating under conditions of high loads and sliding speeds, or due to the application of external heat at high ambient temperatures. It is well known that oxidation of the metals can influence the wear processes, causing significant changes in the overall wear rates.

Depending on nature of oxide film (protective or non-protective) influenced by chemical composition of sliding solids, ambient temperature and wear parameter, wear loss can be decreased or increased [135]. If thin and non-adherent oxide films form on contacting surfaces they may be removed completely, producing oxide wear debris and exposing clean metal to the environment; this is then reoxidized to form further oxide, and the process is repeated which leads to more wear loss [135, 138-140]. Also if the broken oxide debris particles are hard compared with the sliding components, they may be retained as freely moving particles between the contacting surfaces where they may act as three body abradents, causing abrasion damage to both surfaces [139, 140].

More durable, adherent and thick oxide films can give protection against further wear damage by reducing direct contact of sliding surfaces. Although sometimes oxide films may be deformed and fractured under high load sliding wear conditions but the particles fragmented to a small enough size, can be agglomerated at some sites on the worn surfaces, particularly in grooves, due to the adhesion forces between solid surfaces originating from surface energy, to form relatively stable compact layers called “oxide glazes”. It is should be noted that in this case the agglomeration, compaction and sinterability of debris play a crucial role on protecting the worn surface. If fragmented oxides debris show less degree of sinterability they cannot be effective on reducing wear loss [141].

In abrasive wear which ploughing takes place, hard particles are forced against and moved relative to a surface of a component and results in removing certain volume of surface and formation of micro grooves. Abrasive wear occurs under two conditions: high stress and low stress abrasion. The terms high stress and low stress abrasion relate to the condition of the abrasive particles after interaction with the surface. If the abrasive medium is crushed, then the high stress condition is said to prevail. If the abrasive medium remains intact, the process is described as low stress abrasion. Typically, high stress abrasion results from the entrapment of hard particles between metallic surfaces. Abrasive resistance of Stellite hardfacing alloys is influenced by the size and shape of the hard phase formed within the microstructure, and the size and shape of the abrading species [11].

Erosive wear can be classified into solid-particle erosion, slurry erosion or liquid solid particle erosion, liquid droplet erosion, and cavitation erosion. The first two types of erosion are caused by the impingement of small, solid particles against a surface. With the complex mechanisms of the solid particle and slurry erosions, however, the general abrasion mechanism may not be warranted. For example, in solid particle erosion, ductility of Stellite alloys can also be an important factor. As for the last two types of erosion, the performance of Stellite alloys largely depends on their ability to absorb the stress waves without microscopic fracture. Therefore the properties of matrix are more important than carbide volume fraction which has very little effect on resistance to liquid droplet and cavitation erosion [11].

4.1 Sliding Wear of Stellite Alloys

Aoh et al studied sliding wear behavior of PTA deposited Stellite 6, Stellite 21 and Stellite 6+30 wt% Cr_2C_3 deposited coating by PTA technique [142]. The results of pin-on-disk wear test done at various conditions show that Stellite 6 with Cr_2C_3 showed the best wear resistance at elevated temperature (200 and 450 °C), followed by Stellite 6 and Stellite 21. Chromium carbide phase strengthening were the main mechanisms for the superior wear property of Stellite 6+30 wt% Cr_2C_3 examined coating at elevated temperature. Also founding show that pre-oxidation of samples at 700 °C decreased their wear resistance.

The results of investigation done by Persson et al showed that in sliding wear of Stellite 21 which two identical specimens slides against each other under high load sliding condition, FCC→HCP transformation occurs and control the wear mechanism in air and argon atmosphere [143].

Effects of addition of yttrium on the hardness and wear performance of Stellite 6 at elevated temperatures were investigated by Wang and Li [117]. The enhancement in hardness and room temperature wear resistance of yttrium containing Stellite 6 alloy can be attributed to the finer microstructure and the formation of Co_2Y phase in the microstructure. Alloying yttrium particularly improved the resistance of Stellite 6 at elevated temperatures. The oxide film on Stellite 6 mainly consisted of cobalt and chromium oxides. When yttrium was alloyed into the alloy, its oxide scale contained Y_2O_3 phase. The oxide scale of Y-containing Stellite 6 alloy exhibited improved mechanical behavior and higher resistance to scratch failure. However, too much yttrium did not benefit the oxide film [117].

Wear performance of TiC and TiC-Ni reinforced Stellite 712 samples produced by HIP method was investigated by Ning et al [51]. Results of room temperature wear tests conducted on pin-on-disc tribometer showed that the developed composites with bare TiC reinforcement exhibited higher wear resistance than pure Stellite 712 alloy but those with Ni-coated TiC exhibited lower wear resistance. The Ni coating on the TiC particles reduced the bonding strength between the reinforcements and the matrix and leading to the reduction of wear resistance.

Radu and Li studied the effect of addition of yttrium (0.5 and 5 wt%) on sliding wear performance of Stellite 21 at elevated temperatures (600 °C) in air and argon environment [118]. The research demonstrated that a stronger and more adherent oxide film could markedly benefit the wear resistance of Stellite 21, leading to lower wear of the alloy in air than in the argon environment. An improved oxide film by yttrium rendered the oxide film more protective. However, the oxide film became less protective as the wearing force was increased. Under high loads, the oxide film was relatively easier to be destroyed and the cycle of oxidation–oxide removal–reoxidation could accelerate wear or result in more wear in air than in argon. Also the results of pin-on-disc wear tests show that 0.5 wt% addition of yttrium to Stellite 712 was beneficial to its sliding wear resistance due to superior mechanical properties of oxide films that formed on the surface of examined samples at 600 °C [4]. Generally alloying of Stellite 21 and Stellite 712 alloys with less than 1% yttrium noticeably enhances mechanical properties of oxide film which improves wear performance of them at elevated temperature.

Wear performance of molybdenum containing Stellite alloys (CoCrMoC) and tungsten containing Stellite alloys (CoCrWC) conducted on block-on-ring and pin-on-disc tribotester at room temperature was investigated by Yao et al [48, 62]. Better wear resistance of molybdenum containing Stellite alloy in comparison to tungsten containing Stellite alloy were attributed to formation of large amount of carbide and intermetallic compounds in its microstructure.

High temperature sliding wear behavior of Stellite 6 alloy versus iron-based hardfacing alloy and Stellite 6 alloy studied by Inman et al indicates that between room temperature and 390 °C where the Stellite 6 sourced oxides did not form glaze, the abrasive nature of the loose oxides generated further promoted Stellite 6 wear [141]. At elevated temperature (450 °C and greater) preferential oxidation of cobalt and chromium due to their more negative free energy of formation enhanced wear performance of Stellite 6.

Liu et al improved sliding wear performance of low carbon contacting Stellite 21 by addition of VWC hard particles [20]. In this study VWC particles and Stellite 21 powder are mechanically mixed and then deposited on base materials by using PTA method. Matrix of alloy was strengthened due to dissolution of vanadium and tungsten from VWC particle into the Stellite 21 matrix. The hardness and wear resistance of Stellite 21 at RT were improved significantly by adding VWC, and they increased with the content of VWC in the composite.

Kashani et al studied RT and high temperature wear resistance of Stellite 6 and Stellite 21 deposited on H11 steel substrates using tungsten inert gas welding (TIG) process on a pin-on-disc tribotester [144]. At RT Stellite 6 showed better wear resistance than Stellite 21 due to its higher hardness. However at testing temperature of 550 °C, formation of compact oxide layers which act as load-bearing areas and lower contact stresses, played a crucial role in reducing wear loss comparing to those of room temperature. Stellite 21 exhibited lower wear than Stellite 6 at high testing temperature. Also tribological studies of Stellite alloys at different temperature indicated that at room temperature in addition to their higher hardness, higher work hardening due to FCC→HCP strain-induced transformation has contribution on their wear resistance when compared to high temperature wear tests (200 °C). Increase in temperature increases the stacking fault energy of the alloy, hence decreases the martensitic transformation and work hardening ability [64].

Opris et al investigated ball-on-disc wear resistance of Stellite 694 and Stellite 712 composites developed with the reinforcement of 20 wt% titanium carbide particles by powder metallurgy method [145]. It was found that the composites had much higher hardness and wear resistance than the corresponding base alloys.

Birol showed that the adhesive Cr_2O_3 layer growing slowly on Stellite 6 alloys during ball-on-disc tribotester reduces the wear action and damage without spalling and are claimed to be responsible for the superior wear resistance of this alloys at 750 °C [146].

The tribological behavior of Stellite 6 was studied during rotational sliding wear test at 600 °C. Results showed that cobalt and chromium elemental diffuse to the surface of sample and forms cobalt and chromium dominated oxide layer. By increasing wear testing time chromium-rich layer at the surface of sample continued to thicken which this phenomenon would lead to a chromium depleted layer under the oxide layer [147].

Kapoor et al studied wear performance of some Stellite alloys from RT to 450 °C [60]. Pin-on-disc wear test results indicated that wear resistance of Stellite alloys at RT mainly depends on their carbon and other alloying elements such as tungsten. Reduction in wear resistance of examined alloys at 250 °C was related to softening of the solid solutions matrix of Stellite. Increasing tungsten and chromium content can improve the hardness stability of the solid solution and wear performance of Stellite alloys at high temperatures.

Sliding wear resistance of high tungsten containing Stellite alloy was compared to Stellite 6 and Stellite 3 by using pin-on-disc tribotester. Results showed that formation of large amount of tungsten containing complex carbide in produced alloy was beneficial to wear resistance properties and decreased its wear loss compared to Stellite 6 and 3 remarkably [120].

4.2 Abrasive Wear of Stellite Alloys

Abrasive wear behavior of Stellite alloys were investigated by Silence [57]. The results of this study indicated that abrasive wear resistance can be maximized through appropriate processing so as to maximize the particle size of the hardest constituents.

The effect of solidification rate of Stellite 6 produced by casting and laser cladding method (with low, medium and fast cooling rate) on its sliding wear resistance investigated by Frenk and Kurz [131] . Fast cooling of studied alloy resulted in refinements in microstructure which leads to higher hardness but has little influence on the wear rate. Lower dilution from substrate increased wear resistance of coating remarkably. Also addition of 5 wt% Cr_2C_3 enhanced wear performance of Stellite 6 alloy in laser cladding.

Shin et al showed that addition of molybdenum enhanced the hardness and abrasive wear resistance of the Stellite 6 hardfacing alloys deposited by PTA [7]. Formation and increasing volume fraction of M_6C complex carbide as well as the refinement of Co-rich dendrites and Cr-rich carbide was responsible for the improvement of the mechanical properties such as hardness and abrasive wear resistance of examined molybdenum containing Stellite 6 alloy.

Celik and Kaplan investigated the effects of addition of silicon (2.2, 3.1 and 4.2 wt%) on the abrasive wear behavior of Stellite 6 alloy at different temperature varying between room temperature to 800 °C [148]. The hardness and room temperature abrasive wear resistance of Stellite 6 alloy increased with silicon addition. Addition of silicon decreased the wear resistance of Stellite 6 at elevated temperature. Correlation has been found between hardness and wear resistance of the materials studied at room temperature.

Yao showed that replacing tungsten with molybdenum results in changes in the carbide morphology and increased volume fraction of carbides in the microstructure which enhanced the abrasive wear resistance of Stellite alloys [48]. Formation of large amount of carbide in molybdenum contacting Stellite alloy is related to relatively smaller atomic size and much lighter atomic weight that promote mobility of molybdenum in melt pool during solidification.

The effect of producing method on abrasive wear resistance of hyper-eutectic Stellite alloy was studied by Yu et al [47]. The casted samples with large carbide particles showed better abrasive wear resistance than the HIPed samples which contained finer particles. Brittle fracture of the carbides and ploughing of the matrix were the main wear mechanisms for the cast alloy, whereas for the HIPed samples, ploughing and carbide pullout were the dominant wear mechanisms.

The abrasive wear performance of laser cladded Stellite 21 reinforced by addition of TiC, WC and VC particles was studied by Nurminen et al [133]. Results showed that TiC and WC containing Stellite 21 alloy yielded better wear resistance compared to VC containing one.

From these investigations it can be concluded that abrasive wear resistance of Stellite alloys at room temperature can be enhanced by increasing volume fraction and particle size of carbides or intermetallic compound and also addition of hard reinforcement particles.

4.3 Erosive Wear of Stellite Alloys

The results of erosion test done under low angle impingement conditions, indicated that tungsten containing alloy Stellite 12 yielded better resistance compared with the molybdenum containing Stellite 712 [48].

Erosive behavior of Stellite alloy 706 which contains 5 wt% molybdenum with Stellite alloy 6 which contains 4.8 wt% tungsten, both produced in casted and HIPed form, was investigated by Malayoglu and Neville [56]. Results show that molybdenum is much more effective than tungsten in conferring erosion resistance to cobalt-based alloys due to formation of molybdenum rich carbides.

In a research done by Shivamurthy et al, chip formation, chip fracture, microcutting, plowing, and crater lip and platelet formation were observed as a erosive wear mechanism for Stellite 6 coatings [149].

High tungsten containing Stellite alloy was produced by Liu et al and conducted on erosive wear test under various particle impact velocities and impingement angles [120]. The experimental results show that examined alloy has superior solid-particle erosion resistance compared to Stellite 3 and Stellite 6, owing to the formation of large amounts of large-size tungsten rich carbides in the alloy.

It is obvious that addition of elements which form more and hard carbides or intermetallic compounds in the microstructure can improve erosive wear resistance of Stellite alloys.

From these studies it can be understood that work hardening, volume fraction and type of carbides or intermetallic compound formed in the microstructure and also introducing reinforcement particles have significant effect on the sliding wear resistance of Stellite alloys at room temperature. Meanwhile formation of adherent and continuous oxides of cobalt and chromium can be remarkably beneficial in increasing wear resistance of Stellite alloys at high temperature.

Also it can be concluded that abrasive and erosive wear resistance of Stellite alloys at room temperature can be enhanced by increasing volume fraction and particle size of carbides or intermetallic compound and also addition of hard reinforcement particles.

Although the effect of addition of alloying elements and reinforcement particles on different kind of wear behavior of Stellite alloys such as Stellite 6 and low carbon Stellite alloys at RT were studied and promising enhancements have been reported but there is lack of information about the sliding tribological behavior of alloying added and hard particle reinforced Stellite 12 coatings at elevated temperature.

5. EXPERIMENTAL PROCEDURE

The present chapter will summarize the procedures followed in the experimental studies to achieve the objectives of this thesis. For this purpose, initial powders characteristics, deposition of the coatings and finally characterization of coatings will be explained.

5.1 Initial Powder Characteristics

The coating quality therefore coating properties are determined by the coating's microstructure which strongly depends on feedstock powder characteristics and PTA deposition parameters. For this reason, the current section of this thesis will describe the initial powders characteristics such as morphology and particle size distribution. The characterizations of the initial powders were made by means of X-ray diffraction (XRD) analyses, scanning electron microscopy (SEM) and particle size distribution. The powders used in this study are commercially available Stellite 12 (Kennametal), molybdenum (Amdry 313, Sulzer, purity > 99.5 %), nickel (Metco 56C-NS, Sulzer, purity > 99.3 %), WC/W_2C (ThyssenKrupp), TiC (American Elements) and Cr_7C_3 (London & Scandinavian Metallurgical Company). The nominal composition of the Stellite 12 alloy powder is listed in Table 5.1.

Table 5.1 : Nominal Composition of Stellite 12 Powder (wt%).

Co	Cr	C	W	Ni	Si	Fe	Mn
Balance	29.5	1.65	8.5	2.9	1.5	2.4	1

Figure 5.1 present the XRD patterns of the powders used for preparing the feedstock powder mixtures. The typical morphologies of powders are shown in Figure 5.2. Stellite 12 has spherical morphology, typical of metallic powders produced using a gas atomizing process. Molybdenum with spherical and nickel with globular morphologies are produced by agglomerated/densified and precipitated methods, respectively. The morphologies of WC/W_2C, TiC and Cr_7C_3 particles are angular with sharp edges.

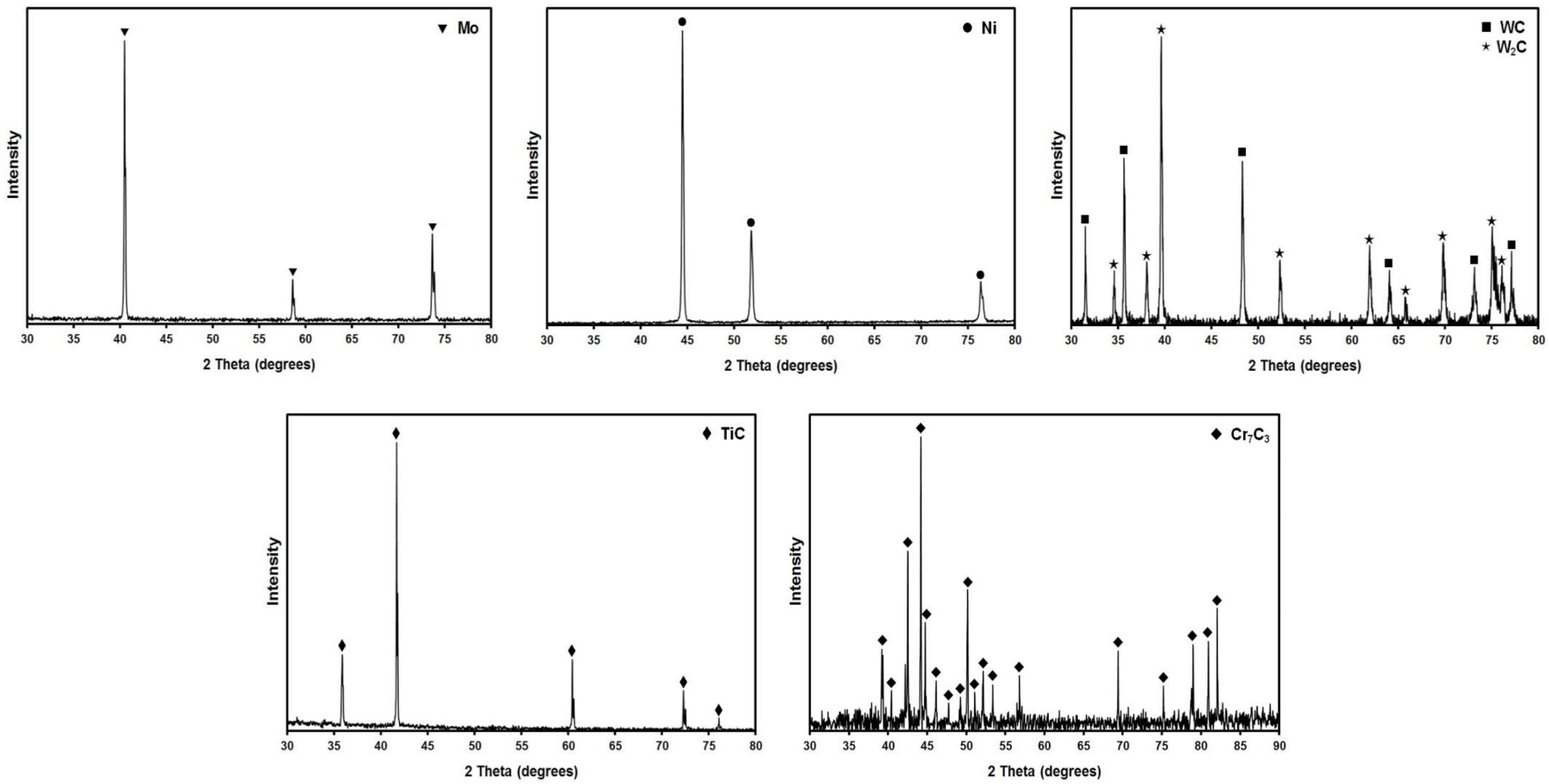

Figure 5.1 : XRD patterns of the powders used for preparing the feedstock powder mixtures.

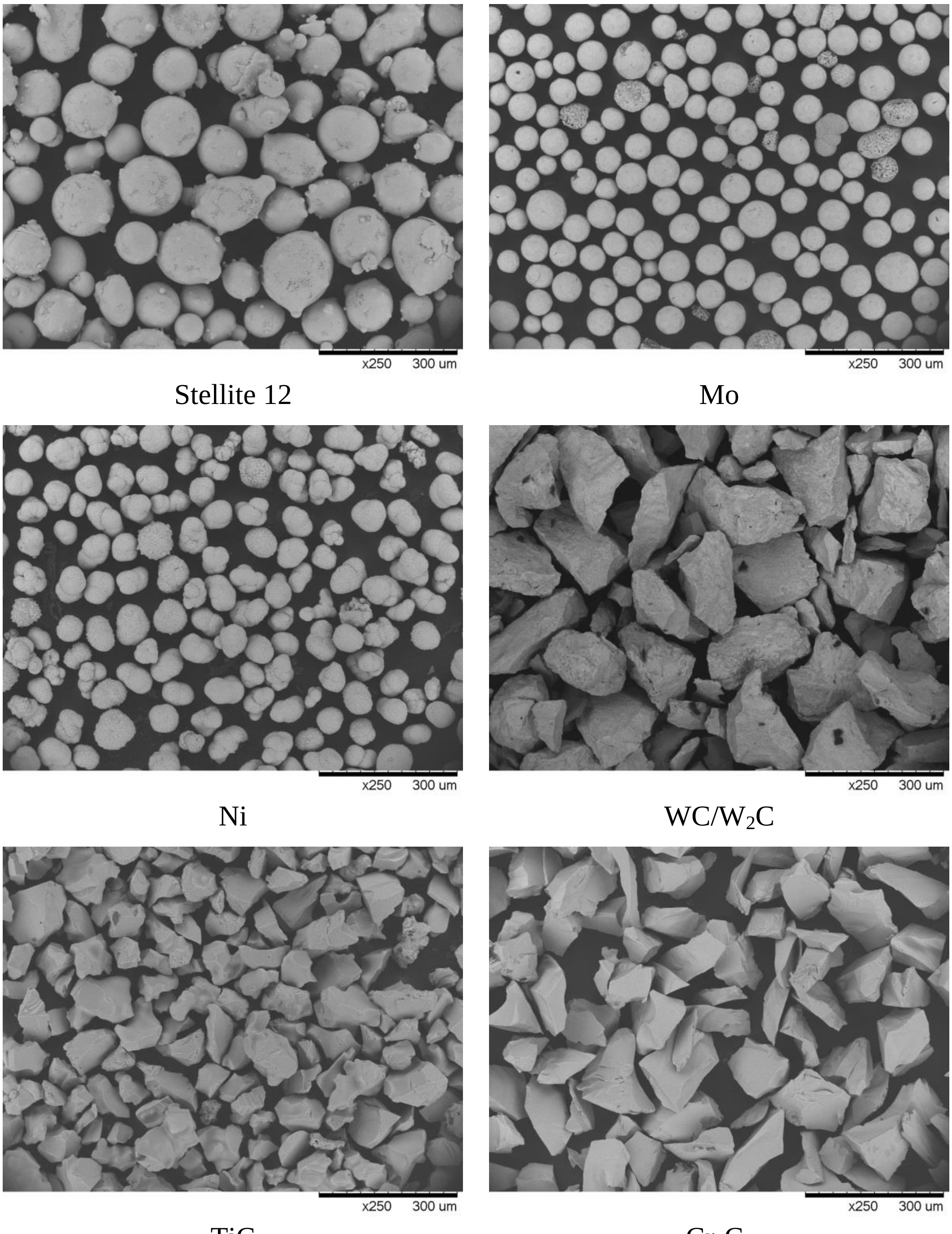

Figure 5.2 : Morphologies powders used for preparing the feedstock powder mixtures.

Particle size distributions were determined utilizing a Mastersizer 2000 Malvern laser diffraction particle size analyzer by dispersing powders in deionized water and results are presented in Figure A.1. Stellite 12 powders is composed of particles ranging from 75 to 145 μm in diameter and has average diameter of 104 μm while particle size of molybdenum and nickel powders ranges between 46-85 and 48-90 μm with a mean size of 63 and 66 μm respectively. Also WC/W_2C, TiC and Cr_7C_3

particles are in the size range of 68-155, 70-150 and 67-151 μm with an average particle size of 103, 102 and 101 μm respectively.

5.2 Deposition of the Coatings

The PTA deposition equipment used in this study is a fully automated machine made in Hettiger Stellite Company. The PTA machine is composed of a powder hopper, power supply unit, cooling system and welding torch which is moved by a computer controlled three-axis displacement system. Argon gas with purity of 99.995 was used as plasma gas, carrier and shield gas. An overall view of the PTA machine is shown in Figure 5.3.

Figure 5.3 : An overall view of the PTA machine.

Stellite 12 powder was mixed with Mo, Ni powders and WC/W_2C, TiC and Cr_7C_3 particles separately to make feedstock materials. While Mo and Ni were added 2, 6 and 10 (wt%), WC/W_2C, TiC and Cr_7C_3 were added 2, 6 and 10 (vol%) ratios. Prepared powders were deposited on 4140 steel specimen machined into a rectangular block with a slot, as shown in Figure 5.4. Prior to deposition, the surface of the substrate was cleaned with acetone in order to remove any contaminants and heated up to 200 °C. The PTA deposition process was carried out in a single layer with a thickness of 5 mm under constant conditions which were presented in Table 5.2.

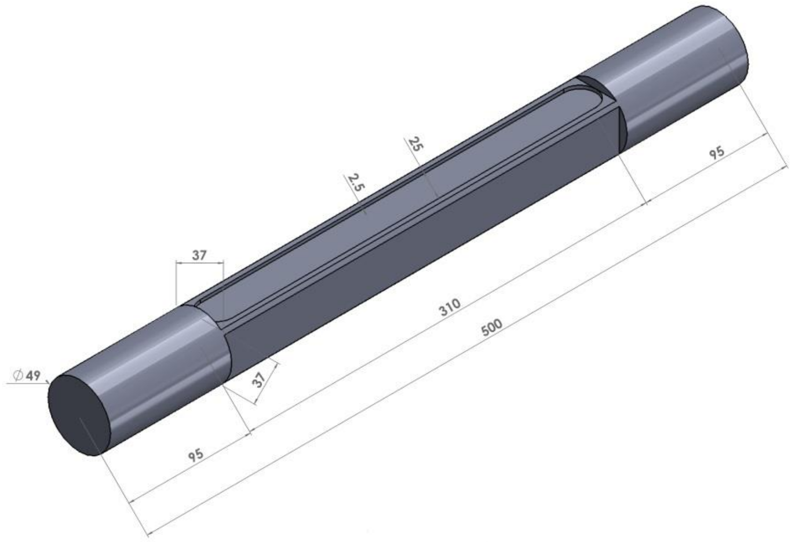

Figure 5.4 : Dimension of specimens machined into rectangular with slotted bar.

Table 5.2 : Processing conditions for PTA deposition.

Parameters	Values
Welding Current (A)	92
Voltage (V)	30
Plasma Gas Flux (l/ min)	3
Protective Gas Flux (l / min)	20
Feeding Gas Flux (l/ min)	3
Welding Speed (mm/ min)	85
Powders Feed Rate (g/min)	24

5.3 Characterization of the Coatings

After PTA welding, the surfaces of specimen were machined to make a flat hardfacing layer with a thickness of 2.5 mm for characterization and wear test.

Microstructural characterization was carried out by scanning electron microscope (SEM) examinations and X-ray diffraction (XRD) analysis. Microscopic examinations were conducted on the cross-sections of the coatings after preparing the samples according to standard metallographic method and etching with 80% HCl+20% H_2O_2 solution. Standard metallographic method consists of sectioning, mounting in a thermoset epoxy, grinding of samples with SiC paper and polishing with 0.25 μm diamond paste. Scanning electron microscopes used in this study are energy dispersive X-ray (EDX) spectrometer equipped Philips SFEG, JEOL JSM-6010LV and Hitachi TM-1000.

X-ray diffraction analysis was conducted on a GBC X-Ray Diffractometer at a generator voltage and current of 35 kV and 28.5 mA, respectively. Cu K_α radiation was used to irradiate the coatings. The X-ray diffraction was performed at a speed of 1 degree per minute with a step-scan size of 0.02°, at angles (2θ) between 10° and 90°.

Mechanical properties of the coatings were determined by hardness measurements and wear tests. Surfaces of coatings were ground with SiC papers and polished with 1 μm diamond paste in order to remove surface roughness prior to hardness measurements and wear tests.

Shimadzu HMV2 micro hardness tests, with a Vickers indenter and under a load of 2 kg, were used for hardness measurements. Five measurements were made on the surfaces of each coating and the average was the final result of hardness. Furthermore, CSM depth sensing indentation tester was conducted on the matrices of coatings under load of 100 mN with a Vickers pyramid indenter.

Wear tests were performed by using a CSM high temperature ball-on-disc type tribometer under normal load of 3 N at RT, 300, 500 and 700 ºC and 32±3% relative humidity. A ball made of alumina (Al_2O_3) with diameter of 6 mm was used as the counter-face under dry sliding contact conditions. Sliding speed was set at 0.1 m/s. Al_2O_3 ball followed a circular path of 5.5 mm in radius for the total sliding distance of 500 m over the surfaces of the samples. The test procedure involved ultrasonic cleaning of the specimens in acetone before each experimental run. The samples were heated in ambient conditions and the test was started when the desired temperature was reached. At least three tests were run under the same conditions for each sample to ensure the reproducibility of data. The frictional force data was continuously recorded during the wear tests. By the end of the tests, wear tracks developed on the surfaces of the samples were monitored using a 2-D contact surface profilometer (Dektak-6M, Veeco, USA). Profilometric measurements were made at eight different locations of each wear track. After determining the average depth and the width of each wear track, wear loss of the samples were calculated by multiplying the average cross-sectional area of wear track with its circular length. Worn surfaces of the samples were also examined by the EDX equipped Philips SFEG and JEOL JSM-6010LV SEM and Raman spectroscopy (Renishaw, inVia Reflex spectrometer, UK) using an excitation wavelength of 532 nm.

6. RESULTS AND DISSCUSION

6.1 Stellite 12 Coating

6.1.1 Microstructural characterization

Figure 6.1 shows a cross-sectional microstructure of Stellite 12 coating deposited by PTA method. In general, microstructure exhibited characteristic feature of hypo-eutectic Stellite hardfacing alloys consisted of dendritic matrix (light gray region) and compounds appeared in dark gray and white colors in lamellar morphology in the interdendritic region.

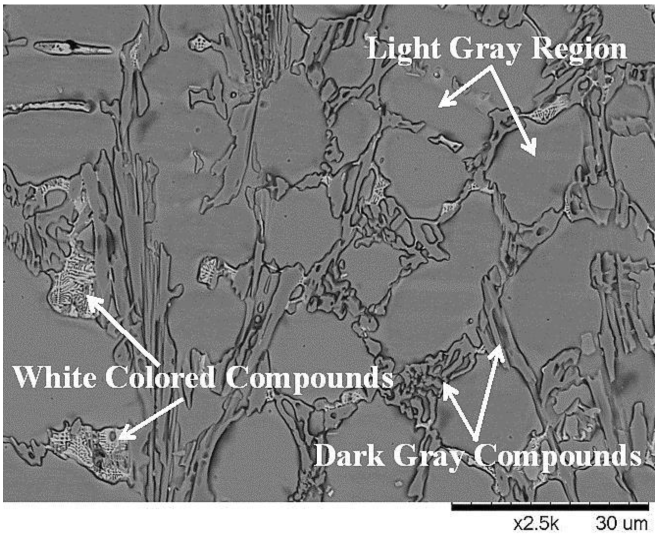

Figure 6.1 : Cross-sectional SEM micrograph of Stellite 12 coating.

Elemental X-ray mapping and the results of EDX analyses of the microstructural constituents along with their average volume fractions quantified by linear intercept method are presented in Figure 6.2 and Table 6.1, respectively. According to Figure 6.2 and Table 6.1, the dendritic matrix of the Stellite 12 coating mainly consisted of cobalt and chromium with a few amounts of dissolved tungsten, nickel and iron (i.e. Co-rich solid solution). While the dark gray compounds can be identified by their high chromium content, the white compounds mainly consisted of cobalt, chromium and tungsten.

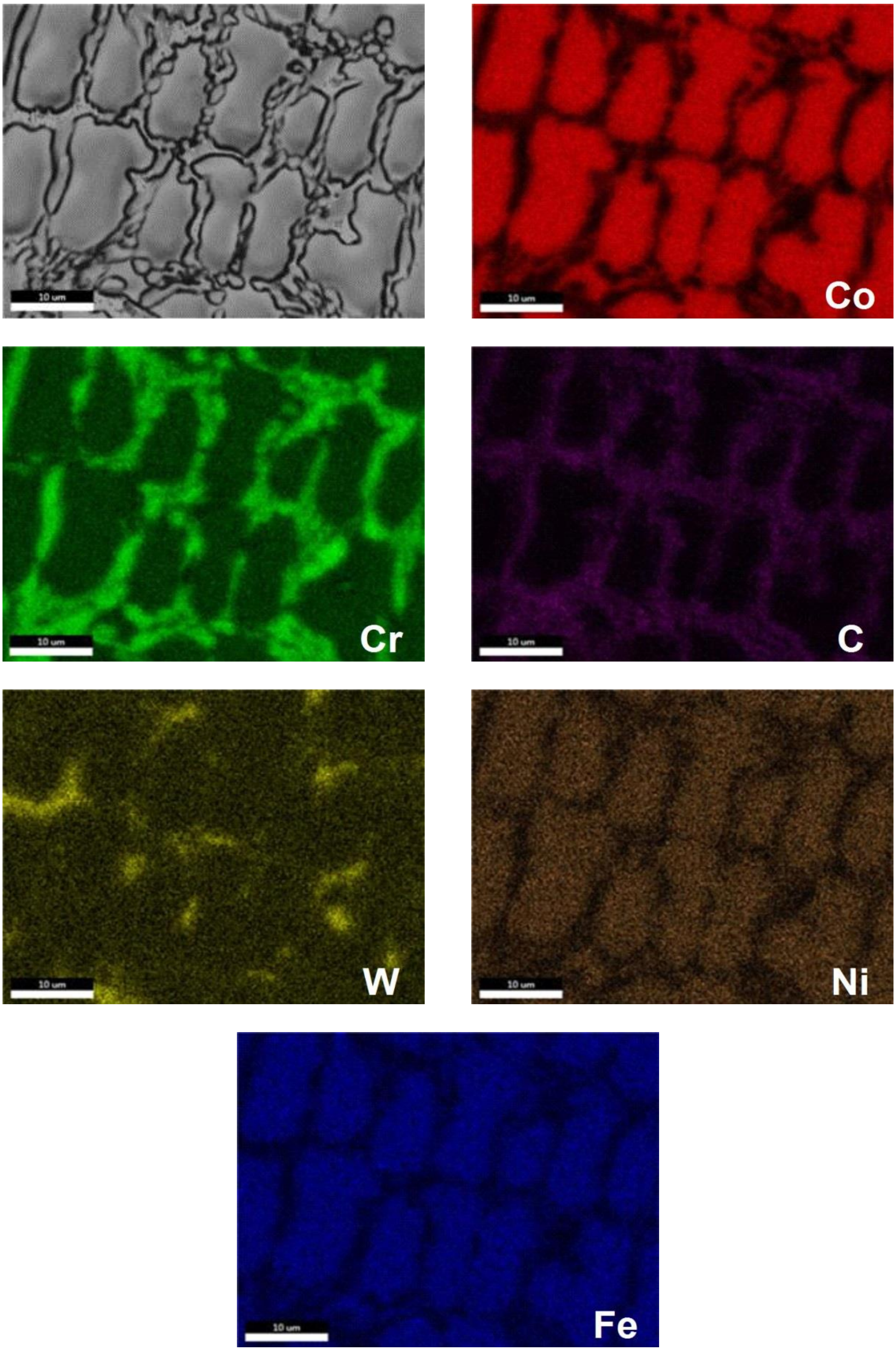

Figure 6.2 : Elemental X-ray mapping of Stellite 12 coating.

Table 6.1 : Composition and volume fraction of the constituents present in the microstructures of Stellite 12 coating.

Coating	Microstructural constituents	Vol %	Co (at%)	Cr (at%)	W (at%)	Ni (at%)	Fe (at%)
Stellite 12	Dendritic matrix	58.8	63.40	27.12	1.76	2.17	5.55
	Dark grey colored compounds	35.6	21.01	76.35	2.64	---	---
	White colored compounds	5.6	46.44	40.63	12.93	---	---

XRD patterns of the Stellite 12 coating is presented in Figure 6.3. When the results of XRD (Figure 6.3) and EDX analyses (Table 6.1) are combined, light gray colored matrix and dark gray compounds appeared in the microstructure of Stellite 12 coating (Figure 6.1) were identified as α-Co (FCC) and Cr-rich carbides (Cr_7C_3 and $Cr_{23}C_6$) , respectively. Any peak related to the white colored compounds, which were quantified about 5.6 vol% in the microstructure of Stellite 12 coating (Table 6.1), did not appear on the relevant XRD pattern (Figure 6.3). According to the literature, these compounds could be Co/W-rich carbides and/or intermetallics [15, 18, 19, 56].

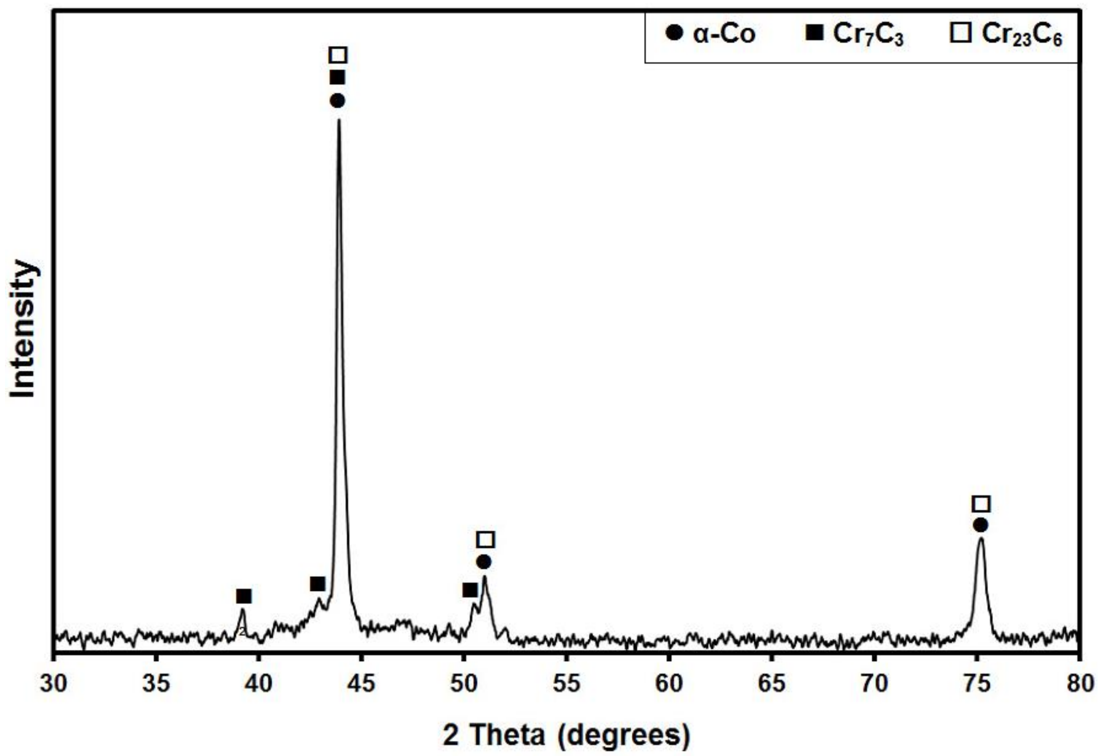

Figure 6.3 : XRD pattern of Stellite12 coating.

It is well documented that cooling of the PTA deposited Stellite12 coating from the liquid state involves primary Co-rich solid solution dendritic matrix and the remaining liquid eventually solidifies by a eutectic reaction into a lamellar mixture of Co-rich solid solution phase with Cr-rich carbides (Cr_7C_3 and $Cr_{23}C_6$), Co/W-rich complex carbides (Co_3W_3C, Co_6W_6C) and intermetallics (Co_3W, Co_7W_6) in the interdendritic region [19, 47, 147]. However the difference between Cr_7C_3 and $Cr_{23}C_6$ carbides and also between Co/W-rich complex carbides and intermetallics are not readily distinguishable under a microscope. Also it is noticeable that sluggish transformation of FCC to HCP phase in cobalt-rich dendritic matrix results in the presence of a dendritic matrix as a mixture of α-Co (FCC) and ε-Co (HCP) at room temperature due to alloying elements in Stellite hardfacing alloys [64, 119, 144]. But no intensive and distinct peak related to a ε-Co (HCP) phase was detected in this study. Difficulties in detecting peaks of ε-Co (HCP) phase can be attributed to its low amount in deposited coating.

6.1.2 Hardness

Room temperature hardness test was conducted on the surface of PTA deposited coatings by means of a Vickers microhardness tester at a load of 2000 g. The average hardness of the Stellite 12 was reported 490 ± 10 HV_2. Generally type and amount of carbide or intermetallic compounds developed during solidification have a significant influences on mechanical properties of Stellite alloys [145, 150].

6.1.3 Wear

The representative 2-D profiles of the wear tracks formed on the surfaces of the PTA deposited Stellite 12 coatings and recorded friction coefficient curves during sliding wear at RT and elevated temperatures are depicted in Figure B.1. The depth and width of the wear tracks (i.e. wear track area) varied remarkably with the testing temperature. In the examined coating, testing temperatures of 300 and 500 ^{o}C induced lager wear track areas than those formed at RT and 700 ^{o}C. After measuring the width and depth of wear tracks, the results of the wear tests were quantified in terms of wear loss and listed in Table 6.2 along with mean values of the friction coefficient. As a general trend, lower friction coefficient values were obtained for examined coatings at elevated temperatures compared to those at RT.

Table 6.2 : Wear loss and friction coefficient values of the PTA deposited Stellite 12 coating at various testing temperatures.

	RT	300 °C	500 °C	700 °C
Stellite 12	Wear Loss (mm^3)×10^{-3}			
	6.45	408.20	327.40	41.70
	Friction Coefficient			
	0.91	0.50	0.63	0.53

Worn surface topographies and EDX patterns taken from the worn surfaces of Stellite 12 coating and corresponding contact surface appearances of the counter-face (Al_2O_3 ball) are illustrated in Figure 6.4 and Figure 6.5, respectively. The worn surfaces of the coatings tested at RT can be characterized by accumulated plastic deformation resulting from cyclic sliding contact. The sliding action of the Al_2O_3 ball at 300 °C imposed plastic deformation along with scratches aligned in the direction of motion on the worn surfaces of the coatings. As it is obvious in Figure 6.4 the progress of wear by the plasticity dominant mechanism on the coatings at RT and 300 °C was accompanied by material transfer to the contact surface of the Al_2O_3 ball to cause a dark colored wear scar appearance.

It is well document that hardness, type and volume fraction of carbides and/or intermetallic compounds formed during solidification of Stellite alloys play a crucial role on tribological performance of deposited coatings [7, 62, 80, 151]. Furthermore work hardening of cobalt-rich solid solution matrix at the contact surface during wear testing contributes to the wear resistance of Stellite alloys at RT [65, 152, 153]. It is reported that, a reduction in the work hardening rate and mechanical strength [60, 64, 152, 153] and/or easy destruction of thin and less adherent oxide films [118, 138, 154] covering the worn surface of examined coating accelerate the progress of wear on Stellite alloys at moderate temperatures (< 400°C). In this respect, the disappearance of the accumulated plastic deformation zones at the worn surfaces of the coatings tested at 300 °C (Figure 6.4) can be associated with the softening and the ineffectiveness of work hardening under sliding contact, in addition to the scratching effect of the fragmented oxide film and/or oxidized metallic wear debris, which acted as third body abradents. The reduction in strength of coating and the rolling of debris particles between mating surfaces resulted in remarkably lower friction coefficient values at 300 °C as compared to RT (Table 6.2). It should be noted that, due to the thin and less adherent nature of the oxide film, no remarkable difference in oxygen content on the worn surfaces was identified after wear testing at RT and 300 °C (Figure 6.4). On the other hand, the appearance of a wear scar on the Al_2O_3 ball indicates that the progress of wear on the coatings at 300 °C was accelerated by the additional contribution of the adhesive material transfer.

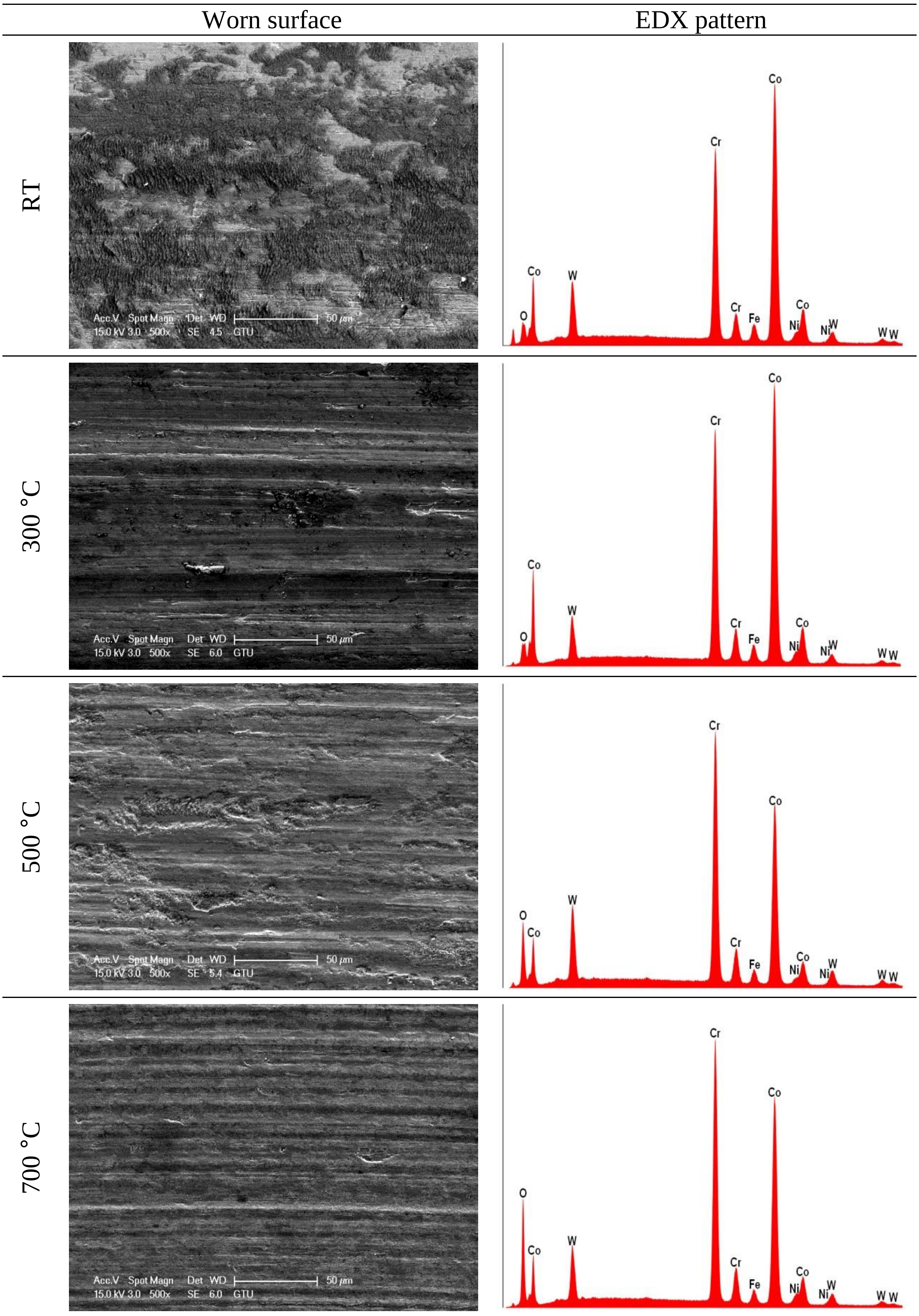

Figure 6.4 : The worn surface topographies and related EDX patterns of Stellite 12 coating after the wear tests at different temperature.

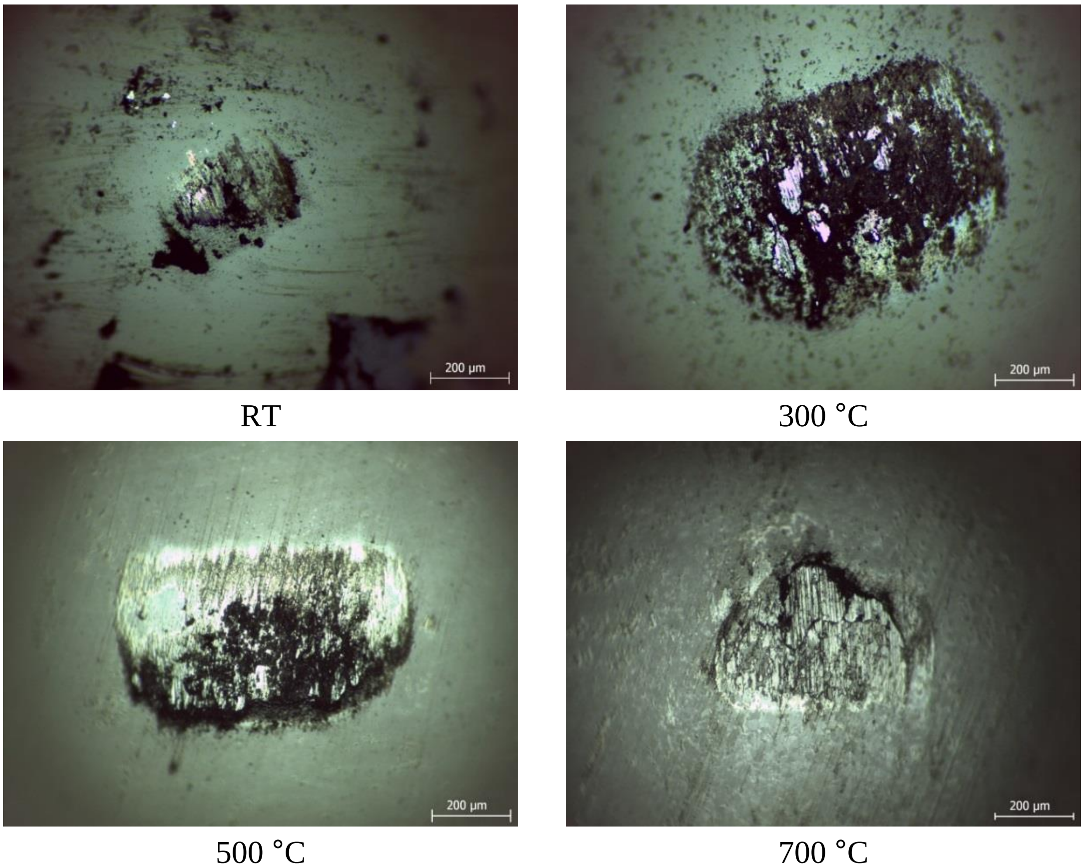

Figure 6.5 : Corresponding contact surface appearances of the Al_2O_3 ball after the wear testing of Stellite 12 coating at different temperature.

Unlike RT and 300 °C, the worn surfaces formed at 500 and 700 °C can be characterized by the formation of an oxide film as also confirmed by the evidence of strong oxygen peaks on the relevant EDX patterns (Figure 6.4). Formation of an oxide film on the worn surface was accompanied by limited material transfer to the contact surface of the Al_2O_3 ball (Figure 6.5). The increase of testing temperature from 500 °C to 700 °C imposed a smaller wear scar on the Al_2O_3 ball.

Raman spectra of the oxide films covered worn surfaces are shown in Figure 6.6. In the present study Raman signals were assigned by considering the data obtained from the literature [154-165]. The observed prominent signal of the Stellite 12 coating worn at 500 and 700 °C corresponded to CoO and mainly a mixture of Co_3O_4 and Cr_2O_3, respectively. Testing temperature of 500 °C favored CoO formation at the contact surface of the Stellite 12 coating as the result of the reaction of oxygen with the Co-rich matrix. Increasing the testing temperature to 700 °C led to incorporation of chromium as Cr_2O_3 while CoO was transformed to Co_3O_4. Since cobalt oxide grow much more rapidly than chromium oxide, a significant amount of CoO layer can form on the surface of Stellite 12 coating at 500 °C [166]. Increasing oxidation temperature or chromium contents in cobalt-based alloys accelerate the formation of Cr_2O_3 [154, 166]. Therefore the development and presence of Cr_2O_3 in the oxide film at 700 °C reduced the wear loss of the Stellite 12 coating due to its good tribological characteristics and high adhesion, strength, resistance to fracture and fragmentation properties [154, 166, 167].

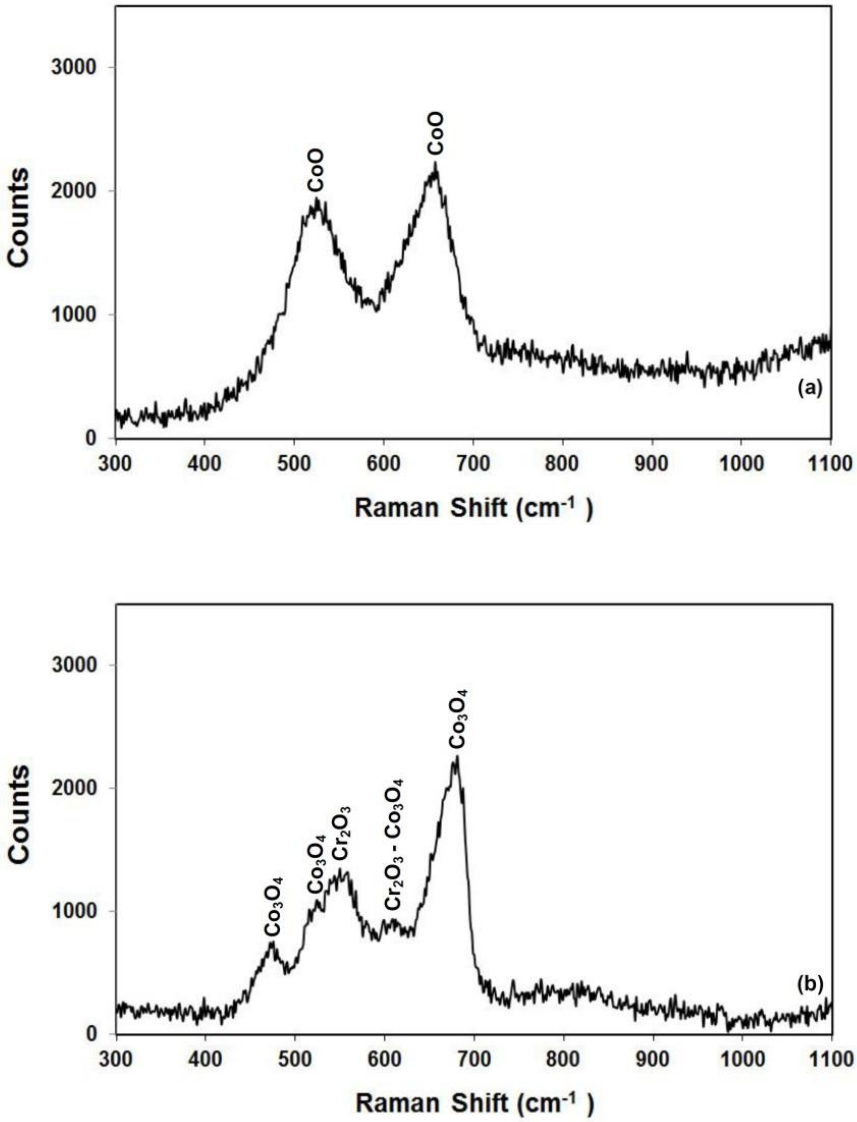

Figure 6.6 : Raman spectroscopy of worn surfaces of Stellite 12 coating after testing at a) 500 and b) 700 °C.

6.2 Alloyed Stellite 12 Coatings

6.2.1 Microstructural characterization

6.2.1.1 Stellite 12+Mo

Cross-sectional microstructure of PTA deposited Stellite 12 coatings containing 2, 6 and 10 wt% Mo are shown in Figure 6.7.

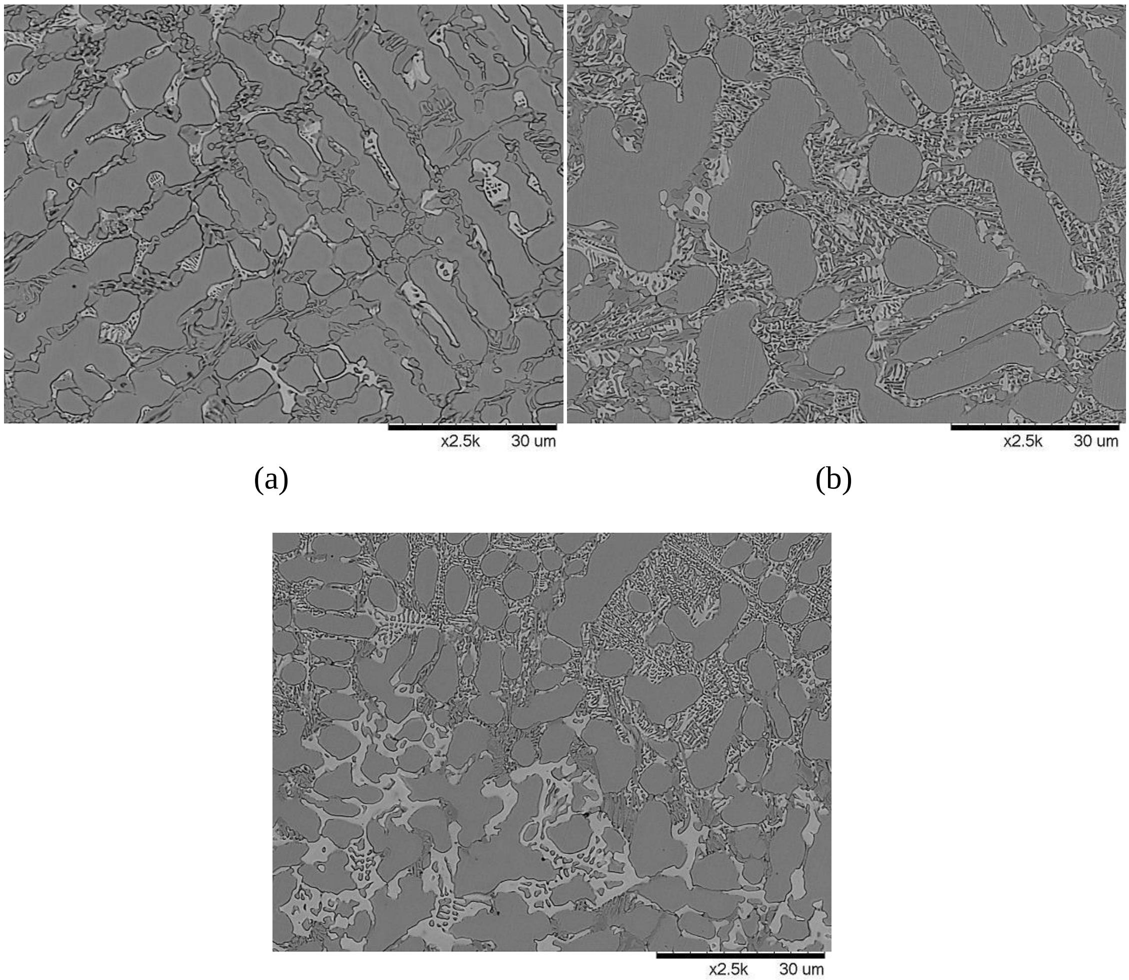

(a) (b) (c)

Figure 6.7 : Cross-sectional SEM micrograph of Stellite 12 coating containing a) 2, b) 6 and c) 10 wt% Mo.

When Mo was added into the Stellite 12, several significantly different solidification characteristics were found in the microstructure evolution of the examined coatings. The SEM micrograph shows that volume fraction of white colored phases increased by increasing Mo content. Elemental X-ray mapping and the results of EDX analyses of the microstructural constituents of Stellite 12+10 wt% Mo along with their average volume fractions are presented in Figure 6.8 and Table 6.3, respectively.

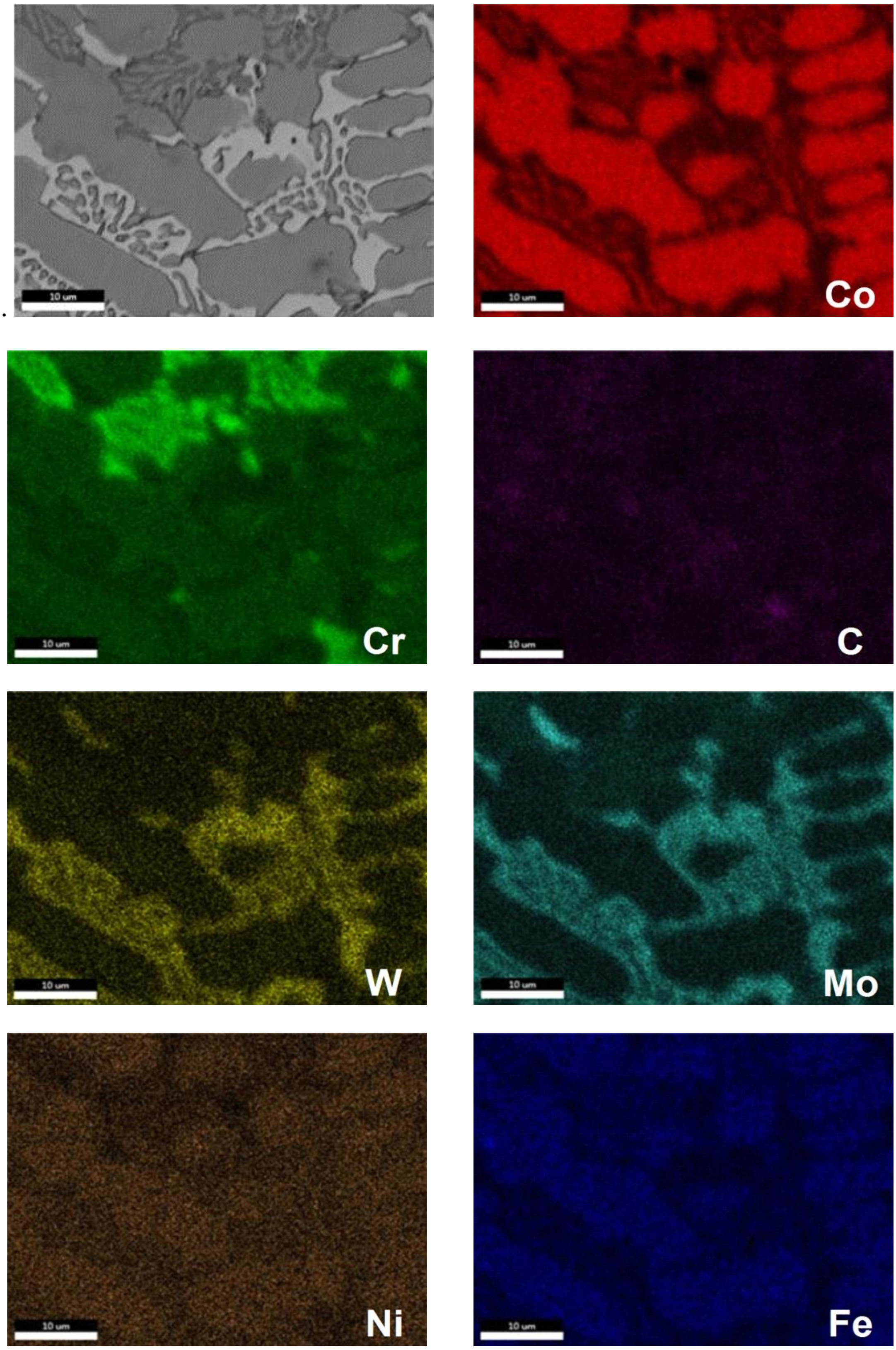

Figure 6.8 : Elemental X-ray mapping of Stellite 12+10 wt% Mo coating.

Table 6.3 : Composition and volume fraction of the constituents present in the microstructures of Stellite 12+10 wt% Mo coating.

Coating	Microstructural constituents	Vol %	Co (at%)	Cr (at%)	W (at%)	Mo (at%)	Ni (at%)	Fe (at%)
Stellite 12 + 10 wt% Mo	Dendritic Matrix	52.4	62.74	26.11	1.73	2.44	2.08	4.90
	Dark grey colored compounds	18.2	17.33	77.96	1.22	3.49	---	---
	White colored compounds	29.4	40.01	34.07	9.22	16.70	---	---

The results show that introducing 10 wt% Mo into Stellite 12 increased the volume fraction of the white colored compounds in the microstructure from 5.6 % to 29.4 %, while reducing the volume fraction of the dark gray compounds and the matrix from 35.6 % to 18.2 % and 58.8 % to 52.4 %, respectively (Table 6.1 and Table 6.3). Also EDX analysis (Table 6.3) revealed that limited amount of molybdenum was dissolved in the dendritic matrix and dark gray compounds (about 3 at%) and white compounds were remarkably enriched by molybdenum (about 17 at%).

Figure 6.9 shows the XRD pattern taken from the examined coatings and investigate how the type of carbides and intermetallic phases changes by addition of Mo element. Peaks of complex carbide (Co_6Mo_6C) and intermetallic (Co_3Mo) detected on the XRD pattern of Mo containing Stellite 12 coating, in addition to the peaks of α-Co (FCC) and Cr-rich carbide ($Cr_{23}C_6$) can be associated with the white compounds in the microstructure (Figure 6.7).

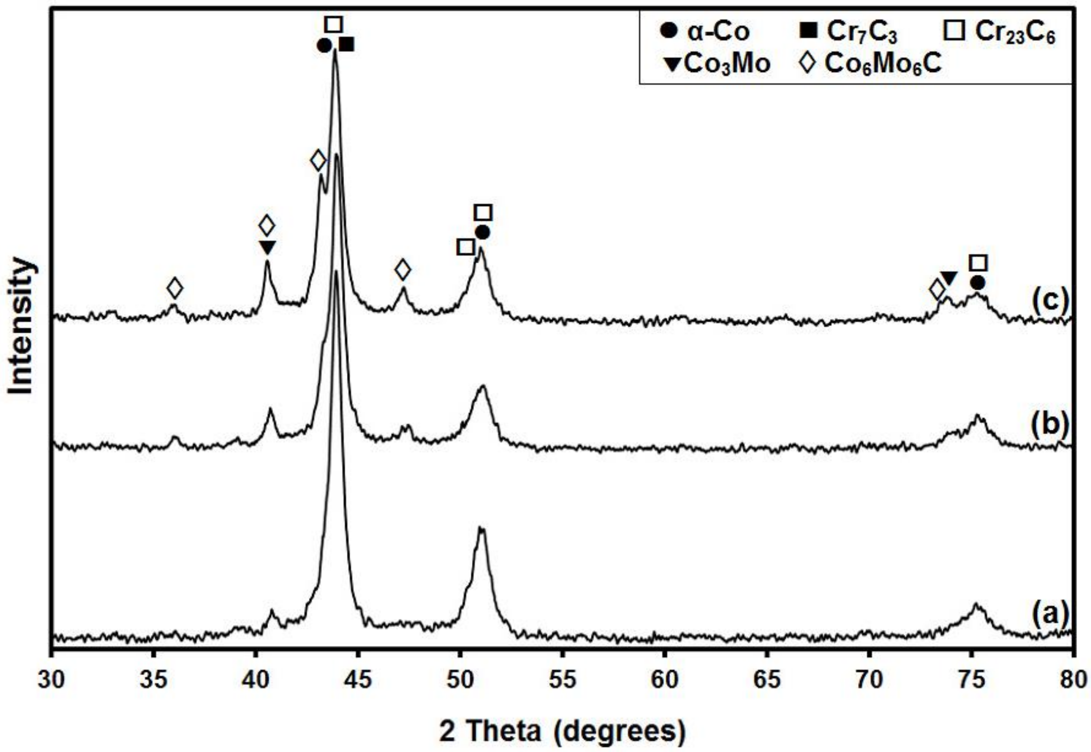

Figure 6.9 : XRD pattern of Stellite12 coating with a) 2, b) 6 and c) 10 wt% Mo.

The microstructural characterization revealed that cooling of the PTA deposited Stellite12 coating containing 2 and 6 wt% molybdenum from liquid state involves primary Co-rich solid solution dendritic matrix and the remaining liquid eventually solidifies by a eutectic reaction into a lamellar mixture of Co-rich solid solution phase with Cr-rich carbides ($Cr_{23}C_6$), Co/Mo-rich complex carbides and intermetallics. It is noticeable that microstructure of 10 wt% containing molybdenum coatings involved Co/Mo-rich complex carbide and/or intermetallic compounds at the interface of dendrites in addition to Co-rich solid solution phase and eutectic compounds. Microstructural survey showed that in Stellite 12+10 wt% Mo deposited coating, after solidification of primary Co-rich dendrite, Co/Mo-rich complex carbide and/or intermetallic compounds develop at the interface of dendrites and finally remaining liquid solidifies by a eutectic reaction. It should be noted that Ni and Fe atoms dissolved completely into the Co-rich matrix phase. Development and increasing amount of Co_6Mo_6C complex carbide and Co_3Mo intermetallic compounds with increasing Mo content in the microstructure of molybdenum containing Stellite 12 can be attributed to the lighter atomic weight and smaller atomic size of molybdenum than those of tungsten, which favor higher mobility during solidification along with greater affinity to carbon [48, 62]. As the complex carbides form, carbon in the molten pool is consumed and therefore relatively low carbon concentration in the remaining melt encourages development of $Cr_{23}C_6$ rather than Cr_7C_3 in the microstructure [7]. Therefore addition of molybdenum up to 10 wt% into Stellite 12 coating reduced the volume fraction of the Co-rich dendritic matrix slightly and encouraged eutectic reaction to form Co/Mo-rich complex carbide (Co_6Mo_6C) and intermetallic (Co_3Mo) while formation of Cr_7C_3 was suppressed.

6.2.1.2 Stellite 12+Ni

Figure 6.10 shows the cross-sectional microstructure of the PTA deposited Stellite 12 coating containing 2, 6 and 10 wt% Ni. It can be seen that microstructure of nickel containing deposited coatings have a hypo-eutectic microstructure characterized by light gray dendrite and dark gray and white colored compounds. Comparing Figure 6.1 and Figure 6.10 revealed that there is no obvious difference between microstructure of Stellite12 and nickel containing Stellite 12 coatings.

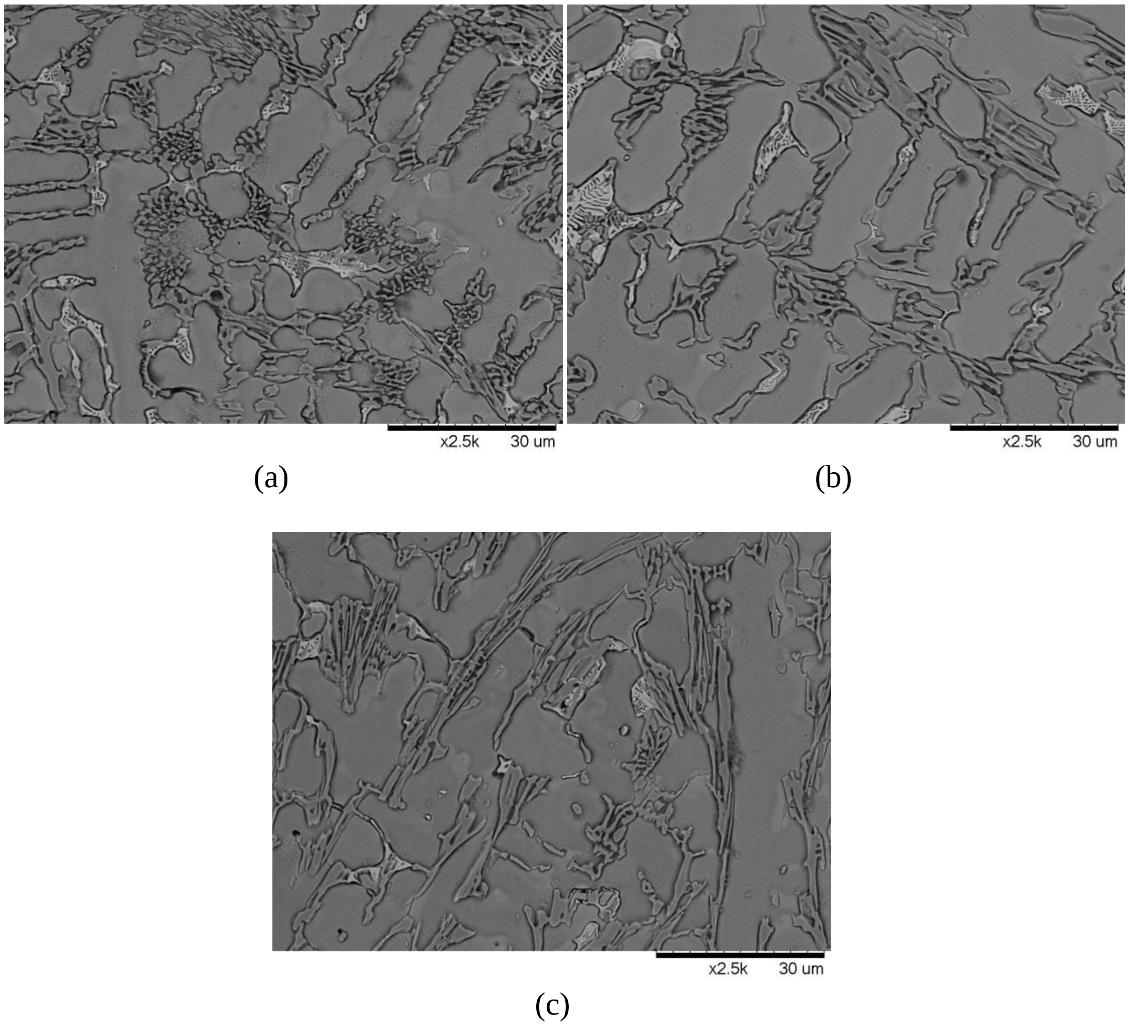

Figure 6.10 : Cross-sectional SEM micrograph of Stellite 12 coating containing a) 2, b) 6 and c) 10 wt% Ni.

Elemental X-ray mapping and the results of EDX analyses of the microstructural constituents of Stellite 12+10 wt% Ni presented in Figure 6.11 and Table 6.4, respectively, indicates that nickel element totally dissolved in Co-rich dendrite matrix without participating in eutectic reaction to form carbides or intermetallics compounds. The average volume fractions of constituents presented in Table 6.1 and Table 6.4 indicates that introducing 10 wt% Ni into Stellite 12 increased the volume fraction of the dendritic matrix from 58.8% to 63.3% while reducing the volume fraction of the dark gray carbides and white colored compounds from 35.6 % to 32.2 % and 5.6 % to 4.4 %, respectively.

Figure 6.12 shows XRD pattern of nickel containing Stellite 12 alloy with varying nickel contents and indicates that microstructure of all deposited nickel containing Stellite 12 coating consisted of α-Co (FCC) and Cr_7C_3 and $Cr_{23}C_6$.

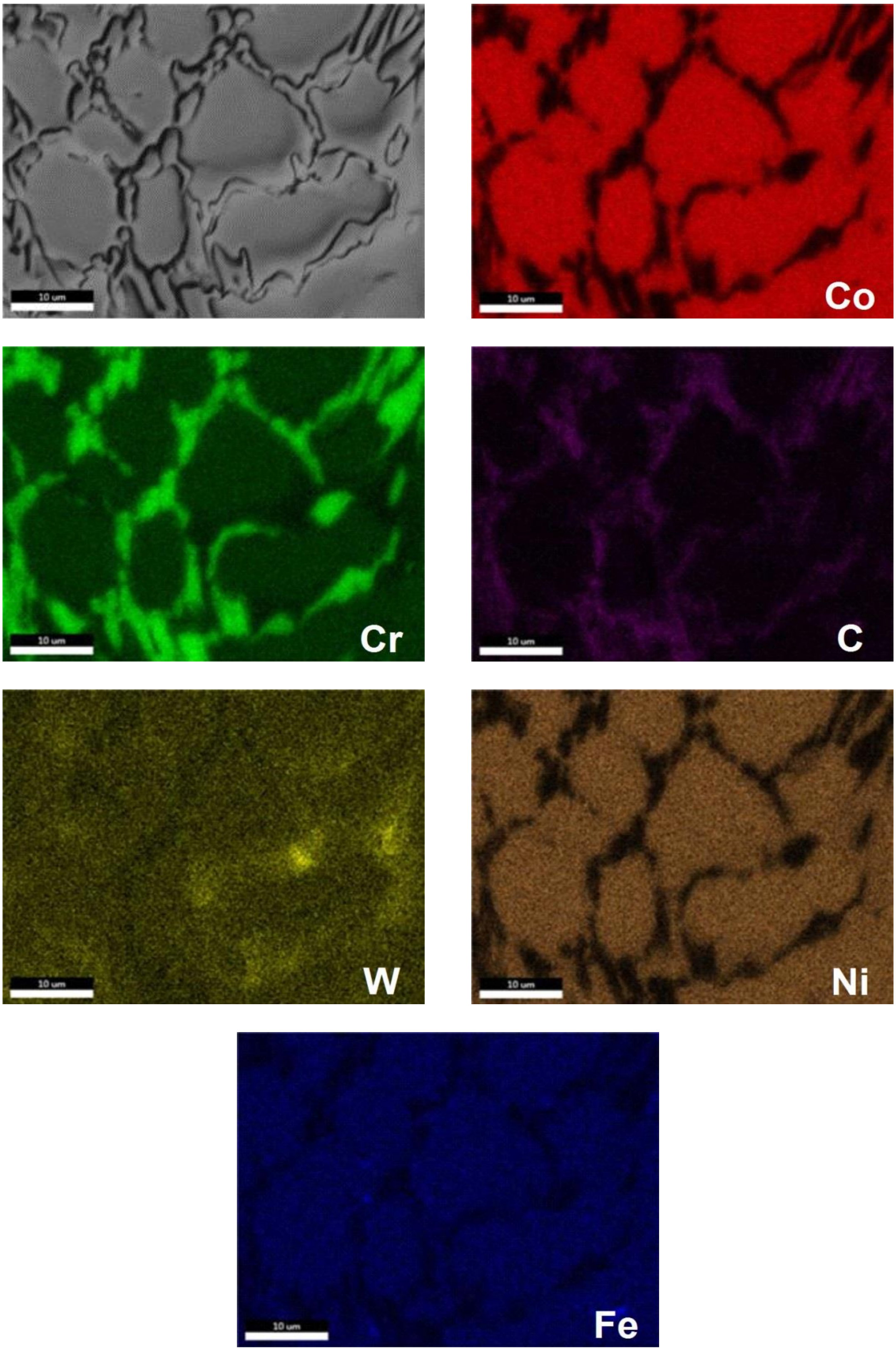

Figure 6.11 : Elemental X-ray mapping of Stellite 12+10 wt% Ni coating.

Table 6.4 : Composition and volume fraction of the constituents present in the microstructures of Stellite 12+10 wt% Ni coating.

Coating	Microstructural constituents	Vol %	Co (at%)	Cr (at%)	W (at%)	Ni (at%)	Fe (at%)
Stellite 12 + 10 wt% Ni	Dendritic Matrix	63.3	57.30	25.18	2.09	12.18	3.25
	Dark grey colored compounds	32.3	34.29	61.95	3.76	---	---
	White colored compounds	4.4	37.17	44.64	18.19	---	---

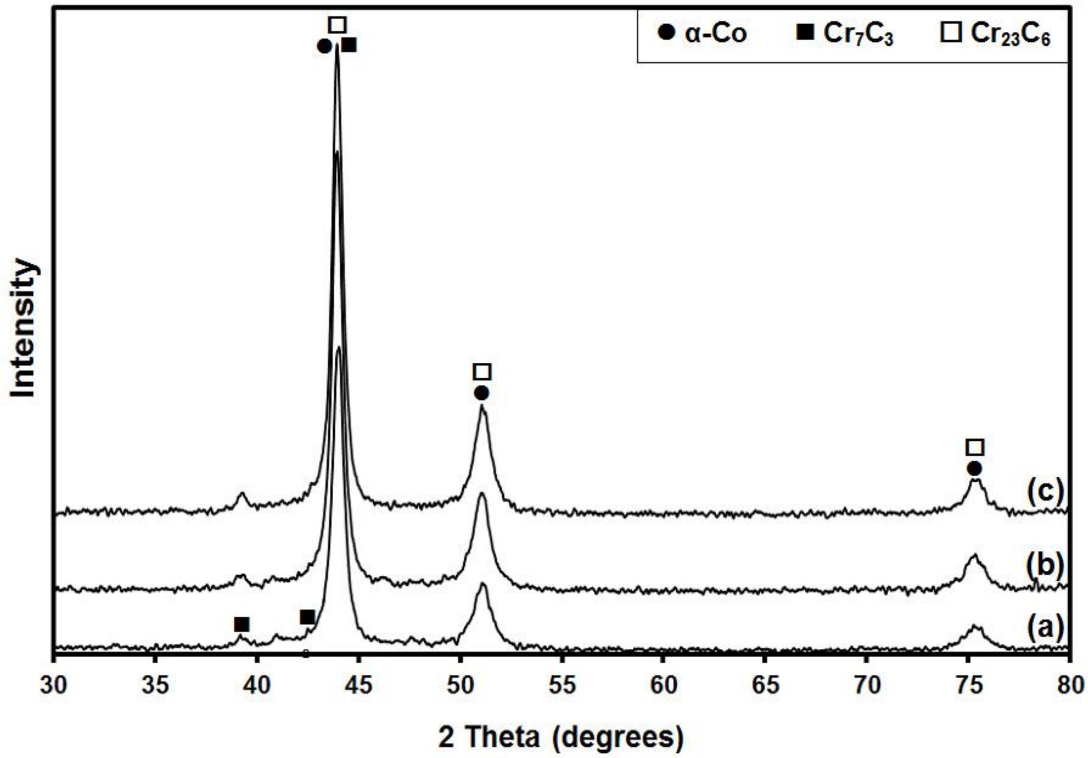

Figure 6.12 : XRD pattern of Stellite12 coating with a) 2, b) 6 and c) 10 wt% Ni.

As mentioned before any peak related to Co/W-rich carbides and/or intermetallics did not appear on the relevant XRD pattern due to their low amount. It is well known that presence and addition of more nickel elements into cobalt-based alloys tends to decrease the FCC to HCP transformation temperature and increasing metastable FCC phases in microstructure at room temperature [64, 119, 144, 168]. Therefore increasing intensity of XRD peaks with addition of nickel elements up to 10 wt% can be attributed to development of more α-Co (FCC) phase instead of ε-Co (HCP) in the microstructure.

6.2.2 Hardness

The hardness values of PTA deposited Stellite 12+Mo and Stellite 12+Ni coatings with varying Mo and Ni contents are presented in Table 6.5. It can be seen from

Table 6.5 that the addition of Mo into Stellite 12 enhanced the hardness of deposited coating and the highest hardness value (621±8 HV_2) can be obtained in the 10 wt% Mo containing coating. It is obvious that the addition of Ni leads to decrease in hardness values of Stellite 12 coating. The hardness value of Stellite 12 coating decreases from 490±10 HV_2 to 458±5 HV_2 as the content of Ni increases up to 10 (wt.%).

Table 6.5 : Vickers mircorhardness values of Stellite 12+Mo and Stellite 12+Ni coatings with varying Mo and Ni contents.

	2 (wt%)	6 (wt%)	10 (wt%)
Stellite 12+ Mo	522±6	568±5	621±8
Stellite 12+ Ni	481±7	472±8	458±5

Any increase in hardness of Mo containing Stellite 12 coatings might be attributed mainly to the following. On the one hand, addition of molybdenum leads to the development of Co/Mo-rich complex carbide and intermetallic compounds in the microstructure. The hardness of Co/W or Co/Mo containing complex carbides and intermetallics and Cr-rich carbides vary between 1420 to 1700 HV and 880 to 1030 HV [48] , respectively. Therefore, replacement of Co_6Mo_6C and Co_3Mo with Cr-rich carbides in the microstructure of the Stellite 12+Mo coating contribute to increasing hardness. On the second hand dissolution of molybdenum in the matrix positively affect the hardness of Mo containing Stellite 12 coatings. Depth sensing hardness measurements presented in Figure 6.13, revealed that the at the constant load of 110 mg plastic penetration depth of indenter decreased from 880 nm to 780 nm which means the matrix hardness of the Stellite 12 coating increased from 470 HV to 513 HV upon the addition of 10 wt% Mo. It is a well-known fact that dissolution of larger atomic sized refractory elements (such as Mo or W) in a Co-rich solid solution obstructs dislocation motion and consequently strengthens the matrix [51, 120, 169].

Decreases in hardness of Stellite 12+Ni coatings can be attributed to changes in crystallographic structure of Co-rich matrix due to addition of Ni. When nickel is dissolved in matrix, the α-Co (FCC) is stabilized, therefore martensitic transformation or work hardening under mechanical load is prevented. In this case deformation occurs by twinning or slip rather than by the FCC→HCP phase transformation and consequently hardness decreases [62, 170, 171].

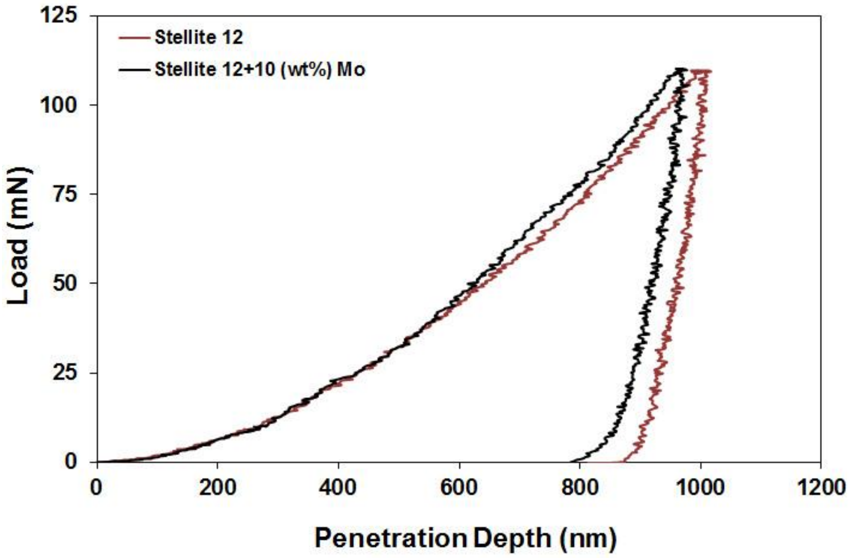

Figure 6.13 : Depth sensing indentation loading and unloading curves of dendritic matrices of Stellite 12 and Stellite 12+10 wt% Mo alloys.

Depth sensing hardness measurements presented in Figure 6.14 obviously show that how penetration depth of indenter increased in Stellite 12+10 wt% Ni coating compared to Stellite 12 under the constant load of 110 mg.

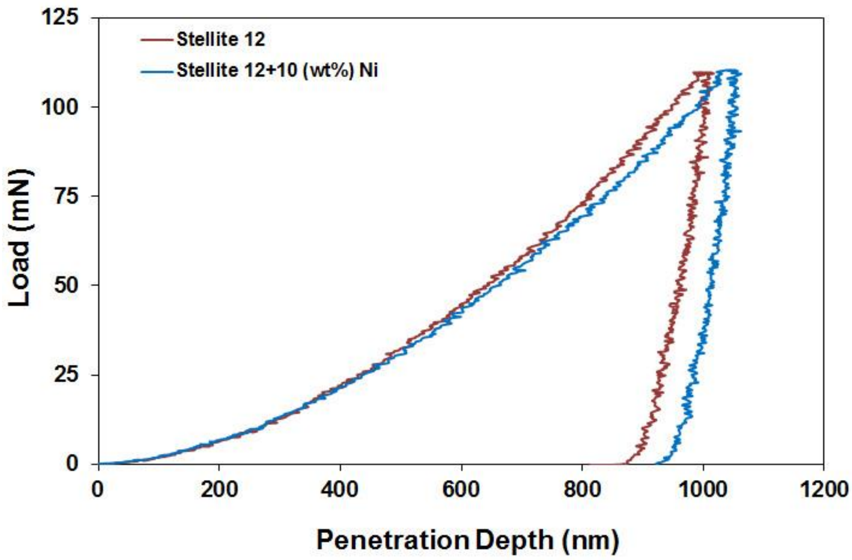

Figure 6.14 : Depth sensing indentation loading and unloading curves of dendritic matrices of Stellite 12 and Stellite 12+10 wt% Ni alloys.

Results indicate that matrix hardness of the Stellite 12 coating decreased from 470 HV to 435 HV upon the addition of 10 wt% Ni. Also lower volume fraction of developed Cr-rich carbides and Co/W-rich intermetallic compound in Ni added coatings led to decrease in hardness (Table 6.1 and Table 6.4).

6.2.3 Wear

The wear loss and friction coefficient of Stellite 12+Mo and Stellite 12+Ni coatings varying with alloying element contents and testing temperature are listed in Table 6.6 and Table 6.7, respectively. The representative 2-D profiles of the wear tracks and related friction coefficient curves recorded during sliding wear of the examined coatings are depicted in Appendix B from Figure B.2 to Figure B.7. It is obvious that in all examined coatings the area of the wear tracks varied remarkably with the testing temperature and testing temperature of 300 and 500 ^{o}C induced bigger wear track areas than those formed at RT and 700 ^{o}C.

Table 6.6 : Wear loss and friction coefficient values of the PTA deposited Stellite 12+Mo coatings at various testing temperatures.

	RT	300 °C	500 °C	700 °C
	Wear Loss (mm^3)×10^{-3}			
Stellite 12+2 wt% Mo	6.02	341.20	158.61	27.04
Stellite 12+6 wt% Mo	5.85	282.15	118.95	11.86
Stellite 12+10 wt% Mo	3.86	255.95	53.31	7.73
Friction Coefficient				
Stellite 12+2 wt% Mo	0.90	0.52	0.61	0.50
Stellite 12+6 wt% Mo	0.90	0.55	0.59	0.45
Stellite 12+10 wt% Mo	0.90	0.56	0.59	0.44

Table 6.7 : Wear loss and friction coefficient values of the PTA deposited Stellite 12+Ni coatings at various testing temperatures.

	RT	300 °C	500 °C	700 °C
	Wear Loss (mm^3)×10^{-3}			
Stellite 12+2 wt% Ni	7.52	410.18	328.54	42.62
Stellite 12+6 wt% Ni	10.26	427.12	325.31	46.85
Stellite 12+10 wt% Ni	15.65	443.85	335.96	52.26
Friction Coefficient				
Stellite 12+2 wt% Ni	0.93	0.52	0.62	0.52
Stellite 12+6 wt% Ni	0.90	0.52	0.60	0.51
Stellite 12+10 wt% Ni	0.90	0.53	0.61	0.53

According to wear tests results presented in Figure B.2, B.3 and B.4 and Table 6.6, it can be seen that the addition of Mo into the Stellite 12 coating reduced the wear track area at all testing temperatures. The results of wear tests presented in Table 6.7 exhibited that at all testing temperature increasing Ni content led to decrease in wear resistance and the highest wear loss was found at 300 and 500 °C. Remarkable decrease in wear resistance of Ni containing Stellite 12 coatings can be observed at

RT sliding wear tests as the wear loss increased by 2 times when the nickel content is increased up to 10 wt%. When the results of the wear tests conducted at 300 °C are of concern, addition of Ni into the Stellite 12 coating slightly increased the wear loss of examined coatings.

Worn surface topographies, EDX patterns taken from the worn surfaces of Stellite 12+Mo and Stellite 12+Ni coatings are illustrated in Figure 6.15 and Figure 6.16, respectively. Also corresponding contact surface appearances of the counter-face (Al_2O_3 ball) are illustrated in Figure 6.17. The wear mechanisms described for Stellite 12 coating at different temperature were dominant in the case of Stellite 12+Mo and Stellite 12+Ni coatings. While the plasticity wear mechanism was progressed at RT and 300 °C, oxidation played a crucial role on wear of examined coatings at 500 and 700 °C. Limited materials transferring to the contact surface of the Al_2O_3 ball and created smaller wear scare on it confirm the positive role of formation of oxide film on reducing wear loss when testing temperature increased from 300 °C to 500 and 700 °C (Fig. 6.17).

When the results of the wear tests conducted at RT and 300 °C are of concern, addition of 10 wt% Mo into the Stellite 12 coating caused about 40% reduction in wear loss under plasticity dominated wear conditions. As the results of the changes in the microstructure, the addition of 2, 6 and 10 wt% Mo improved the hardness of the Stellite 12 coating (Table 6.5) and provided a lower wear loss (Table 6.6). Since hardness and amount of carbides and intermetallic compounds plays a crucial role on the wear performance of Stellite alloys at RT and moderate temperatures [7, 62, 80, 151] a lower wear loss of the Stellite 12+Mo can be attributed to their higher hardness and volume fraction of intermetallic compounds with higher hardness. Reduction of wear resistance of Ni containing coatings at RT can be attributed to stabilization of the α-Co (FCC) and decrease of volume fraction of hard carbides or intermetallic compounds (Table 6.1 and Table 6.4) in the microstructure due to addition of Ni [62, 170, 171]. It is obvious that effect of work hardening on enhancement of wear resistance is prevalent in Stellite 12 coatings. At testing temperature of 300 °C while the work hardening was ineffectiveness, reduction of hardness due to addition of Ni led to only 8% increase in wear loss upon addition of 10 wt% Ni.

Worn surface	EDX pattern

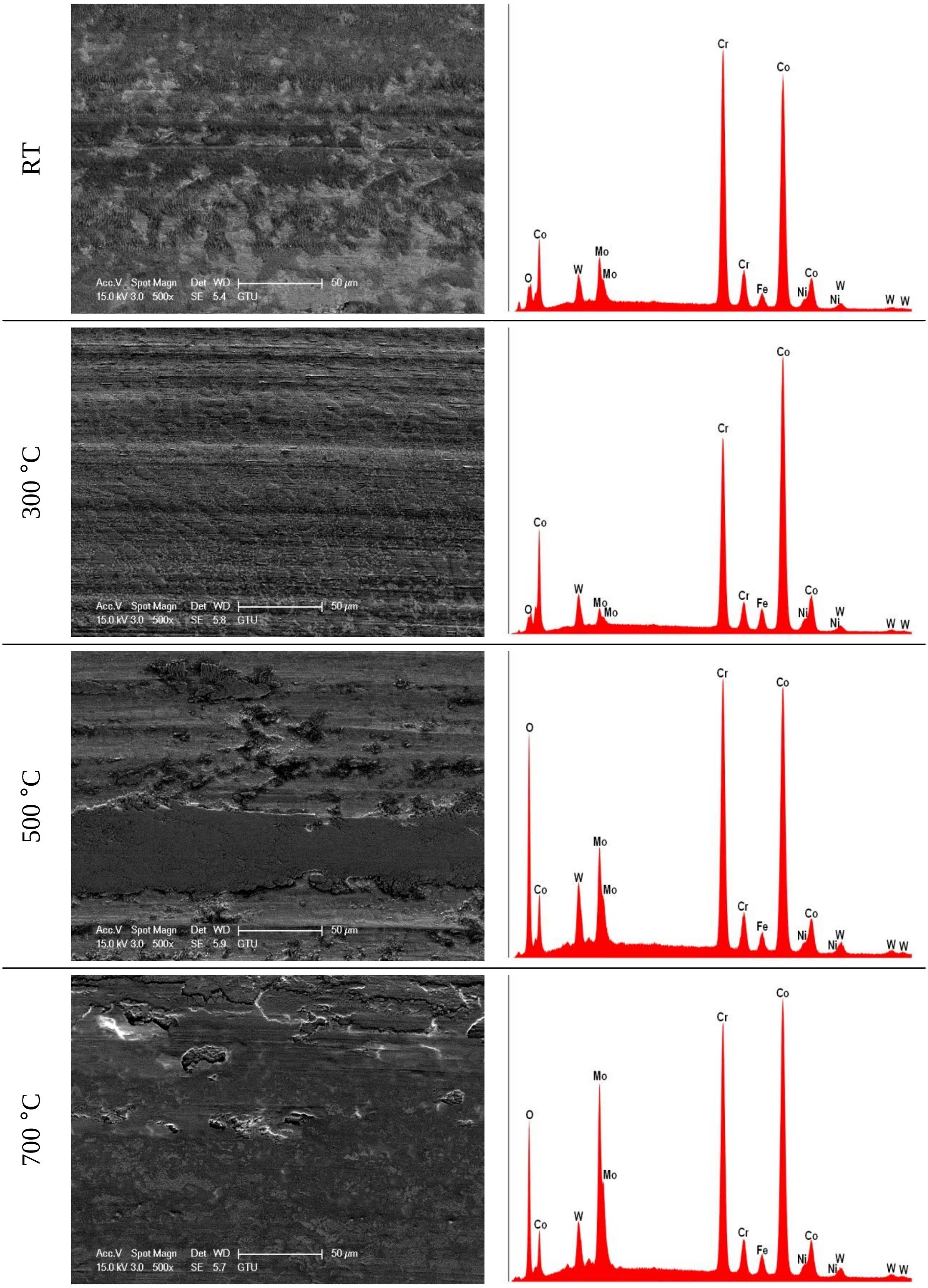

Figure 6.15 : The worn surface topographies and related EDX patterns of Stellite 12+10 wt% Mo coating after wear test.

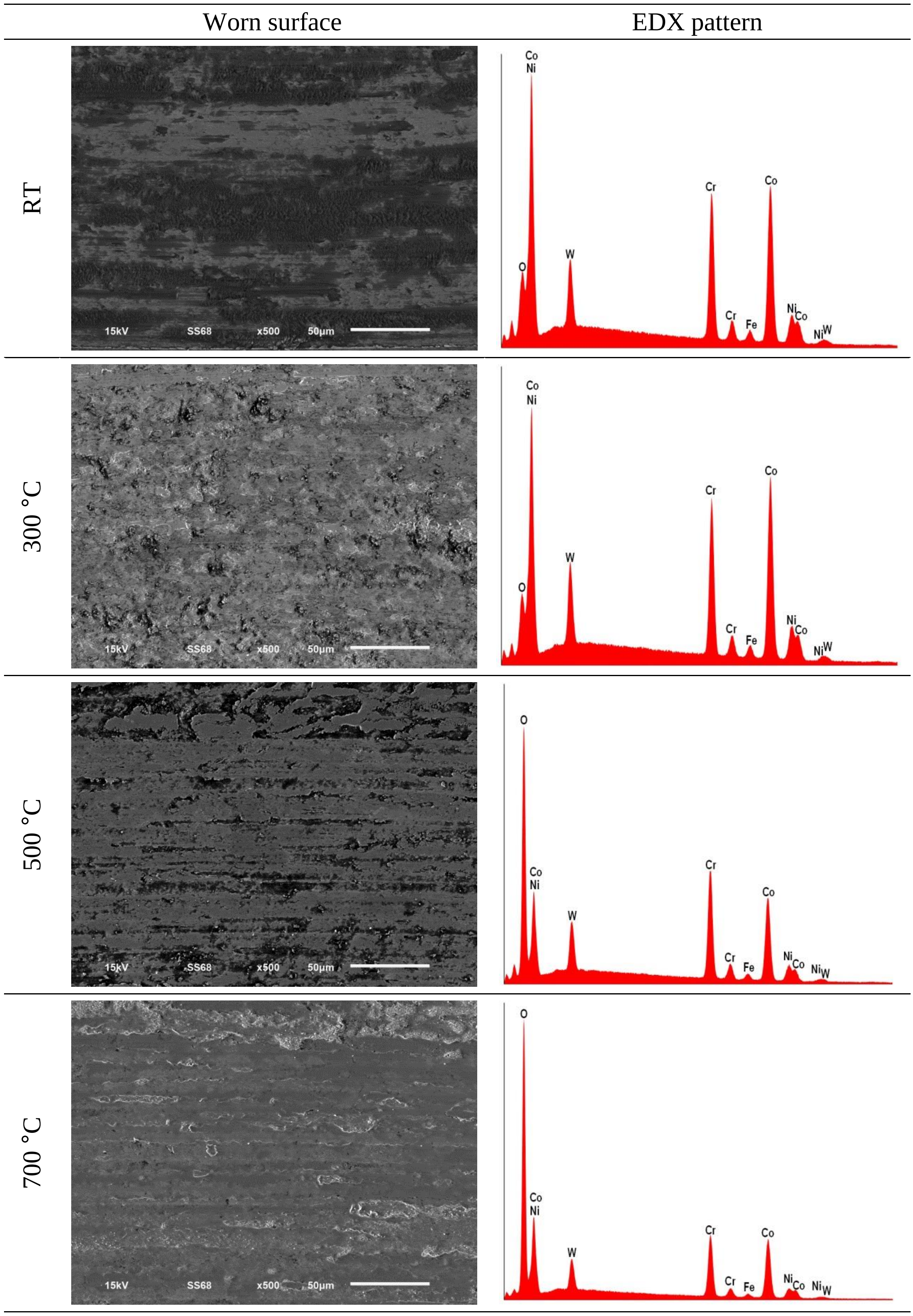

Figure 6.16 : The worn surface topographies and related EDX patterns of Stellite 12+10 wt% Ni coating after wear test.

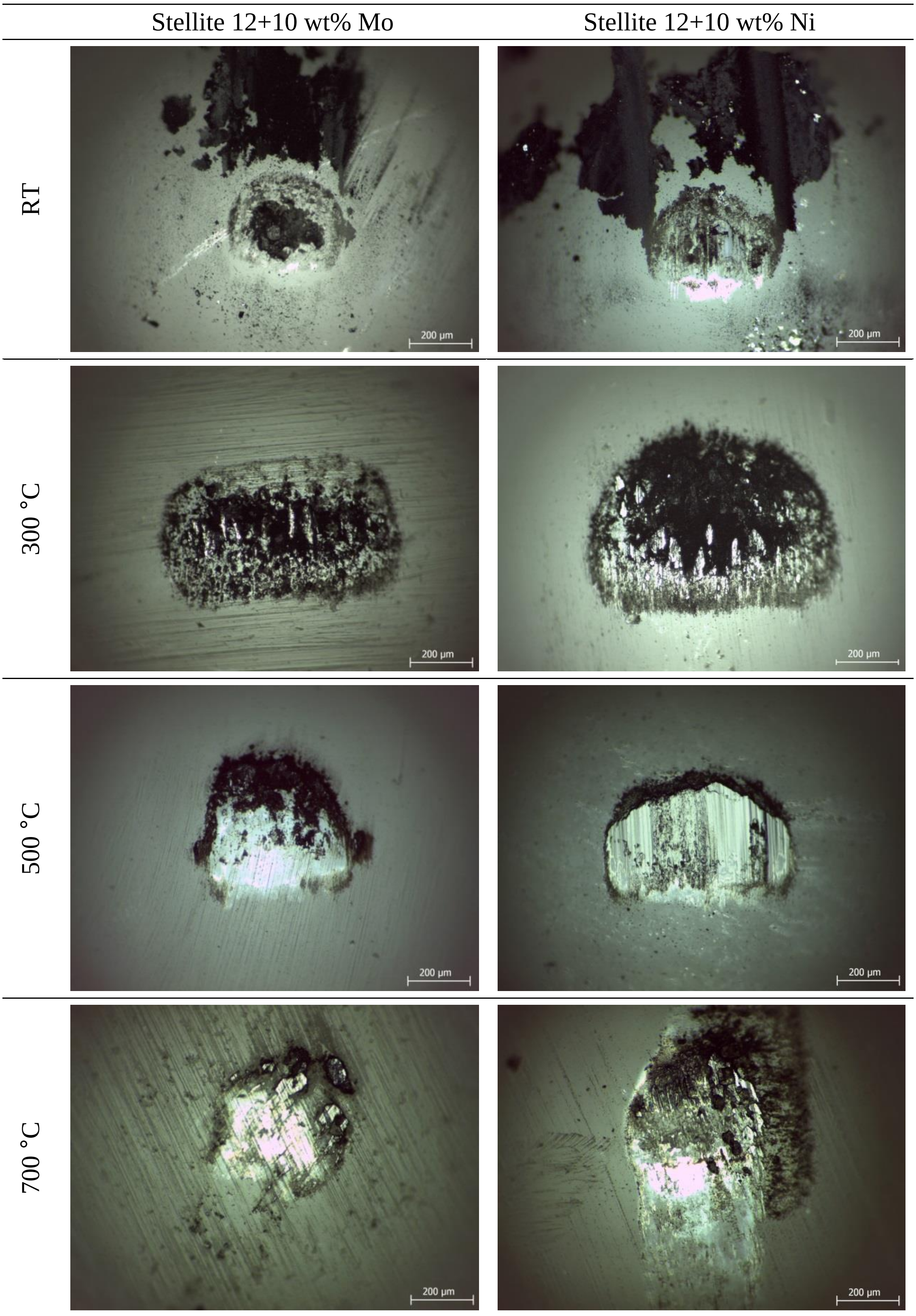

Figure 6.17 : Corresponding contact surface appearances of the Al_2O_3 ball after the wear testing of Stellite 12+10 wt% Mo and Stellite 12+10 wt% Ni coatings.

Under oxidation dominated wear testing conditions at elevated temperature (500 and 700 °C), the Stellite 12+Mo coating exhibited lower wear loss than the Stellite 12 coating in comparison to RT and 300 °C (about 90% lower wear loss). In the case of Stellite 12+Ni coating the results of the wear tests conducted at 500 and 700 °C revealed that addition of Ni into the Stellite 12 coating did not caused remarkable reduction in wear loss. The results of Raman spectroscopy analyses presented in Figure 6.18 and Figure 6.19 clearly indicated that the type of developed oxide film on the worn surfaces at 500 and 700 °C plays crucial role on the wear behavior of the examined coating.

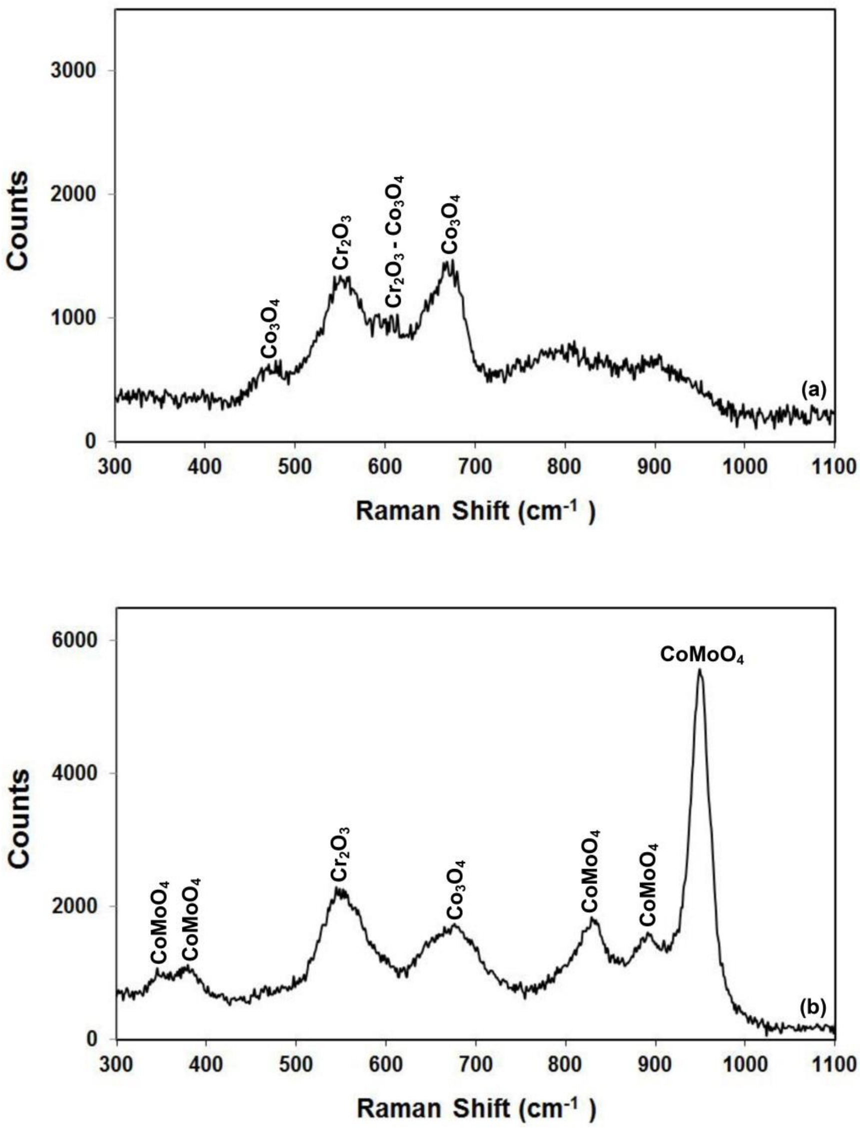

Figure 6.18 : Raman spectroscopy of worn surfaces of Stellite 12+10 wt% Mo coating after testing at a) 500 and b) 700 °C.

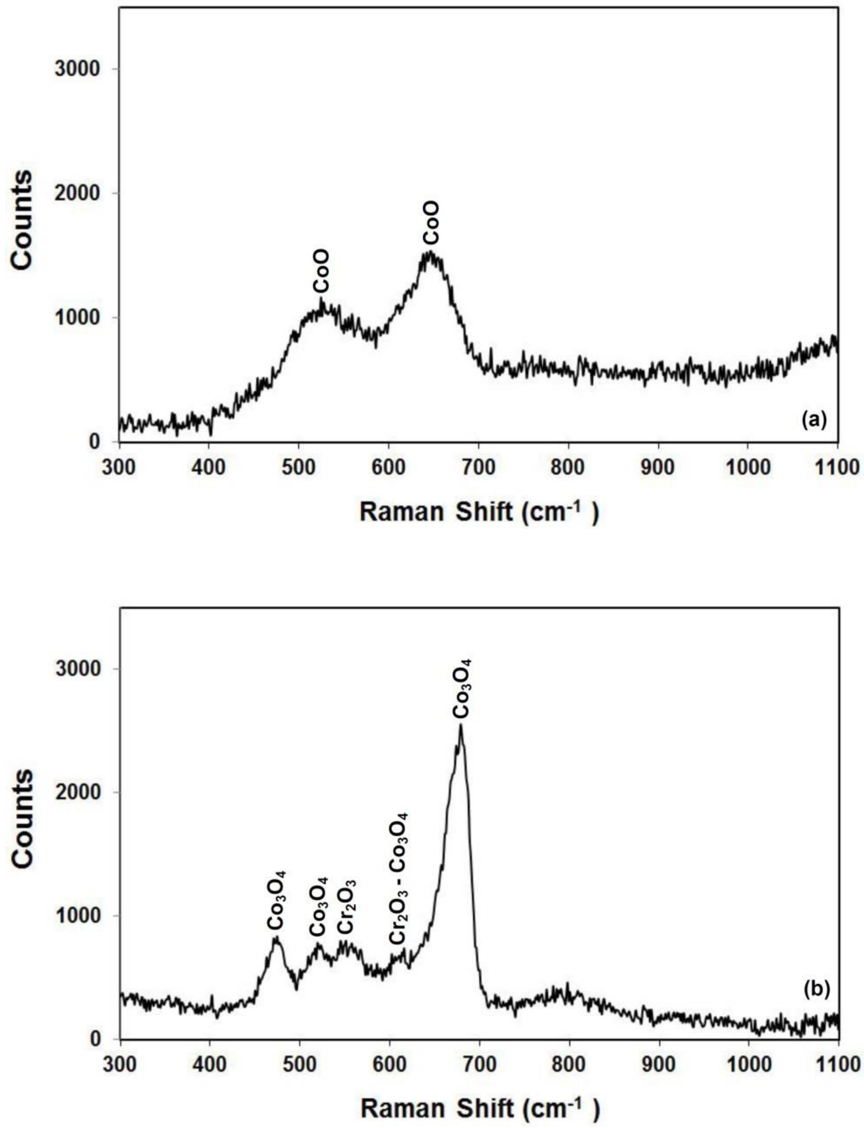

Figure 6.19 : Raman spectroscopy of worn surfaces of Stellite 12+10 wt% Ni coating after testing at a) 500 and b) 700 °C.

In the case of the Stellite 12+10 wt% Mo coating, the oxide film formed at the testing temperature of 500 °C contained similar oxides to that of the Stellite 12 coating worn at 700 °C. Detection of Cr_2O_3 on the worn surface of the Stellite 12+10 wt% Mo coating after testing at 500 °C can be attributed to the presence of $Cr_{23}C_6$ in the microstructure of the coating at the expense of Cr_7C_3 (Figure 6.9). It is reported that increasing temperature leads to enrichment of the matrix with Cr atoms by replacement of cobalt and other atoms dissolved in the matrix with the chromium in the $Cr_{23}C_6$ [172]. Therefore enrichment of the matrix with chromium promoted Cr_2O_3 in the oxide layer. Furthermore, migration of molybdenum atoms dissolved in the matrix to the worn surface of the Stellite 12+Mo coatings during wear testing at 700 °C, accelerated the solid state reaction between the cobalt and molybdenum oxides to form $CoMoO_4$ complex oxide in addition to Cr_2O_3 and Co_3O_4 [173]. In this respect, the remarkable reductions in wear loss and friction coefficient values of the Stellite 12+ 10 wt% Mo coating (from 8.6 to 1.3 and from 0.59 to 0.44, respectively) with increasing testing temperature from 500 °C to 700 °C (Table 6.9 and Table 6.10) can be associated with the existence of $CoMoO_4$ complex oxide within the oxide film of the worn surface. This observation is in good agreement with the tribology literature describing enhanced protective [174] and lubricious [175] nature of the $CoMoO_4$ complex oxide.

Raman spectroscopy analyses presented in Figure 6.19 showed that while the testing temperature of 500 °C favored CoO formation on the worn surface of Stellite 12+10 wt% Ni, increasing testing temperature to 700 °C led to development of Co_3O_4 and Cr_2O_3. According to the literature high mobility and diffusivity of Co atoms toward surface can form CoO film on the worn surface of examined containing coating at 500 °C. By increasing testing temperature to 700 °C, CoO was transformed to Co_3O_4 and also chromium atoms participated in formation of oxide films on the worn surface. It is well-documented that good tribological characteristics of Cr_2O_3 can significantly contribute to the reduction of wear loss of examined coating at 700 °C [154, 166, 167]. Although at elevated testing temperature (500 and 700 °C) increasing Ni contents can favor development of oxide films on the worn surfaces but leads to decreasing hardness of deposited coatings. It has been reported that decreasing hardness and consequently increasing plastic deformation of zone beneath the sliding ball can lead to easily break-down and removal of oxide films formed on worn surfaces and increase the wear damages [117].

6.3 Reinforced Stellite 12 Coatings

6.3.1 Microstructural characterization

6.3.1.1 Stellite 12+WC/W_2C

The microstructural evolution of PTA deposited WC/W_2C reinforced Stellite 12 coatings with varying volume fraction of WC/W_2C particle are shown in Figure 6.20. The SEM micrographs were taken from the zone which reinforcement particles were fully melted and changed the microstructure features. It can be seen that as the volume fraction of WC/W_2C particles increased the size of eutectic compounds decreased and Co-rich dendrite matrix refined. Microstructural surveys indicate that while some part of WC/W_2C particles were completely melted and dissolved in Stellite 12 melt pool, some part of particles were partially melted. Also investigations provided no homogenous distribution of WC/W_2C particles in the examined coatings. It is also reported that WC/W_2C reinforcing particles in the deposited composite coating tend to sink towards the substrate due to their much larger density and higher melting point than that of Co-based alloy [20, 176].

Figure 6.21 and Table 6.8 exhibited elemental X-ray mapping and the results of EDX analyses of the microstructural constituents of Stellite 12+10 vol% WC/W_2C coating along with their average volume fractions.

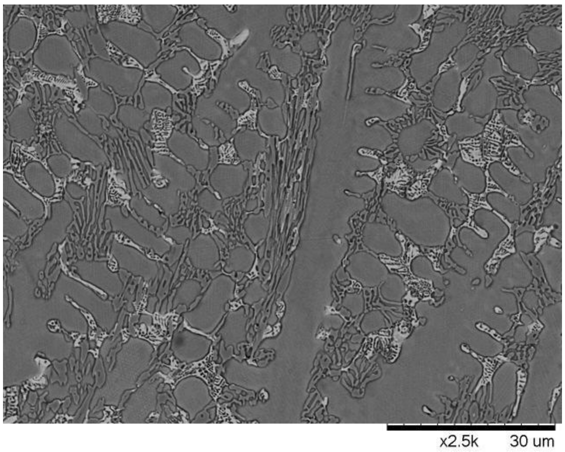

(a)

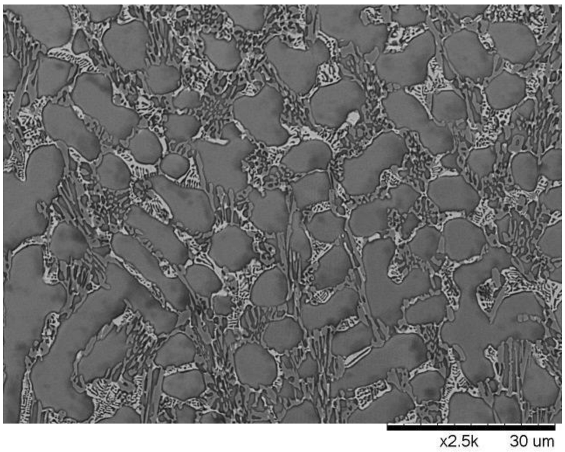

(b)

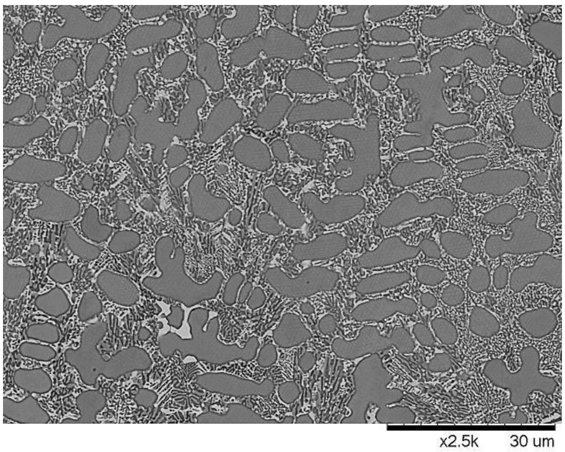

(c)

Figure 6.20 : Microstructural evolution of WC/W_2C reinforced Stellite 12 coatings containing a) 2, b) 6 and c) 10 vol% WC/W_2C.

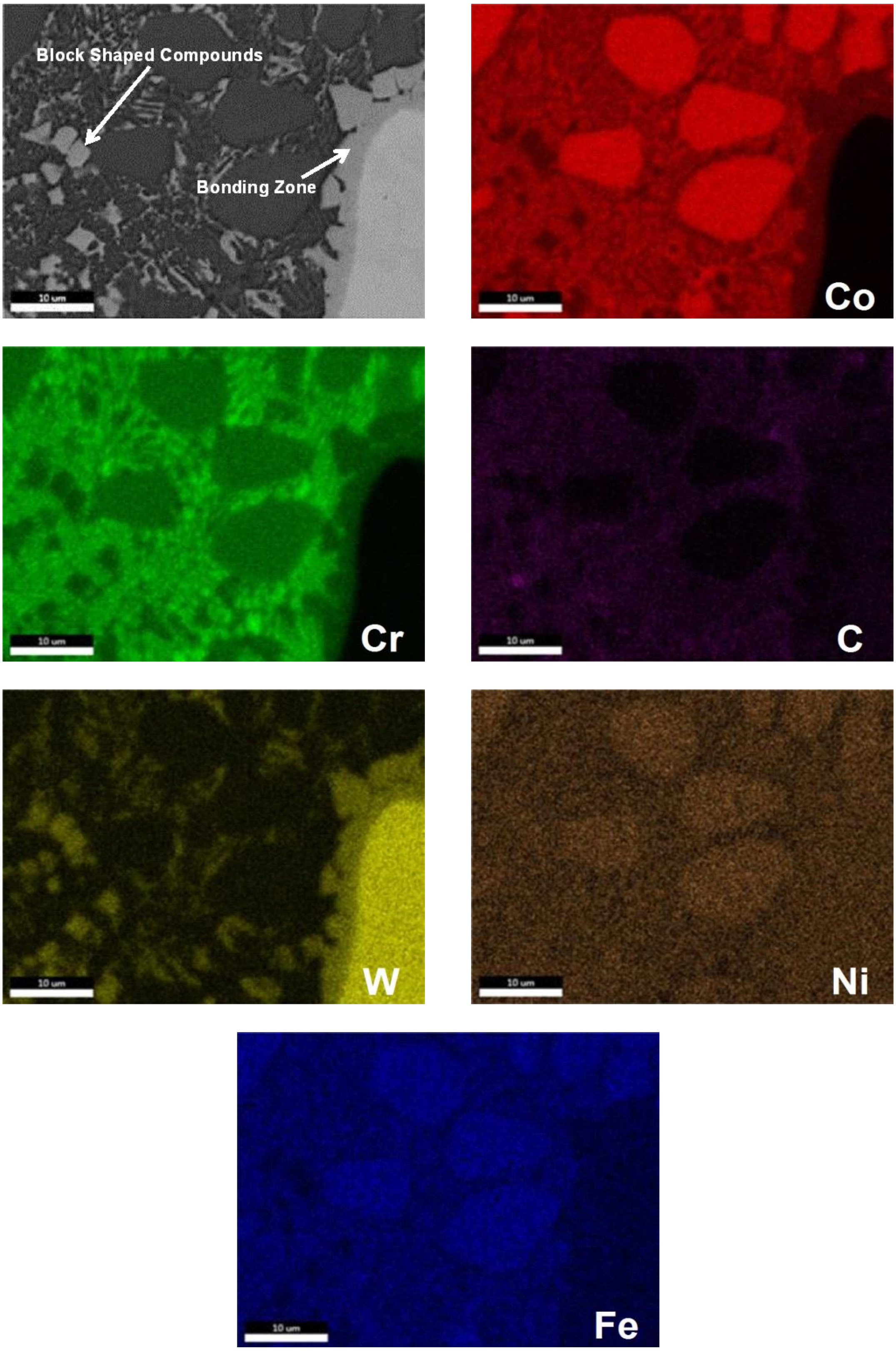

Figure 6.21 : Elemental X-ray mapping of Stellite 12+10 vol% WC/W_2C coating.

Table 6.8 : Composition and volume fraction of the constituents present in the microstructures of Stellite 12+10 vol% WC/W_2C coating.

Coating	Microstructural constituents	Vol. %	Co (at%)	Cr (at%)	W (at%)	Ni (at%)	Fe (at%)
Stellite 12 + 10 vol% WC/W_2C	Dendritic Matrix	49.5	64.57	25.31	3.19	2.28	4.65
	Dark grey colored compound	20.4	20.81	75.34	3.85	---	---
	White colored compound	26.3	51.62	35.27	13.11	---	---
	Block shaped compounds	0.5	55.42	28.12	16.46	---	---
	Bonding Zone	---	42.42	36.46	21.12	---	---
	Unmelted WC/W_2C particles	3.3	---	---	54.12	---	---

Comparing the results of linear intercept method used for quantifying the volume fraction of constituent of Stellite 12 and Stellite 12+10 vol% WC/W_2C coatings (Table 6.1 and Table 6.8) show that while introducing 10 vol% WC/W_2C into Stellite 12 increased the volume fraction of the white colored compounds in the microstructure from 5.6 % to 26.3 %, reduced the volume fraction of the dark gray compounds and the matrix from 35.6 % to 20.4 % and 58.8 % to 49.5 %, respectively. Also EDX analysis revealed that limited amount of tungsten was dissolved in the dendritic matrix (3.85 at%) and no remarkable changes was observed in its content in dark gray and white colored compounds. SEM micrograph of Stellite 12+10 vol% WC/W_2C presented in Figure 6.21 shows that between partially melted reinforcement particles and their surrounded microstructure a bonding zone was formed. This zone is enriched in cobalt, chromium and tungsten. Also block shaped compounds which mainly contained cobalt, chromium and tungsten were observed around WC/W_2C particle.

XRD pattern presented in Figure 6.22 demonstrates the type of carbides and intermetallic phases formed during PTA deposited WC/W_2C reinforced Stellite 12 coatings. Peaks of complex carbide (Co_3W_3C and Co_6W_6C) and intermetallic (Co_3W) detected on the XRD pattern of WC/W_2C containing Stellite 12 coating can be associated with the Co/W-rich white colored compounds in the microstructure and other constituents in the microstructure (Figure 6.20) were identified as α-Co (FCC) and Cr-rich carbides (Cr_7C_3 and $Cr_{23}C_6$).

Microstructural analyses showed that dissolution of WC/W_2C resulted in altering compositions of the dendritic matrix and the volume fraction of compounds formed during solidification. Enrichment of the melt pool in W and C due to dissolution of WC/W_2C particles increased the volume fraction of Co/W-rich complex carbide and intermetallic compounds resulted from eutectic reaction.

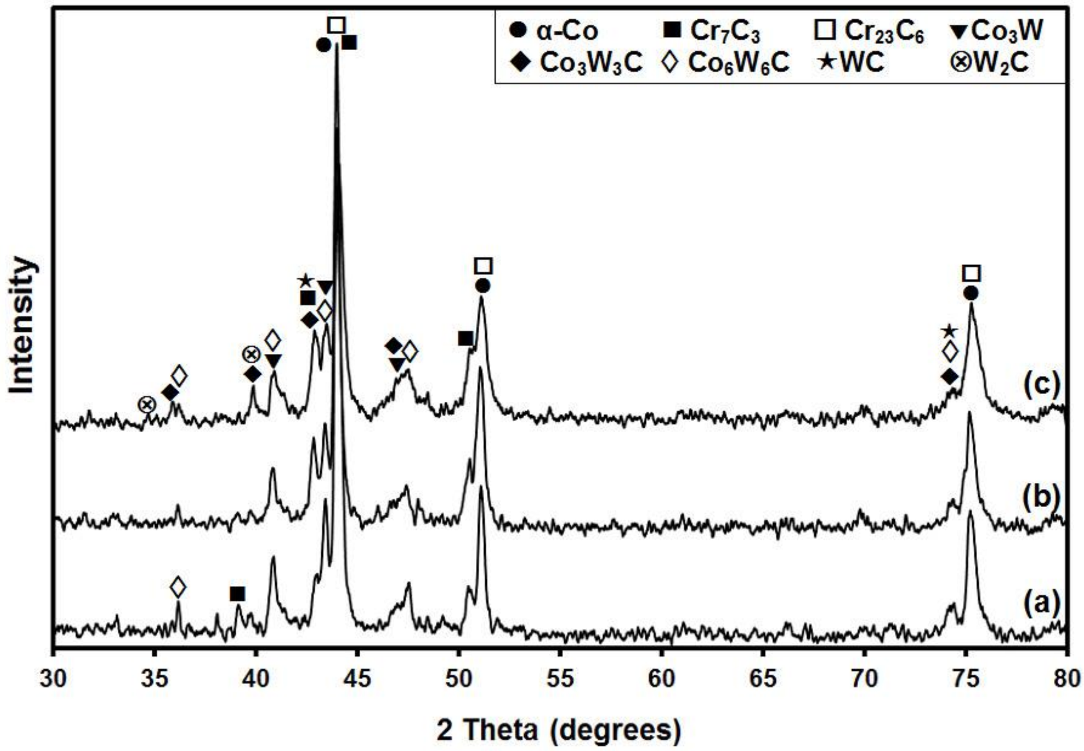

Figure 6.22 : XRD pattern of Stellite12 coating with a) 2, b) 6 and c) 10 vol% WC/W_2C.

It is obvious that when 2 and 6 vol% WC/W_2C was added into the Stellite 12, the basic dendritic matrix and eutectic solidification features of deposited coatings was maintained almost the same but the microstructure characteristic of the examined coatings changed as volume fraction of WC/W_2C particles increased to 10%. Addition of 10 vol% of WC/W_2C particles in to Stellite 12 and consequently increasing dissolution of W and C atoms resulted in formation of Co/W-rich compounds at the interface of dendrites (Figure 6.20 c) and/or block shaped compounds near the reinforcement particles (Figure 6.21). According to the literature, when added WC/W_2C particles in to Stellite alloys are melted during PTA hardfacing, limited part of W element can be dissolved in dendritic matrix and the majority of W will be contained in the eutectic compounds [17, 18, 20, 134]. However, when more W atoms dissolved in the melt, the dendritic matrix will not be able to contain so much of W, therefore the remaining W solidify into a Co/W-rich carbide or intermetallic compounds at the interface of dendrites and/or as block shaped compounds before eutectic reaction. Also presence of partially melted WC/W_2C particles in the melt pool can contribute to refinement of dendritic matrix and developed eutectic compounds due to changes in the nucleation pattern.

6.3.1.2 Stellite 12+TiC

In Figure 6.23 the microstructural SEM micrographs of PTA deposited TiC reinforced Stellite 12 with varying volume fraction of TiC particle is shown. The SEM micrographs show the effect of addition of TiC particles on the evolution of microstructure in the zone which not included reinforcing particles. It is obvious that as the volume fraction of TiC particles increased Co-rich dendrite matrix refined and the volume fraction of dark gray and white colored eutectic compounds increased.

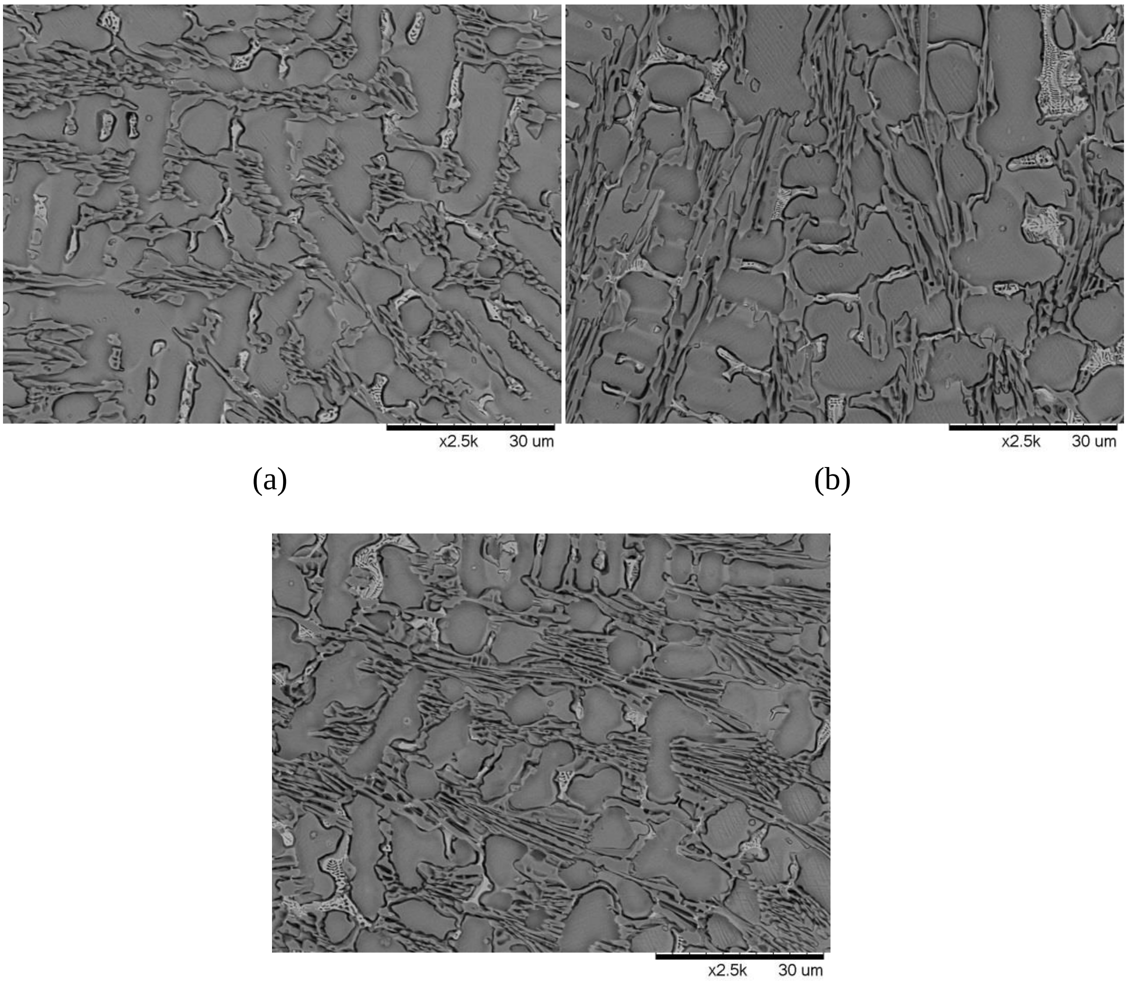

(a) (b)

(c)

Figure 6.23 : Microstructural evolution of TiC reinforced Stellite 12 coatings containing a) 2, b) 6 and c) 10 vol% TiC.

Also investigations provided no homogenous distribution of TiC particles in the microstructure of the PTA deposited examined coatings. Due to density difference between TiC particles (4.94 g/cm^3) and liquid Co-based hardfacing alloys (8.53 g/cm^3), TiC particles tend to float on the surface of melt pool during deposition process [51, 177-179].

Figure 6.24 and Table 6.9 presented elemental X-ray mapping and the results of EDX analyses of the microstructural constituents of Stellite 12+10 vol% TiC coating along with their average volume fractions. Comparing the results of linear intercept method used for quantifying the volume fraction of constituent of Stellite 12 and Stellite 12+10 vol% TiC coatings (Table 6.1 and Table 6.9) show that introducing 10 vol% TiC into Stellite 12 decreased the volume fraction of the matrix from 58.8% to 43.4% while increasing the volume fraction of the dark gray and white colored compounds in the microstructure from 35.6% to 44.20% and 5.6% to 8.1% respectively. Also EDX analysis revealed that very limited amount of titanium was dissolved in the dendritic matrix (0.42 at%), dark gray compounds (0.21 at%) and white colored compounds (0.74 at%).

Presented XRD pattern of TiC reinforced Stellite 12 coatings in Figure 6.25 indicate that the microstructure of examined coating consisted of α-Co (FCC), Cr_7C_3, $Cr_{23}C_6$ and Co_3W compounds. According to the microstructural EDX analyses (Figure 6.24 and Table 6.9) and XRD pattern (Figure 6.25) it can be deduced that while the Co/W-rich white colored compounds in the microstructure can be identified as Co_3W, the Cr-rich dark gray colored compounds and Co-rich light gray matrix can be identified as Cr_7C_3 and $Cr_{23}C_6$ and α-Co (FCC), respectively.

Microstructural surveys show that when 2, 6 and 10 vol% TiC was added into the Stellite 12, the basic dendritic matrix and eutectic solidification features of deposited coatings was maintained almost the same but presence of TiC resulted in altering volume fraction of compounds formed during solidification without changing chemical composition of constituents.

Change of Gibbs free energy of formation governs the thermal stability of the hard particles. The higher negative values of energy, the more stable the particle [32]. As it is shown in Figure 3.1, TiC is more stable than WC, W_2C, SiC, VC and Cr_2C_3 particles at high temperature. Therefore TiC does not dissociate and dissolved easily in to the melt pool during PTA deposition process [32, 130]. Also according to the literature and based on the theoretical kinetic calculations (Table 3.2), the solubility of TiC in cobalt-based hardfacing alloys is least when compared to those of it in nickel- and iron-based hardfacing alloys and compared to other hard particles.

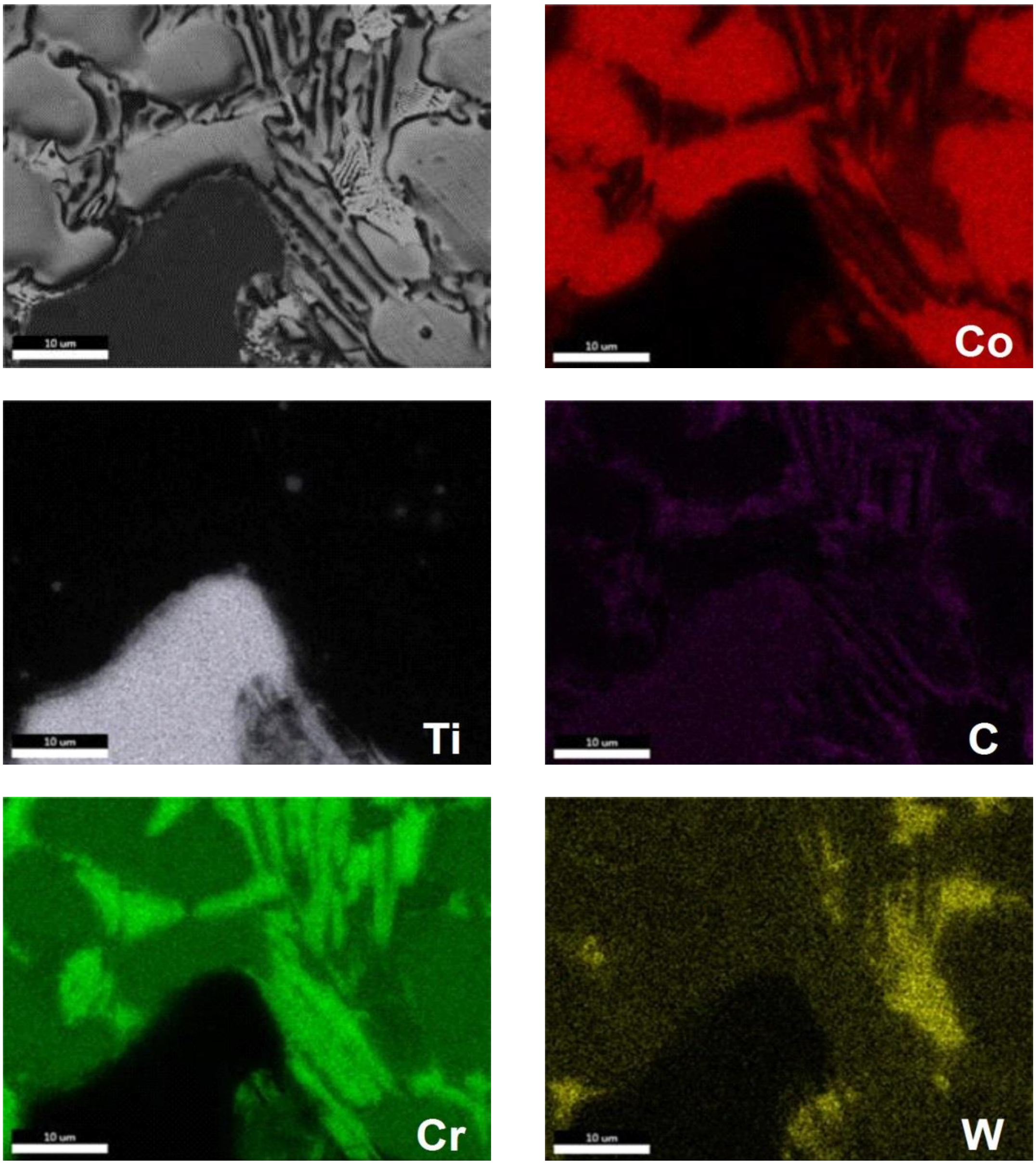

Figure 6.24 : Elemental X-ray mapping of Stellite 12+10 vol% TiC coating.

Table 6.9 : Composition and volume fraction of the constituents present in the microstructures of Stellite 12+10 vol% TiC coating.

Coating	Microstructural constituents	Vol. %	Co (at%)	Cr (at%)	W (at%)	Ni (at%)	Fe (at%)	Ti (at%)
Stellite 12 + 10 vol% TiC	Dendritic Matrix	43.4	65.85	26.15	1.81	2.02	3.75	0.42
	Dark grey colored compound	44.2	21.95	74.75	3.09	---	---	0.21
	White colored compound	8.1	37.10	46.11	16.05	---	---	0.74
	Unmelted TiC particles	4.3	---	---	---	---	---	52.02

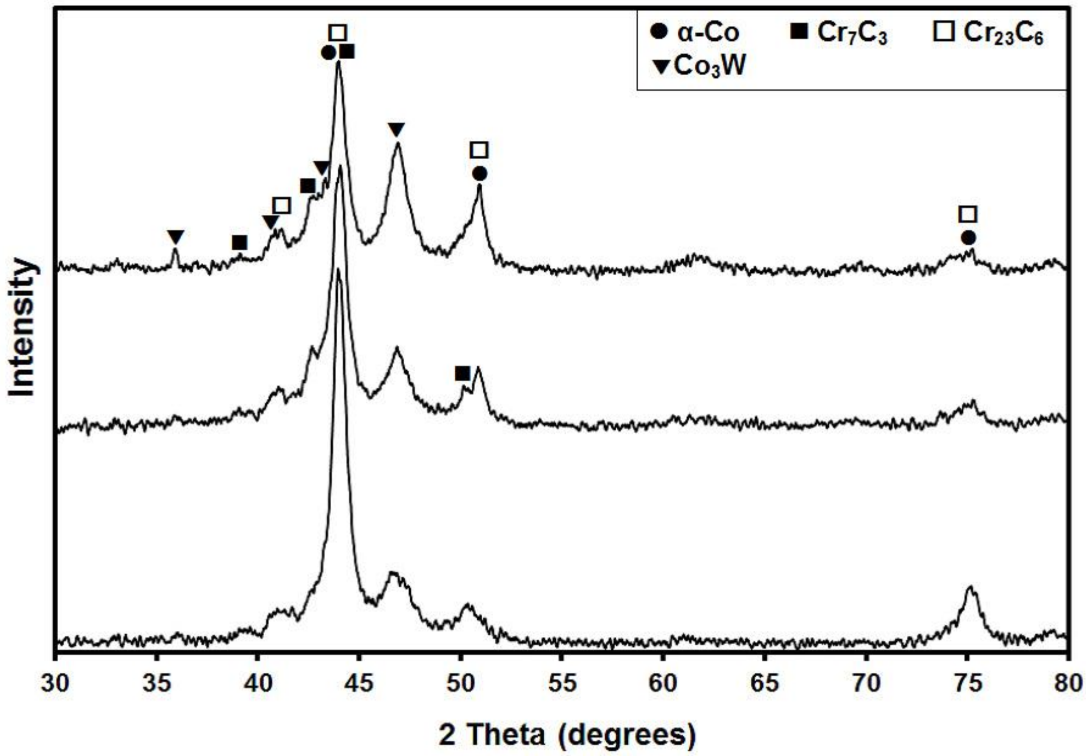

Figure 6.25 : XRD pattern of Stellite12 coating with a) 2, b) 6 and c) 10 vol% TiC.

It is obvious that presences of undissolved TiC particles in the melt pool act as suitable sites for nucleation of eutectic compounds during solidification and consequently contribute to refinement of dendritic matrix and developed eutectic carbides and intermetallics compounds in microstructure [46, 69, 77, 124, 132, 177].

6.3.1.3 Stellite 12+Cr_7C_3

The microstructural evolution of PTA deposited Cr_7C_3 reinforced Stellite 12 coatings with 2, 6 and 10 vol% of Cr_7C_3 particle are shown in Figure 6.26. The SEM micrographs were taken from the zone which reinforcement particles were fully melted and changed the microstructure features. It can be seen that as the volume fraction of Cr_7C_3 particles increased the volume fraction of eutectic compound increased. The microstructure of Stellite 12+10 vol% Cr_7C_3 deposited coating consists of uniformly distributed needle-like eutectic phase. Microstructural investigations indicate that almost total of Cr_7C_3 particles were completely melted and dissolved in Stellite 12 melt pool.

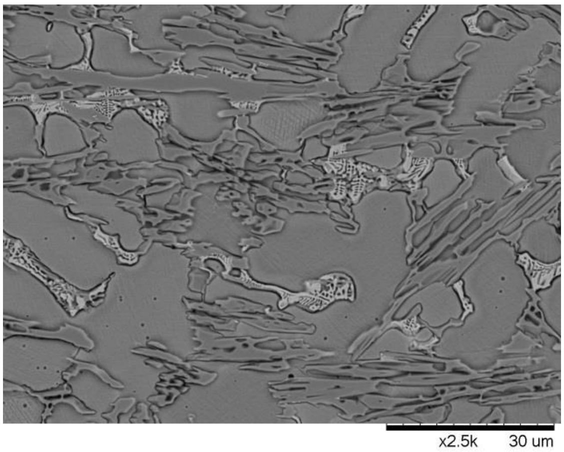

(a)

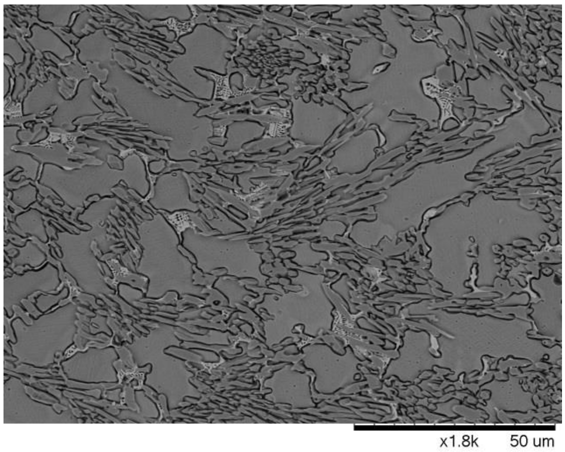

(b)

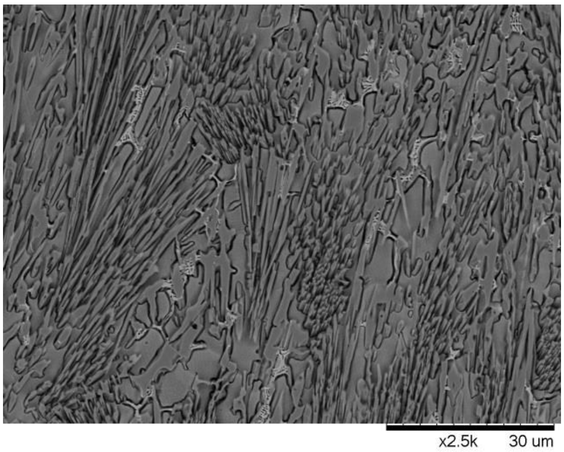

(c)

Figure 6.26 : Microstructural evolution of Cr_7C_3 reinforced Stellite 12 coatings containing a) 2, b) 6 and c) 10 vol% Cr_7C_3.

Elemental X-ray mapping and the results of EDX analyses of the microstructural constituents of Stellite 12+10 vol% Cr_7C_3 coating along with their average volume fractions are presented in Figure 6.27 and Table 6.10, respectively.

Comparing the results of linear intercept method presented in Table 6.1 and Table 6.10 show that addition of 10 vol% Cr_7C_3 into Stellite 12 increased the volume fraction of the dark gray and white colored compounds in the microstructure from 35.6 % to 54.8 % and from 5.6% to 7.6%, respectively. Increasing eutectic compounds with addition of Cr_7C_3 up to 10 vol% resulted in decreasing light gray colored matrix from 58.8% to 35.8%. EDX analyses (Table 6.10) show that while dissolution of Cr_7C_3 increased the chromium atom contents in dark gray compound (from 76.35 at% to 84.46 at%) and white colored compounds (from 40.63 at% to 51.21 at%), no remarkable changes was observed in its content in dendritic matrix.

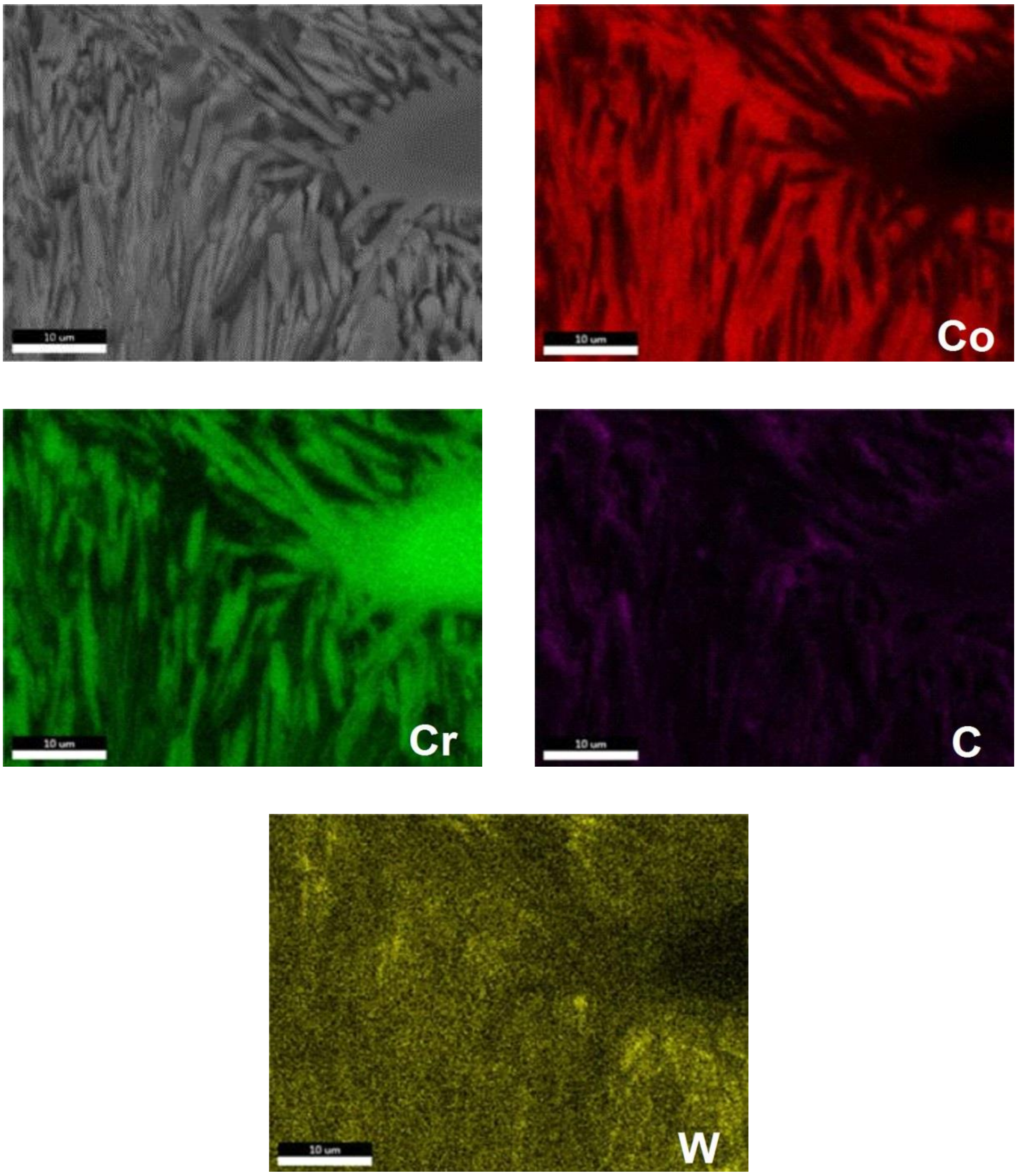

Figure 6.27 : Elemental X-ray mapping of Stellite 12+10 vol% Cr_7C_3 coating.

Table 6.10 : Composition and volume fraction of the constituents present in the microstructures of Stellite 12+10 vol% Cr_7C_3 coating.

Coating	Microstructural constituents	Vol. %	Co (at%)	Cr (at%)	W (at%)	Ni (at%)	Fe (at%)
Stellite 12 + 10 vol% Cr_7C_3	Dendritic Matrix	35.8	62.57	27.96	1.92	2.13	5.42
	Dark grey colored compound	54.8	14.05	84.46	1.49	---	---
	White colored compound	7.6	36.89	51.21	11.90	---	---
	Unmelted Cr_7C_3 particles	1.8	---	68.20	---	---	---

XRD pattern presented in Figure 6.28 demonstrates the type of carbides and intermetallic phases formed during PTA deposited Cr_7C_3 reinforced Stellite 12 coatings.

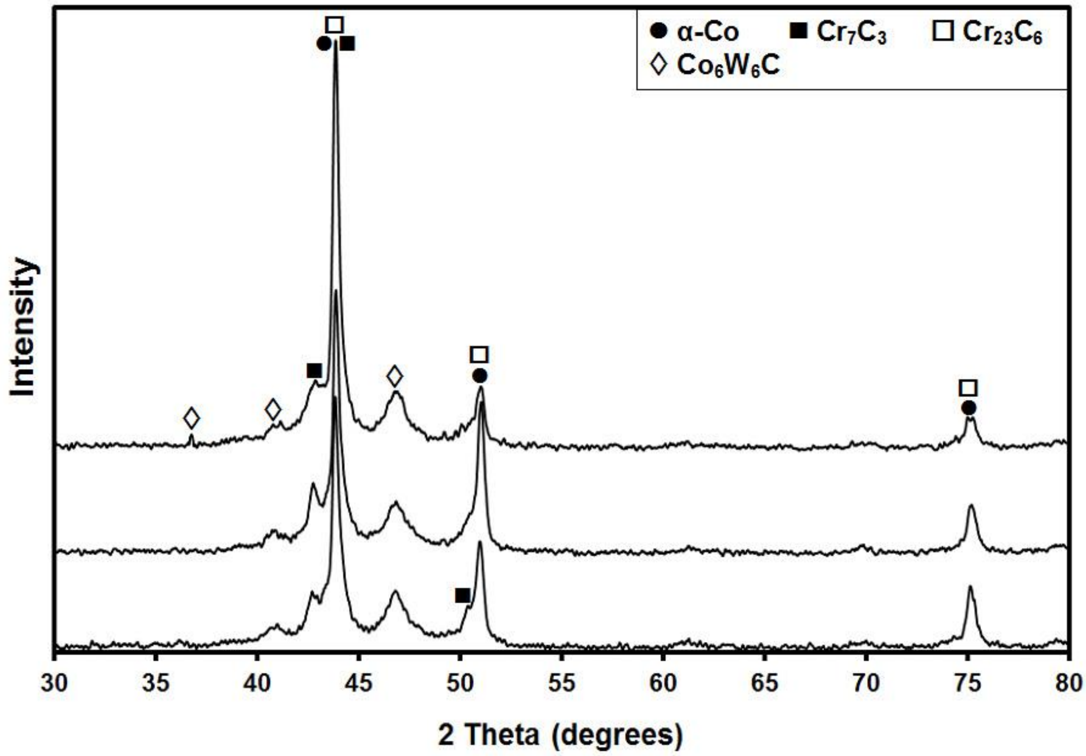

Figure 6.28 : XRD pattern of Stellite12 coating with a) 2, b) 6 and c) 10 vol% Cr_7C_3.

The results show that the microstructure of examined coating consisted of α-Co (FCC), Cr_7C_3, $Cr_{23}C_6$ and Co_6W_6C compounds. It is clear that when 2 and 6 vol% Cr_7C_3 was added into the Stellite 12, the basic dendritic matrix and hypo-eutectic solidification features of deposited coatings was maintained almost the same but the microstructure characteristic of the examined coatings changed as volume fraction of Cr_7C_3 particles increased to 10%. The microstructural characterization revealed that cooling of the PTA deposited Stellite12 coating containing 2 and 6 vol% Cr_7C_3 from liquid state involves primary Co-rich solid solution dendritic matrix and the remaining liquid eventually solidifies by a eutectic reaction into a lamellar mixture of Co-rich solid solution phase with Cr-rich carbides (Cr_7C_3, $Cr_{23}C_6$), Co/W-rich complex carbides (Co_6W_6C). It is noticeable that microstructure of 10 vol% containing Cr_7C_3 coatings involved primary Cr-rich carbide in addition to eutectic phases. Microstructural surveys showed that in Stellite 12+10 vol% Cr_7C_3 deposited coating, after solidification of primary Cr-rich carbides remaining liquid solidifies in to needle-like eutectic phases composed of Cr-rich carbide, Co/W-rich complex carbide and Co-rich solid solution phases. Remarkable increase in volume fraction of Cr-rich carbides resulted during solidification can be attributed to intensive dissolution of Cr_7C_3 hard particles due to its low melting point and high solubility in Co-based hardfacing alloys that increase content of free Cr and C in the melt pool [32, 137, 180]. Also high C content of melt pool induced formation of Co_6W_6C complex carbide in the microstructure.

6.3.2 Hardness

The average hardness of the PTA deposited Stellite 12+ WC/W_2C, Stellite 12+TiC and Stellite 12+Cr_7C_3 coatings with varying reinforcement particle contents are presented in Table 6.11. These measurements were made in the zone which not included particles and therefore only the influence of carbide particles on the hardness of microstructure that is far away particles was determined. It can be seen that in all examined coatings increasing the volume fraction of reinforcing particles leads to increase in hardness and the highest hardness value can be obtained in the 10 vol% particle containing coating. Among the examined coatings, WC/W_2C reinforced Stellite 12 coatings showed the highest hardness values at different contents of particle.

Table 6.11 : Vickers microhardness values of Stellite 12+WC/W_2C, Stellite 12+TiC and Stellite 12+Cr_7C_3 coatings varying with particles contents.

	2 (vol%)	6 (vol%)	10 (vol%)
Stellite 12+ WC/W_2C	538±5	588±7	642±5
Stellite 12+ TiC	521±5	554±5	580±8
Stellite 12+Cr_7C_3	533±7	579±5	636±6

Any increase in Vickers microhardness of Stellite 12+WC/W_2C coatings can be explained in the same manner as described in the Mo containing Stellite 12 coatings. Fully or partially melting of WC/W_2C particles enriched the melt pool in W and C during PTA deposition and leads to development of more Co/W-rich complex carbides and intermetallic in microstructure. Due to this fact that he hardness of refractory element containing complex carbides (Co_3W_3C and Co_6W_6C) and intermetallics (Co_3W and Co_7W_6) are higher than Cr-rich carbides [48, 134], development of more Co/W-rich compound in addition to Cr-rich carbides in the microstructure of the Stellite 12+WC/W_2C coating (Table 6.8) contribute to increasing hardness. Also dissolution of W in Co-rich matrix and increasing its content up to 3.19 at% in Stellite 12+10 wt% WC/W_2C coating can be beneficial to enhancement hardness owing to solid solution hardening effect [51, 120, 169].

Enhancement in hardness of Stellite 12+TiC coatings can be explained by formation of more Cr-rich eutectic carbide during solidification by increasing TiC particle content (Table 6.9). Since hardness of Stellite 12 alloy mainly depend on Cr-rich carbides (with hardness of 880 to 1030 HV) dispersed in a Co-rich solid solution matrix (with hardness of 400 to 480 HV) formation of more Cr-rich carbide due to change in nucleation pattern or chemical composition led to an increase in hardness of microstructure [60, 137, 168].

In the case of Stellite 12+Cr_7C_3 coatings, lower melting point of Cr_7C_3 particle (1775 °C) promoted their dissolution in melting pool. Enrichment of melting pool in Cr and C contributed to development of mainly Cr_7C_3 and $Cr_{23}C_6$ during solidification [107]. It is well documented that chromium carbides (in the form of Cr_3C_2 and Cr_7C_3) have the lowest melting temperature of the used reinforcement for hardfacing applications and usually melts and dissolves partly or fully into the melt pool and precipitate in the form of Cr_7C_3 and $Cr_{23}C_6$ during cooling [133, 180-182]. Since developed Cr-rich carbides in the microstructure of Stellite 12 have hardness twice higher than Co-rich solid solution matrix, formation of more Cr-rich carbide (in the form of Cr_7C_3 or $Cr_{23}C_6$) due to addition of Cr_7C_3 particles (Table 6.10), led to enhancement in hardness of Stellite 12 alloys and reached to its highest value (636±6 HV_2) upon addition of 10 vol% Cr_7C_3 [32, 181].

6.3.3 Wear

The mean values of wear loss and friction coefficient of Stellite 12 coatings containing 2, 6 and 10 vol% WC/W_2C, TiC and Cr_7C_3 reinforcing particles tested at RT, 300, 500 and 700 °C are listed in Table 6.12, Table 6.13 and Table 6.14, respectively. The related 2-D profiles of the wear tracks and friction coefficient curves recorded during wear test are presented in Appendix B (Figure B.8 to Figure B.16). In all examined coatings, testing at 300 and 500 °C resulted in bigger wear track than those formed at RT and 700 °C.

The results presented in Table 6.2 and Table 6.12 indicates that the addition of WC/W_2C into the Stellite 12 coating reduced the wear track area at all testing temperatures and the Stellite 12+10 vol% WC/W_2C coating showed the better wear performance in comparison with 2 and 6 vol% containing WC/W_2C coatings. Also the wear test results showed that the wear resistance of Stellite 12 coating improved about 85% and 60 % at 500 and 700 °C, respectively upon addition of 10 vol% WC/W_2C.

Table 6.12 : Wear loss and friction coefficient values of the PTA deposited Stellite 12+WC/W_2C coatings at various testing temperatures.

	RT	300 °C	500 °C	700 °C
	Wear Loss $(mm^3)\times10^{-3}$			
Stellite12+2vol% WC/W_2C	6.02	199.83	142.62	40.22
Stellite12+6vol% WC/W_2C	5.22	187.10	113.96	33.21
Stellite12+10vol% WC/W_2C	3.68	157.26	51.24	16.80
Friction Coefficient				
Stellite12+2vol% WC/W_2C	0.88	0.61	0.68	0.53
Stellite12+6vol% WC/W_2C	0.88	0.71	0.65	0.54
Stellite12+10vol% WC/W_2C	0.91	0.74	0.63	0.54

Table 6.13 : Wear loss and friction coefficient values of the PTA deposited Stellite 12+TiC coatings at various testing temperatures.

	RT	300 °C	500 °C	700 °C
	Wear Loss $(mm^3)\times10^{-3}$			
Stellite 12+2 vol% TiC	5.52	294.02	175.87	46.22
Stellite 12+6 vol% TiC	4.62	255.96	176.13	58.20
Stellite 12+10 vol% TiC	3.60	228.57	297.02	94.49
Friction Coefficient				
Stellite 12+2 vol% TiC	0.90	0.52	0.62	0.51
Stellite 12+6 vol% TiC	0.88	0.55	0.63	0.52
Stellite 12+10 vol% TiC	0.88	0.58	0.66	0.54

Table 6.14 : Wear loss and friction coefficient values of the PTA deposited Stellite 12+Cr_7C_3 coatings at various testing temperatures.

	RT	300 °C	500 °C	700 °C
	Wear Loss $(mm^3)\times10^{-3}$			
Stellite12+2vol%Cr_7C_3	5.02	253.00	171.18	56.35
Stellite12+6 vol%Cr_7C_3	4.51	215.09	277.19	69.86
Stellite12+10 vol%Cr_7C_3	3.58	202.22	436.03	106.42
Friction Coefficient				
Stellite12+2vol%Cr_7C_3	0.91	0.51	0.61	0.52
Stellite12+6 vol%Cr_7C_3	0.91	0.54	0.63	0.54
Stellite12+10 vol%Cr_7C_3	0.90	0.59	0.69	0.57

In the case of Stellite 12+TiC coating, comparing the wear tests results presented in Table 6.2 and Table 6.13 showed that while the addition of 2, 6 and 10 vol % TiC reduced the wear loss of Stellite 12 coating at RT, 300 and 500 °C, resulted in increasing of wear loss at testing temperature of 700 °C. At RT and 300 °C the wear resistance of Stellite 12 coating improved about 44 % upon addition of 10 vol% TiC particle. At testing temperature of 500 °C, 2 and 6 vol% containing TiC coatings yielded 46% less wear loss in comparison with Stellite12 coating but significant difference was not observed between wear loss of Stellite 12+10 vol % TiC and Stellite 12 coating. Addition of TiC particles into Stellite 12 coating led to decrease in wear resistance of examined coatings at 700 °C as wear loss increase more than two times upon addition of 10 vol % TiC.

Table 6.2 and Table 6.14 indicated that addition of 2, 6 and 10 vol% Cr_7C_3 particles into the Stellite 12 enhanced its wear resistance at RT and moderate temperature as the Stellite 12+10 vol% Cr_7C_3 coating showed 45% and 50% less wear loss at RT and 300 °C, respectively. At 500 and 700 °C, increasing content of Cr_7C_3 particles in examined coating raised the wear loss values. At testing temperature of 500 °C while addition of 2 and 6 vol% Cr_7C_3 in to Stellite 12 coatings resulted in less wear loss, addition of 10 vol% Cr_7C_3 remarkably increased wear loss. Stellite 12+Cr_7C_3 coatings exhibited worse wear performance than Stellite 12 coatings at 700 °C (Table 6.2 and Table 6.14).

SEM studies were done on the worn surface of examined coatings for determining wear mechanism at different testing temperature. Worn surface topographies and related EDX patterns of Stellite 12+WC/W_2C, Stellite 12+TiC and Stellite 12+Cr_7C_3 coatings presented in Figure 6.30, Figure 6.31 and Figure 6.32, respectively, clearly revealed that the wear mechanism explained in the case of Stellite 12 coating at each testing temperate govern the wear progress of above mentioned examined coatings. Progressing wear by plasticity dominated mechanism at RT and moderate temperature and by oxidative wear mechanism at elevated temperature was also confirmed from the corresponding contact surface appearances of the Al_2O_3 ball presented in Figure B.17, Figure B.18 and Figure B.19.

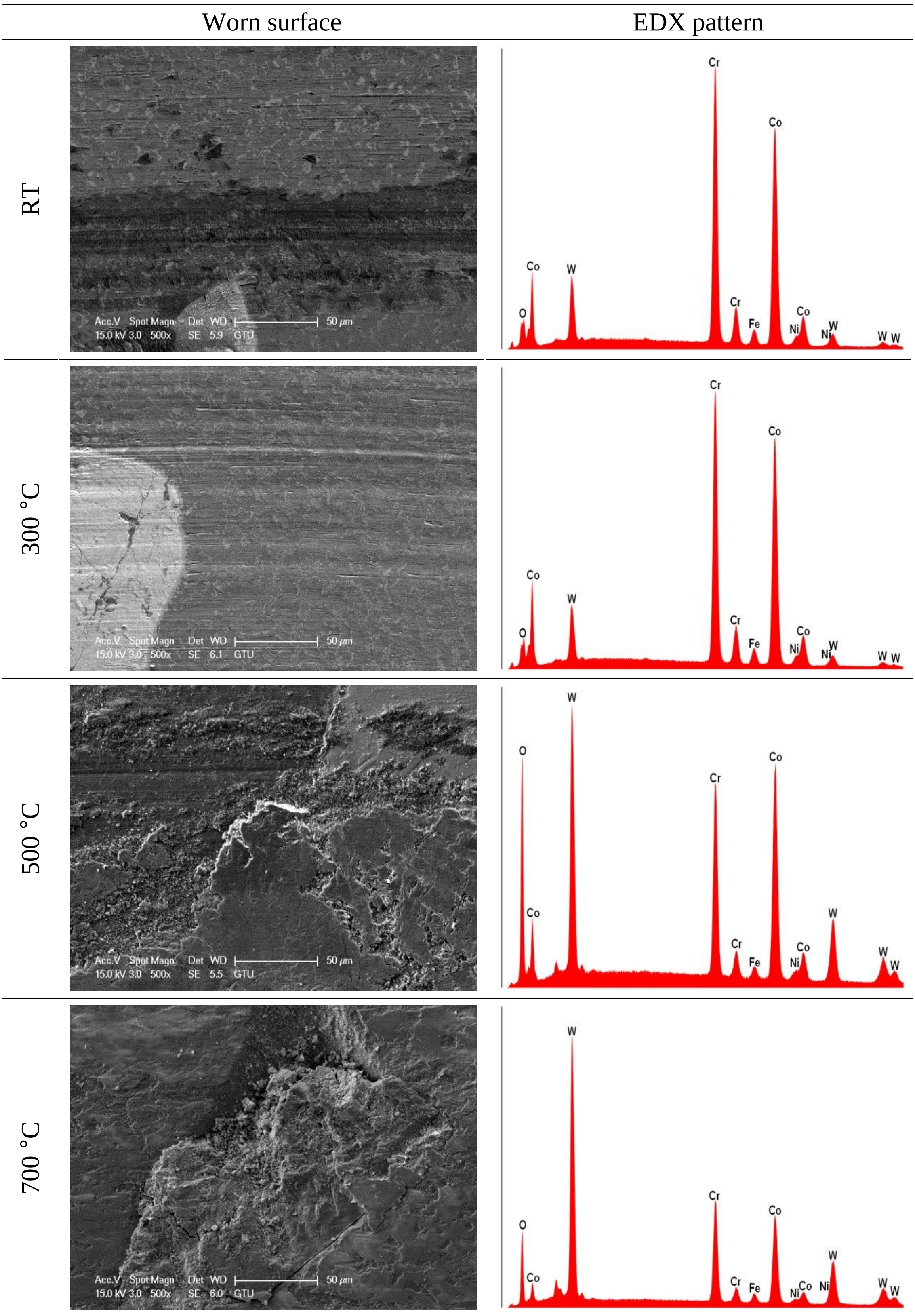

Figure 6.29 : The worn surface topographies and related EDX patterns of Stellite 12+10 vol% WC/W_2C coating after wear test.

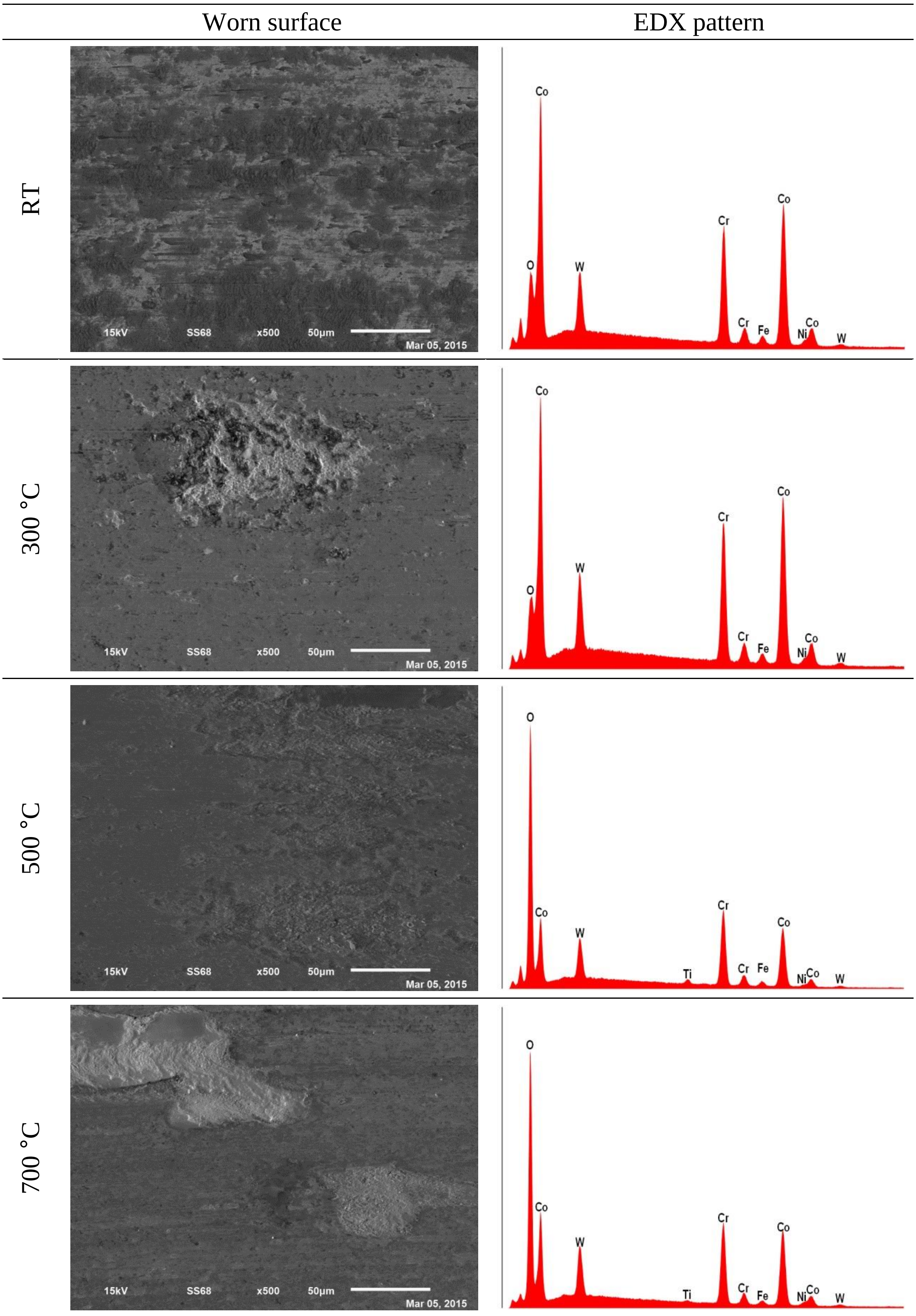

Figure 6.30 : The worn surface topographies and related EDX patterns of Stellite 12+10 vol% TiC coating after wear test.

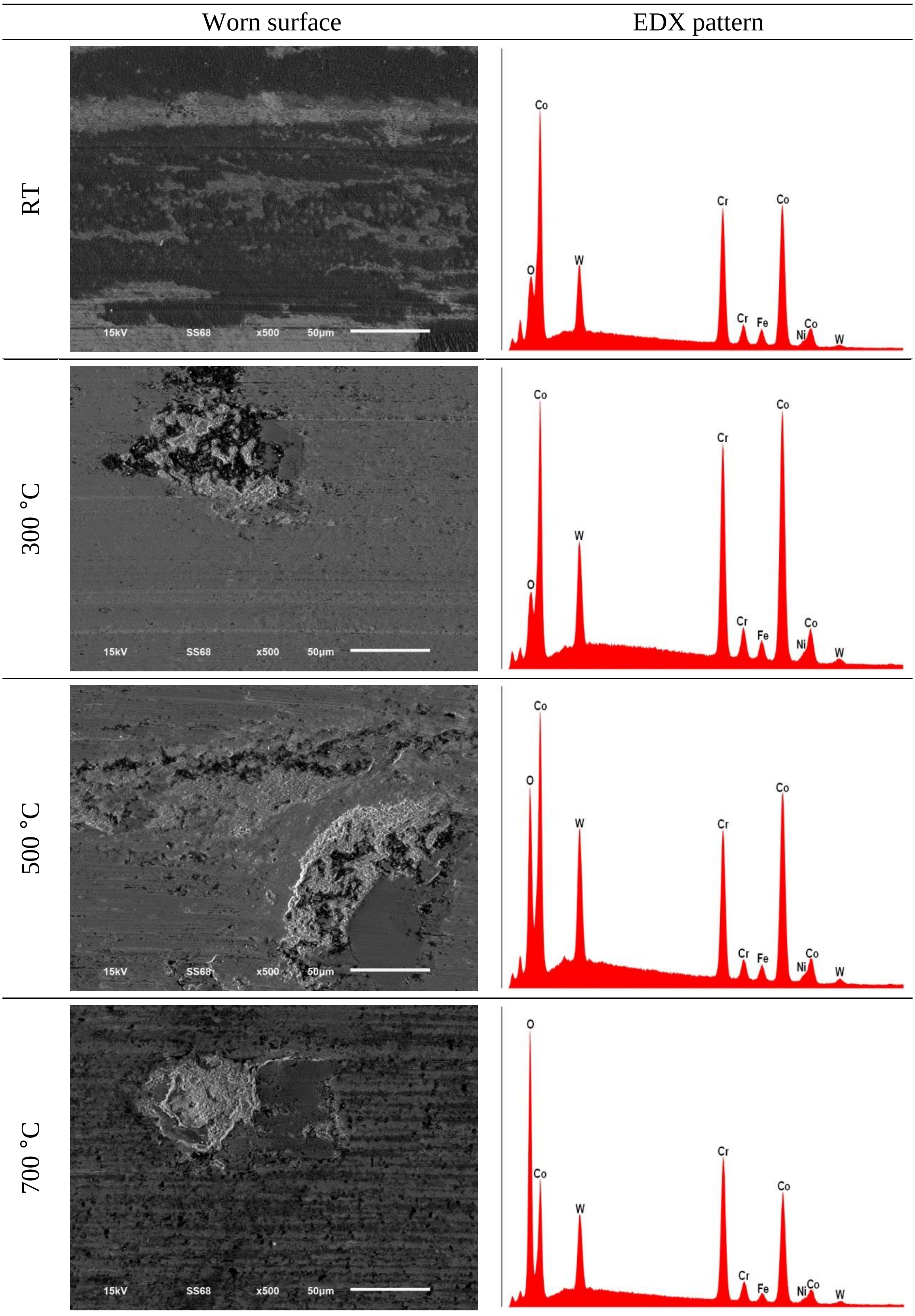

Figure 6.31 : The worn surface topographies and related EDX patterns of Stellite 12+10 vol% Cr_7C_3 coating after wear test.

Improvements in wear resistance of WC/W_2C added Stellite 12 coating at RT and 300 °C can be attributed to development of complex carbide (Co_3W_3C and Co_6W_6C) and intermetallics (Co_3W) and also dissolution of W in the Co-rich matrix (Table 6.8) which enhanced the hardness of matrix [17, 48, 141, 142, 183]. The role of dissolution of W and matrix hardness is important since the wear mechanism is plasticity dominated mechanism [32]. In addition to the changes in the microstructure presence of unmelted or partially melted WC/W_2C particles (with hardness of 1850 $HV_{0.5}$) on the wear path has significant effect on the reduction of wear loss by reducing direct contact between the Al_2O_3 ball and examined coatings. At the testing temperature of 500 and 700 °C formation of an oxide film confirmed by SEM micrographs and the evidence of strong oxygen peaks on the relevant EDX patterns, play a crucial role on the reduction of wear loss. As it is obvious in Figure B.17, formation of an oxide film was accompanied by limited material transfer to the contact surface of the Al_2O_3 ball on the worn surface and also resulted in smaller wear scare on it. Raman spectroscopy analyses conducted on the worn surface of Stellite 12+10 vol% WC/W_2C coating tested at 500 and 700 °C are presented in Figure 6.32. The oxide film formed on the worn surface of Stellite 12+10 vol% WC/W_2C coating tested at 500 °C was composed of mainly Co_3O_4 and Cr_2O_3 and signal of minor oxide (WO_3) was also detected. Development of Cr_2O_3 on the worn surface of examined coating after testing at 500 °C can be attributed to the dissolution of W atom in Co-rich solid solution matrix (Table 6.8). It is well-documented that addition of W to Stellite alloys can be beneficial in outward diffusion of chromium atoms dissolved in Co-rich solid solution matrix and promoting the formation of Cr_2O_3 [166]. Also increasing amount of dissolved W atom in matrix from 1.76 at% (Table 6.1) to 3.19 at% (Table 6.8) upon addition of 10 vol% WC/W_2C resulted in development of WO_3 in the oxide layer. Therefore at testing temperature of 500 °C remarkable reduction in wear loss of Stellite 12+WC/W_2C coating comparing with Stellite 12 coating can be attributed to good tribological properties and protective nature of Cr_2O_3 and WO_3 [154, 175, 184]. Increasing testing temperature to 700 °C resulted in development of $CoWO_4$ complex oxide in addition to Cr_2O_3 and Co_3O_4. It is noticeable that due to tendency of WO_3 to volatilize at 700 °C, outward diffused W atoms dissolved in the matrix, prefer to make solid reaction with cobalt and develop $CoWO_4$ complex oxide [173, 185, 186]. Therefore improvement in wear loss of the Stellite 12+WC/W_2C coating with increasing testing temperature from 500 °C to 700 °C (Table 6.12) can be attributed to the formation of protective and lubricious $CoWO_4$ complex oxide within the oxide film of the worn surface [159, 186, 187].

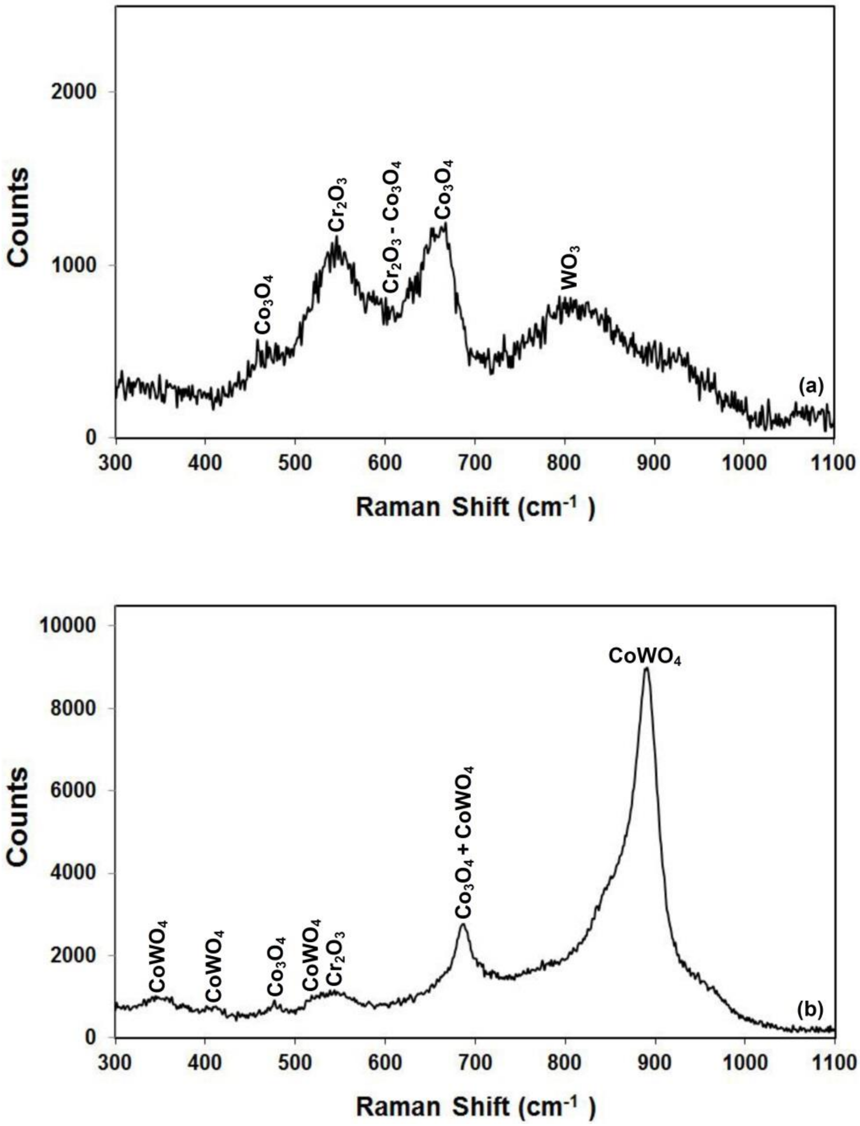

Figure 6.32 : Raman spectroscopy of worn surfaces of Stellite12+10 vol% WC/W_2C coating after testing at a) 500 and b) 700 °C.

It should be noted that oxidation and consequently volatilization of WC/W_2C reinforcement particles at 700 °C, resulted in their decomposition and fragmentation during sliding wear as seen in Figure 6.29. Some fragmented particles can remain between sliding Al_2O_3 ball and worn surface and act as three-body abradents. Therefore higher wear loss of Stellite 12+WC/W_2C coating comparing with Stellite 12+Mo coatings tested at 700 °C can be attributed to abrasive effect of fragmented WC/W_2C particle which resulted in break-down and removal of oxide layer [188]. The phenomenon of oxide layer break-down at testing temperature of 700 °C can be seen as fluctuation in friction coefficient curve of Stellite 12+10 vol% WC/W_2C coating presented in Figure B.10.

Enhancement in wear resistance of Stellite 12+TiC coating at RT and 300 °C can be attributed to enhancement in hardness of coatings due to formation of more Cr-rich carbides and Co/W-rich intermetallic compound in microstructure (Figure 6.23 and Table 6.9) upon addition of TiC particles. Also TiC particles (with hardness of 3200 $HV_{0.5}$) located on the wear path remarkably increased wear resistance of TiC containing coatings. Presence of TiC particle on wear path can reduce direct contact between the Al_2O_3 ball and examined coatings and consequently diminish plastic deformation of examined coating and removal of materials.

At testing temperature of 500 °C while 2 and 6 vol% containing TiC coatings yielded 46% less wear loss in comparison with Stellite12 coating, significant difference was not observed between wear loss of Stellite 12+10 vol % TiC coating and Stellite 12 coating. Addition of TiC particles into Stellite 12 coating leads to decrease in wear resistance at 700 °C as wear loss increase more than two times upon addition of 10 vol % TiC (Table 6.2 and Table 6.13). The results of Raman spectroscopy analyses presented in Figure 6.33 revealed that the oxide film formed on worn surface of Stellite 12+10 vol% TiC coating tested at 500 and 700 °C was composed of CoO and mainly Co_3O_4, respectively. In spite of observing the same Raman signals in Stellite 12 and Stellite 12+6 vol% TiC coatings (Figure 6.6 and Figure 6.33 a), lower wear resistance of Stellite 12+TiC coatings containing 2 and 6 vol% TiC at 500 °C can be associated with increasing hardness of coating. It is well-documented that when the hardness of PTA deposited coating increased and became stronger, its support to the oxide film on its surface enhanced [117]. At elevated temperature sliding wear tests, increasing hardness of deposited coatings and consequently decreasing plastic deformation of zone beneath the sliding ball can prevent easily break-down and removal of oxide films formed on worn surfaces and reduce the wear damages. However in the case of Stellite 12+10 vol% TiC coating formation of more Cr-rich carbides and decreasing volume fraction of Co-rich solid solution matrix (Table 6.5) inhibited the development of continuous protective CoO film on the worn surface and therefore contributed to the progress of wear [27, 135, 188].

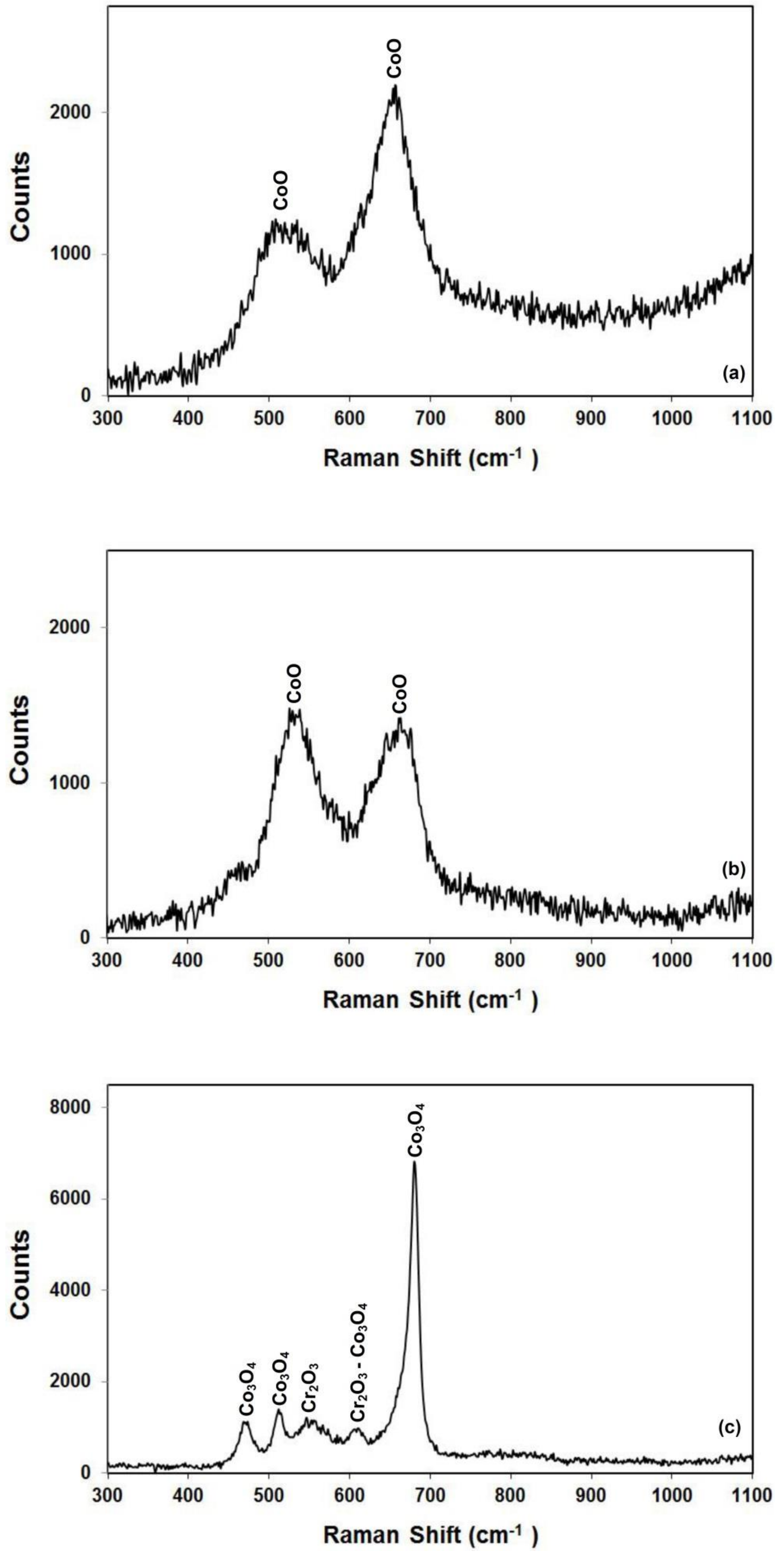

Figure 6.33 : Raman spectroscopy of worn surfaces of Stellite 12+6 vol% TiC after testing at a) 500 °C and Stellite 12+10 vol% TiC after testing at b) 500 °C and c) 700 °C.

At testing temperature of 700 °C, increasing wear loss of Stellite 12+TiC can be related to the composition of formed oxide film which was mainly Co_3O_4 and also reducing continuous oxide film formed on worn surfaces of coatings upon addition of TiC particles. Since addition of TiC particles changed solidification pattern and increased Cr-rich carbides, chromium atoms were tied up in these eutectic compounds and also Co-rich solid solution matrix decreased. Therefore chromium atoms do not afford quite as much protection as might be expected if they were free to migrate from dendritic solid solution matrix to the surface and form a continuous Cr_2O_3 layer [152].

Since hardness and amount of carbides or intermetallics in microstructure have significant effect on wear resistance of Stellite coating at moderate temperature, decreasing wear loss of Stellite 12+Cr_7C_3 coating can be attributed to large volume fraction of Cr-rich carbides developed upon addition of Cr_7C_3 particles [7, 62, 80, 151]. Also it should be noted that development of higher amount of Cr-rich carbides and reduction of dendritic matrix decreased the destructive effect of thin oxide film fragmentation at 300 °C.

At 500 and 700 °C addition of Cr_7C_3 particles in to Stellite 12 coating up to 10 vol% increased wear loss of examined coatings. At testing temperature of 500 °C while addition of 2 and 6 vol% Cr_7C_3 in to Stellite 12 coatings resulted in less wear loss, addition of 10 vol% Cr_7C_3 remarkably increased wear loss. Stellite 12+Cr_7C_3 coatings exhibited worse wear performance than Stellite 12 coatings at 700 °C (Table 6.9 and Table 6.14). Figure 6.36 and Figure 6.37 show the SEM micrographs of worn surfaces, related EDX patterns and corresponding contact surface appearances of the counter-face (Al_2O_3 ball), respectively.

According to the results of Raman spectroscopy analyses presented in Figure 6.35, the oxide film formed on worn surface of Stellite 12+10 vol% Cr_7C_3 coating tested at 500 and 700 °C was identified as CoO and mainly Co_3O_4, respectively. In comparison to the testing temperature of 300 °C, development of protective oxide film on the worn surface of 2 vol% containing Cr_7C_3 coating at 500 °C and 2, 6 and 10 vol% containing Cr_7C_3 coating at 700 °C led to reduction in wear loss. In spite of increasing hardness of deposited coating upon addition of Cr_7C_3, reduction of wear resistance of examined coating under oxidation dominated wear mechanism (at 500 and 700 °C) can be attributed to nature of oxide film cover the worn surfaces. Formation of more Cr-rich carbides and decreasing volume fraction of Co-rich solid solution matrix (Table 6.6) upon addition of Cr_7C_3 particles reduced the development of continuous and protective CoO and Co_3O_4 film on the worn surfaces at 500 and 700 °C respectively, and therefore contributed to the progress of wear [27, 135, 188]. At 500 °C not development of continuous oxide film (CoO) on the worn surfaces resulted in increasing direct contact of sliding alumina ball and the surface which may cause more plastic deformation and also more transferring of materials (Figure 6.37). Comparing the wear loss results at 500 and 700 °C indicated that increasing testing temperature to 700 °C promoted formation of thicker and more continuous oxide film on the worn surface. However reduction of wear resistance of examined coating upon addition of Cr_7C_3 particles can be associated with increasing amount of Cr-rich carbides and also consumption of more chromium atoms for development of Cr-rich eutectic compounds. As it was described previously increasing temperature favored outward diffusion of chromium atoms to form Cr_2O_3 in the oxide film, but due to reduction of dendritic solid solution matrix and lack of free chromium atoms, development of continuous Cr_2O_3 was inhibited and the protective nature of oxide film formed on the worn surface decreased [152].

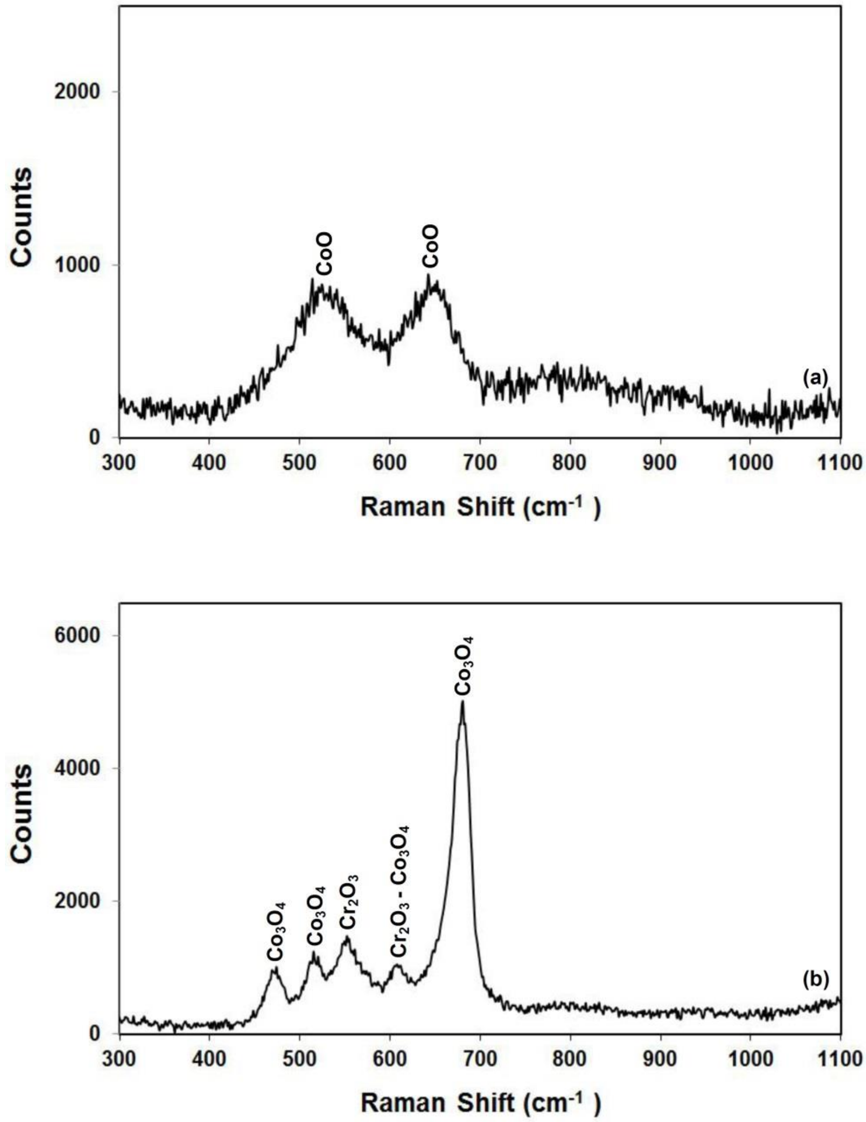

Figure 6.34 : Raman spectroscopy of worn surfaces of Stellite 12+10 vol% Cr_7C_3 after testing at a) 500 °C and b) 700 °C.

7. CONCLUSIONS AND RECOMENDATIONS

The results of this study can be stated as follow:
Stellite 12, alloyed and reinforced Stellite 12 coatings were successfully deposited on ASIS 4140 steel.

1-Microstructural investigation showed that Stellite 12 coating was composed of Co-rich solid solution dendritic matrix (α-Co) and lamellar mixture of Co-rich solid solution phase with Cr-rich carbides (Cr_7C_3 and $Cr_{23}C_6$), Co/W-rich complex carbides (Co_3W_3C, Co_6W_6C) and intermetallics (Co_3W, Co_7W_6) in the interdendritic region. The average hardness of the Stellite 12 was reported 490 ± 10 HV_2.

2-Addition of molybdenum up to 10 wt% into Stellite 12 coating reduced the volume fraction of the Co-rich dendritic matrix slightly and encouraged eutectic reaction to form Co_6Mo_6C complex carbide and Co_3Mo intermetallic compounds while formation of Cr_7C_3 was suppressed. As a result of the changes in the microstructure, the hardness of the Stellite 12 increased from 490 HV_2 to 621 HV_2 upon addition of 10 wt% molybdenum.

3-Ni element added into Stellite 12 coating was dissolved totally in Co-rich solid solution matrix without changing the microstructural constituents. Dissolution of Ni in dendritic solid solution matrix favored stabilization of α-Co at RT and reduced the hardness values of Ni containing Stellite 12 coatings. The hardness of Stellite 12 coating decreases from 490±10 HV_2 to 458±5 HV_2 upon addition of 10 (wt%) Ni.

4-Fully or partially melting of WC/W_2C reinforcement particles enriched the melt pool in W and C and favored the formation of more Co_3W_3C and Co_6W_6C complex carbide and Co_3W intermetallic compound in microstructure. Presence of unmelted particles changed the solidification pattern and refined the microstructure. Development of complex carbide and intermetallic compounds enhanced the hardness of Stellite 12+WC/W_2C coating as it reached to 642±5 upon addition of 10 wt% WC/W_2C.

5-Addition of TiC into Stellite 12 altered the volume fraction of compounds formed during solidification without changing chemical composition of constituents. Microstructural investigation showed that TiC did not melt or dissolve during PTA deposition process. As the volume fraction of TiC particles increased Co-rich dendrite matrix refined and the volume fraction of Cr_7C_3, $Cr_{23}C_6$ and Co_3W eutectic compounds increased. Hardness of Stellite 12+TiC coatings enhanced and reached to 580±8 upon addition of 10 vol% TiC.

6- The microstructure of Stellite 12+Cr_7C_3 coating consisted of α-Co (FCC), Cr_7C_3, $Cr_{23}C_6$ and Co_6W_6C compounds. Low melting point and high solubility of Cr_7C_3 particles in Co-based hardfacing alloys enriched the melt pool in Cr and C and increase in volume fraction of eutectic compounds.

7-In the sliding wear of the examined coatings depending on the testing temperature, two different mechanisms were identified. Plasticity dominated wear mechanism at RT and 300 °C affected by hardness and work hardening of deposited coating and oxidative wear mechanism at high temperatures (500 and 700 °C) which formation of continues and protective oxide film significantly influenced on wear performance. In all examined coatings the area of the wear tracks varied remarkably with the testing temperature and testing temperature of 300 and 500 ^{o}C induced bigger wear track areas than those formed at RT and 700 ^{o}C. Reduction in the work hardening rate and mechanical strength and/or easy destruction of thin and less adherent oxide films covering the worn surface of examined coating accelerate the progress of wear on Stellite alloys at 300 °C as compared to RT.

Addition of Mo into the Stellite 12 coating reduced the wear track area at all testing temperatures. As the results of the changes in the microstructure, the addition of 2, 6 and 10 wt% Mo improved the hardness of the Stellite 12 coating (Table 6.5) and provided a lower wear loss (Table 6.6). Development of Cr_2O_3 and $CoMoO_4$ at 500 and 700 °C was beneficial in reduction of wear loss.

Addition of Ni into Stellite 12 resulted in increased of wear loss of examined coating at all testing temperature. Decreasing hardness of coatings and work hardening of Co-rich solid solution matrix had significant effect on reduction of wear resistance at RT.

Development of complex carbide (Co_3W_3C and Co_6W_6C) and intermetallics (Co_3W) and also dissolution of W in the Co-rich matrix enhanced the hardness and consequently the wear resistance of Stellite 12+WC/W_2C coatings at RT and 300 °C. In comparison to Stellite 12 development of Cr_2O_3 at testing temperature of 500 °C remarkably reduced the wear loss of Stellite 12+WC/W_2C coating. Increasing testing temperature to 700 °C resulted in development of $CoWO_4$ complex oxide in addition to Cr_2O_3 and Co_3O_4. Improvement in wear loss of the Stellite 12+WC/W_2C coating with increasing testing temperature from 500 °C to 700 °C was attributed to protective and lubricious nature of $CoWO_4$ complex oxide.

Addition of TiC reinforcement particles into Stellite 12 improved wear resistance at RT, 300 and 500 °C, but increased the wear loss at testing temperature of 700 °C. While increasing amount of reinforcement particles led to decrease wear loss at RT and 300 C, wear resistance of examined coating decreased at 500 and 700 C. Although enhancement of hardness was beneficial in supporting of oxide film on the worn surface of coating at elevated temperature but deficiency in development of continuous and protective oxide film due to formation of more Cr-rich carbides and decreasing volume fraction of Co-rich solid solution matrix contributed to the progress of wear.

In the case of Stellite 12+Cr_7C_3 coating formation of large volume fraction of Cr-rich carbides contributed to reduction of wear loss at RT and 300 °C. At 500 and 700 °C addition of Cr_7C_3 particles in to Stellite 12 coating up to 10 vol% increased wear loss of examined coatings. At testing temperature of 500 °C while addition of 2 and 6 vol% Cr_7C_3 in to Stellite 12 coatings resulted in less wear loss, addition of 10 vol% Cr_7C_3 remarkably increased wear loss. Stellite 12+Cr_7C_3 coatings exhibited worse wear performance than Stellite 12 coatings at 700 °C.

Not development of adequate continuous and protective Cr_2O_3 and Co_3O_4 oxide film on the worn surface was identifies as a main reason of increasing wear loss at elevated temperature.

As a result of this investigation, when a combination of microstructural characteristics, hardness and wear behavior of examined samples at RT and high temperature is of concern, the addition of 10 wt% Mo as a alloying element and introducing 10 vol% WC/W_2C as a reinforcement particle for enhancing the hardness and wear resistance of Stellite 12 coatings is recommended.

REFERNCES

[1] **Holmberg, K. and Matthews, A.** (2009). *Coatings Tribology: Properties, Mechanisms, Techniques and Applications in Surface Engineering* (2nd ed.): Elsevier Science.

[2] **Buchely, M.F., Gutierrez, J.C., León, L.M., and Toro, A.** (2005). The effect of microstructure on abrasive wear of hardfacing alloys, *Wear*, *259*, 52-61.

[3] **Chen, D., Liu, D., Liu, Y., Wang, H., and Huang, Z.** (2014). Microstructure and fretting wear resistance of γ/TiC composite coating in situ fabricated by plasma transferred arc cladding, *Surface and Coatings Technology*, *239*, 28-33.

[4] **Radu, I. and Li, D.Y.** (2007). The wear performance of yttrium-modified Stellite 712 at elevated temperatures, *Tribology International*, *40*, 254-265.

[5] **Gualco, A., Svoboda, H.G., Surian, E.S., and de Vedia, L.A.** (2010). Effect of welding procedure on wear behaviour of a modified martensitic tool steel hardfacing deposit, *Materials and Design*, *31*, 4165-4173.

[6] **D'Oliveira, A.S.C.M., Paredes, R.S.C., and Santos, R.L.C.** (2006). Pulsed current plasma transferred arc hardfacing, *Journal of Materials Processing Technology*, *171*, 167-174.

[7] **Shin, J.C., Doh, J.M., Yoon, J.K., Lee, D.Y., and Kim, J.S.** (2003). Effect of molybdenum on the microstructure and wear resistance of cobalt-base Stellite hardfacing alloys, *Surface and Coatings Technology*, *166*, 117-126.

[8] **Hsieh, C.C., Liu, Y.C., Wang, J.S., and Wu, W.** (2014). Microstructural evolution with various Ti contents in Fe-based hardfacing alloys using a GTAW technique, *Metals and Materials International*, *20*, 701-712.

[9] **Freels, M., Liaw, P.K., Jiang, L., and Klarstrom, D.L.** (2006). Cobalt alloys and composites, in *Advanced Structural Materials Properties, Design Optimization, and Applications*, p. 187–224, Eds. Soboyejo, W.O. and Srivatsan, T.S., CRC Press Publication, Florida, USA.

[10] **Kostick, J.A., Segall, A.E., Conway, J.C., Amateau, M.F., and Opet, S.** (1997). The sliding wear behavior of cobalt-based hardfacing alloys used in steam valve applications©, *Tribology Transactions*, *40*, 168-172.

[11] **Liu, R. and Yao, M.X.** (2013). High-Performance Wear/Corrosion-Resistant Superalloys, in *Aerospace Materials Handbook*, p. 151-236, Eds. Zhang, S. and Zhao, D., CRC Press Publication, Florida, USA.

[12] **Campbell, F.C.** (2008). *Elements of Metallurgy and Engineering Alloys*, Ohio, USA: ASM International.

[13] **Deng, H., Shi, H., and Tsuruoka, S.** (2010). Influence of coating thickness and temperature on mechanical properties of steel deposited with Co-based alloy hardfacing coating, *Surface and Coatings Technology*, *204*, 3927-3934.

[14] **Davis, J.R.** (2000). *Nickel, Cobalt, and Their Alloys*, ASM Specialty Handbook, Ohio, USA: ASM International.

[15] **Kuzucu, V., Ceylan, M., Celik, H., and Aksoy, I.** (1997). Microstructure and phase analyses of Stellite 6 plus 6 wt.% Mo alloy, *Journal of Malerials Processing Technology*, *69*, 257-263.

[16] **Xu, G., Kutsuna, M., and Rathod, M.** (2006). Cladding of Stellite-6 and vanadium carbide on carbon steel using a yttrium–aluminum–garnet laser robot system, *Journal of Laser Applications*, *18*, 47-55.

[17] **Zhong, M., Liu, W., Yao, K., Goussain, J.C., Mayer, C., and Becker, A.** (2002). Microstructural evolution in high power laser cladding of Stellite 6+WC layers, *Surface and Coatings Technology*, *157*, 128-137.

[18] **Chiang, K.A. and Chen, Y.C.** (2007). Microstructural characterization and microscopy analysis of laser cladding Stellite12 and tungsten carbide, *Journal of Materials Processing Technology*, *182*, 297-302.

[19] **Huang, P., Liu, R., Wu, X., and Yao, M.X.** (2007). Effects of molybdenum content and heat treatment on mechanical and tribological properties of a low-carbon Stellite® alloy, *Journal of Engineering Materials and Technology*, *129*, 523-529.

[20] **Liu, R., Yao, M.X., Patnaik, P.C., and Wu, X.J.** (2006). An improved wear-resistant PTA hardfacing: VWC/Stellite 21, *Journal of Composite Materials*, *40*, 2203-2215.

[21] **Wu, W. and Wu, L.T.** (1996). The wear behavior between hardfacing materials, *Metallurgical and Materials Transactions A*, *27*, 3639-3648.

[22] **Berns, H.** (1995). Microstructural properties of wear-resistant alloys, *Wear*, *181-183*, 271-279.

[23] **Modi, O.P., Prasad, B.K., Jha, A.K., Deshmukh, V.P., and Shah, A.K.** (2004). Effects of material composition and microstructural features on dry sliding wear behaviour of Fe–TiC composite and a cobalt-based stellite, *Tribology Letters*, *17*, 129-138.

[24] **Holmberg, K., Laukkanen, A., Turunen, E., and Laitinen, T.** (2014). Wear resistance optimisation of composite coatings by computational microstructural modelling, *Surface and Coatings Technology*, *247*, 1-13.

[25] **Lu, F., Li, H., Ji, Q., Zeng, R., Wang, S., Chi, J., Li, M., Chai, L., and Xu, H.** (2011). Characteristics of the functionally graded coating fabricated by plasma transferred arc centrifugal cladding, *Surface and Coatings Technology*, *205*, 4441-4446.

[26] **Chen, H., Xu, C., Qu, J., Hutchings, I.M., Shipway, P.H., and Liu, J.** (2005). Sliding wear behaviour of laser clad coatings based upon a nickel-

based self-fluxing alloy co-deposited with conventional and nanostructured tungsten carbide–cobalt hardmetals, *Wear*, *259*, 801-806.

[27] **Schlager, D., Theiler, C., and Kohn, H.** (2002). Protection against high temperature corrosion with laser welded claddings - Applied and tested on exhaust valve discs of large diesel engines burning heavy fuel oil, *Materials and Corrosion*, *53*, 103-110.

[28] **Chakraborty, G., Kumar, N., Das, C.R., Albert, S.K., Bhaduri, A.K., Dash, S., and Tyagi, A.K.** (2014). Study on microstructure and wear properties of different nickel base hardfacing alloys deposited on austenitic stainless steel, *Surface and Coatings Technology*, *244*, 180-188.

[29] **Leech, P.W., Li, X.S., and Alam, N.** (2012). Comparison of abrasive wear of a complex high alloy hardfacing deposit and WC–Ni based metal matrix composite, *Wear*, *294-295*, 380-386.

[30] **Wang, X.H., Han, F., Liu, X.M., Qu, S.Y., and Zou, Z.D.** (2008). Effect of molybdenum on the microstructure and wear resistance of Fe-based hardfacing coatings, *Materials Science and Engineering A*, *489*, 193-200.

[31] **Su, Y.L. and Chen, K.Y.** (1997). The influence of niobium, chromium, molybdenum and carbon on the sliding bear behavior of nickel-base hardfacing alloys, *Wear*, *209*, 160-170.

[32] **Tuominen, J.** (2009). Engineering coatings by laser cladding-The study of wear and corrosion properties (PhD Thesis*)*, Tampere University of Technology, Finland.

[33] **Su, Y.L. and Chen, K.Y.** (1997). Effect of alloy additions on wear resistance of nickel based hardfacing, *Welding Journal*, *76*, 143-150.

[34] **Liyanage, T.** (2010). Microstructure and properties of Ni-Alloy and Ni-WC composite overlays, (PhD Thesis*)*, University of Alberta, Alberta, Canada.

[35] **Sari, N.Y. and Yilmaz, M.** (2008). Improvement of wear resistance of wire drawing rolls with Cr–Ni–B–Si+WC thermal spraying powders, *Surface and Coatings Technology*, *202*, 3136-3141.

[36] **Miguel, J.M., Guilemany, J.M., and Vizcaino, S.** (2003). Tribological study of NiCrBSi coating obtained by different processes, *Tribology International*, *36*, 181-187.

[37] **Mendez, J., Ghoreshy, M., Mackay, W.B.F., Smith, T.J.N., and Smith, R.W.** (2004). Weldability of austenitic manganese steel, *Journal of Materials Processing Technology*, *153-154*, 596-602.

[38] **Kim, J.H., Ko, K.H., Noh, S.D., Kim, G.G., and Kim, S.J.** (2009). The effect of boron on the abrasive wear behavior of austenitic Fe-based hardfacing alloys, *Wear*, *267*, 1415-1419.

[39] **Kim, J.H., Na, K.S., Kim, G.G., Oh, J.Y., Yoon, C.S., and Kim, S.J.** (2008). The effects of Mn and B on the cavitation erosion resistance of

austenitic Fe-base hardfacing alloys, *Materials Science and Engineering A*, *477*, 204-207.

[40] **Kim, J.K., Kim, G.M., and Kim, S.J.** (2001). The effect of manganese on the strain-induced martensitic transformation and high temperature wear resistance of Fe-20Cr-1C-1Si hardfacing alloy, *Journal of nuclear materials*, *289*, 263-269.

[41] **Yang, K., Yu, S., Li, Y., and Li, C.** (2008). Effect of carbonitride precipitates on the abrasive wear behaviour of hardfacing alloy, *Applied Surface Science*, *254*, 5023-5027.

[42] **Kirchgaßner, M., Badisch, E., and Franek, F.** (2008). Behaviour of iron-based hardfacing alloys under abrasion and impact, *Wear*, *265*, 772-779.

[43] **Sapate, S.G., Selokar, A., and Garg, N.** (2010). Experimental investigation of hardfaced martensitic steel under slurry abrasion conditions, *Materials and Design*, *31*, 4001-4006.

[44] **Berns, H. and Fischer, A.** (1987). Microstructure of Fe-Cr-C hardfacing alloys with additions of Nb, Ti and B, *Metallography*, *20*, 401-429.

[45] **Atamert, S.** (1988). Stability, wear resistance, and microstructure of iron, cobalt and nickel-based hardfacing alloys, (PhD Thesis*)*, University of Cambridge, UK.

[46] **Liu, H.Y., Yu, F.B., Meng, Q.S., Chen, S.P., and Wang, H.** (2012). Microstructure and properties of Fe–Cr–C hardfacing alloys reinforced with TiC–TiB_2, *Science and Technology of Welding and Joining*, *17*, 419-423.

[47] **Yu, H., Ahmed, R., and de Villiers Lovelock, H.** (2007). A comparison of the tribo-mechanical properties of a wear resistant cobalt-based alloy produced by different manufacturing processes, *Journal of Tribology*, *129*, 586.

[48] **Yao, M.X., Wu, J.B.C., and Xie, Y.** (2005). Wear, corrosion and cracking resistance of some W- or Mo-containing Stellite hardfacing alloys, *Materials Science and Engineering A*, *407*, 234-244.

[49] **Gholipour, A., Shamanian, M., and Ashrafizadeh, F.** (2011). Microstructure and wear behavior of stellite 6 cladding on 17-4 PH stainless steel, *Journal of Alloys and Compounds*, *509*, 4905-4909.

[50] **Wu, A.P., Ren, J.L., Peng, Z.S., Murakawa, H., and Ueda, Y.** (2000). Numerical simulation for the residual stresses of Stellite hard-facing on carbon steel, *Journal of Materials Processing Technology*, *101*, 70-75.

[51] **Ning, Y., Patnaik, P.C., Liu, R., Yao, M.X., and Wu, X.J.** (2005). Effects of fabrication process and coating of reinforcements on the microstructure and wear performance of Stellite alloy composites, *Materials Science and Engineering A*, *391*, 313-324.

[52] **Yang, L.J. and Loh, N.L.** (1995). The wear properties of plasma transferred arc cladded stellite specimens, *Surface and Coatings Technology*, *71*, 196-200.

[53] **Url-1** <http://www.kennametal.com/en/home.html>, date retrieved 20.11.2014.

[54] **Khoddamzadeh, A., Liu, R., Liang, M., and Yang, Q.** (2012). Novel wear-resistant materials – Carbon fiber reinforced low-carbon Stellite alloy composites, *Composites Part A: Applied Science and Manufacturing*, *43*, 344-352.

[55] **Apay, S. and Gulenc, B.** (2014). Wear properties of AISI 1015 steel coated with Stellite 6 by microlaser welding, *Materials and Design*, *55*, 1-8.

[56] **Malayoglu, U. and Neville, A.** (2005). Mo and W as alloying elements in Co-based alloys—their effects on erosion–corrosion resistance, *Wear*, *259*, 219-229.

[57] **Silence, W.L.** (1978). Effect of structure on wear resistance of Co-, Fe-, and Ni-base alloys, *Journal of Tribology*, *100*, 428-435.

[58] **Hidouci, A., Pelletier, J.M., Ducoin, F., Dezert, D., and El Guerjouma, R.** (2000). Microstructural and mechanical characteristics of laser coatings, *Surface and Coatings Technology*, *123*, 17-23.

[59] **Wang, X.H., Zou, Z.D., and Qu, S.Y.** (2006). Microstructure of Fe-based alloy hardfacing coating reinforced by TiC-VC particles, *Journal of Iron and Steel Research, International*, *13*, 51-55.

[60] **Kapoor, S., Liu, R., Wu, X.J., and Yao, M.X.** (2012). Temperature-dependence of hardness and wear resistance of Stellite alloys, *World Academy of Science, Engineering and Technology*, *67*, 964-973.

[61] **De Mol Van Otterloo, J.L. and De Hosson, J.T.M.** (1997). Microstructural features and mechanical properties of a cobalt-based laser coating, *Acta Materialia*, *45*, 1225-1236.

[62] **Yao, M.X., Wu, J.B.C., Xu, W., and Liu, R.** (2005). Metallographic study and wear resistance of a high-C wrought Co-based alloy Stellite 706K, *Materials Science and Engineering A*, *407*, 291-298.

[63] **Suetin, D.V., Shein, I.R., and Ivanovskii, A.L.** (2009). Structural, electronic and magnetic properties of η carbides (Fe_3W_3C, Fe_6W_6C, Co_3W_3C and Co_6W_6C) from first principles calculations, *Physica B: Condensed Matter*, *404*, 3544-3549.

[64] **Kashani, H., Amadeh, A., and Ohadizadeh, A.** (2006). Effect of temperature on the strain induced $\gamma \rightarrow \varepsilon$ phase transformation in Stellite 21 during wear test, *Materials Science and Engineering A*, *435-436*, 474-477.

[65] **Yao, M.X., Wu, J.B.C., Yick, S., Xie, Y., and Liu, R.** (2006). High temperature wear and corrosion resistance of a Laves phase strengthened Co–Mo–Cr–Si alloy, *Materials Science and Engineering A*, *435-436*, 78-83.

[66] **Pradeep, G.R.C., Ramesh, A., and Durga Prasad, B.** (2010). A review paper on hardfacing processes and materials, *International Journal of Engineering Science and Technology*, *2*, 6507-6510.

[67] **Adoberg, E., Podgurski, V., Antonov, M., Sarjas, H., Žikin, A., Kulu, P., and Veinthal, R.** (2012). Coatings and surface engineering. Industry oriented research, *Estonian Journal of Engineering*, *18*, 176-184.

[68] **Zikin, A., Ilo, S., Kulu, P., Hussainova, I., Katsich, C., and Badisch, E.** (2012). Plasma transferred arc (PTA) hardfacing of recycled hardmetal reinforced nickel-matrix surface composites, *Materials Science, 18*, 12-17.

[69] **Mendez, P.F., Barnes, N., Bell, K., Borle, S.D., Gajapathi, S.S., Guest, S.D., Izadi, H., Gol, A.K., and Wood, G.** (2014). Welding processes for wear resistant overlays, *Journal of Manufacturing Processes*, *16*, 4-25.

[70] **Madadi, F., Shamanian, M., and Ashrafizadeh, F.** (2009). Cladding of stellite composite on carbon steel by gas tungsten arc welding (GTAW), *International Journal of ISSI*, *6*, 34-37.

[71] **Xinhong, W., Lin, C., Min, Z., and Zengda, Z.** (2009). Fabrication of multiple carbide particles reinforced Fe-based surface hardfacing layer produced by gas tungsten arc welding process, *Surface and Coatings Technology*, *203*, 976-980.

[72] **Badisch, E. and Kirchgaßner, M.** (2008). Influence of welding parameters on microstructure and wear behaviour of a typical NiCrBSi hardfacing alloy reinforced with tungsten carbide, *Surface and Coatings Technology*, *202*, 6016-6022.

[73] **Katsich, C., Zikin, A., and Badisch, E.** (2012). Wear protection of highly loaded components: advantages of plasma transferred arc welding as hardfacing technology. *8th International DAAAM Baltic Conference*, Tallinn, Estonia, April 19-21.

[74] **Veinthal, R., Sergejev, F., Zikin, A., Tarbe, R., and Hornung, J.** (2013). Abrasive impact wear and surface fatigue wear behaviour of Fe–Cr–C PTA overlays, *Wear, 301*, 102-108.

[75] **Zikin, A., Badisch, E., Hussainova, I., Tomastik, C., and Danninger, H.** (2013). Characterisation of TiC–NiMo reinforced Ni-based hardfacing, *Surface and Coatings Technology*, *236*, 36-44.

[76] **Economou, S., Bonte, M.D., Celis, J.P., Smith, R.W., and Lugscheider, E.** (1998). Processiog, structure and tribological behaviour of TiC-reinforced plasma sprayed coatings, *Wear*, *220*, 34-50.

[77] **Zahiri, R., Sundaramoorthy, R., Lysz, P., and Subramanian, C.** (2014). Hardfacing using ferro-alloy powder mixtures by submerged arc welding, *Surface and Coatings Technology*, *260*, 220-229.

[78] **Balasubrarnanian, V., Lakshminarayanan, A.K., Varahamoorthy, R., and S.Babu** (2009). Application of response surface methodology to prediction of dilution in plasma transferred arc hardfacing of stainless steel on carbon steel, *Journal of Iron and Steel Research, International*, *16*, 44-53.

[79] **Ramachandran, C.S., Balasubramanian, V., and Varahamoorthy, R.** (2009). Evaluation of dry sliding wear behaviour of plasma transferred arc hardfaced stainless steel, *Journal of Iron and Steel Research, International*, *16*, 49-54.

[80] **Lin, W.C. and Chen, C.** (2006). Characteristics of thin surface layers of cobalt-based alloys deposited by laser cladding, *Surface and Coatings Technology*, *200*, 4557-4563.

[81] **Navas, C., Conde, A., Cadenas, M., and de Damborenea, J.** (2006). Tribological properties of laser clad Stellite 6 coatings on steel substrates, *Surface Engineering*, *22*, 26-34.

[82] **Shang, S., Wellburn, D., Sun, Y.Z., Wang, S.Y., Cheng, J., Liang, J., and Liu, C.S.** (2014). Laser beam profile modulation for microstructure control in laser cladding of an NiCrBSi alloy, *Surface and Coatings Technology*, *248*, 46-53.

[83] **Url-2** <http://en.wikipedia.org/wiki/Cladding_(metalworking)>, date retrieved 25.12.2014.

[84] **Leunda, J., García Navas, V., Soriano, C., and Sanz, C.** (2014). Effect of laser tempering of high alloy powder metallurgical tool steels after laser cladding, *Surface and Coatings Technology*, *259*, 570-576.

[85] **Farahmand, P., Liu, S., Zhang, Z., and Kovacevic, R.** (2014). Laser cladding assisted by induction heating of Ni–WC composite enhanced by nano-WC and La_2O_3, *Ceramics International*, *40*, 15421-15438.

[86] **Wang, D., Hu, Q., and Zeng, X.** (2014). Microstructures and performances of $Cr_{13}Ni_5Si_2$ based composite coatings deposited by laser cladding and laser-induction hybrid cladding, *Journal of Alloys and Compounds*, *588*, 502-508.

[87] **Deuis, R.L., Yellup, J.M., and Subramanian, C.** (1998). Metal-matrix composite coatings by PTA surfacing, *Composite Science and Technology*, *58*, 299-309.

[88] **Rokanopoulou, A., Skarvelis, P., and Papadimitriou, G.D.** (2014). Microstructure and wear properties of the surface of 2205 duplex stainless steel reinforced with Al_2O_3 particles by the plasma transferred arc technique, *Surface and Coatings Technology*, *254*, 376-381.

[89] **Çelik, O.N.** (2013). Microstructure and wear properties of WC particle reinforced composite coating on Ti6Al4V alloy produced by the plasma transferred arc method, *Applied Surface Science*, *274*, 334-340.

[90] **Hou, Q.Y.** (2013). Influence of molybdenum on the microstructure and properties of a FeCrBSi alloy coating deposited by plasma transferred arc hardfacing, *Surface and Coatings Technology*, *225*, 11-20.

[91] **Hou, Q.Y., He, Y.Z., Zhang, Q.A., and Gao, J.S.** (2007). Influence of molybdenum on the microstructure and wear resistance of nickel-based alloy coating obtained by plasma transferred arc process, *Materials and Design*, *28*, 1982-1987.

[92] **Wang, W., Qian, S.Q., and Zhou, X.Y.** (2009). Microstructure and properties of TiN/Ni composite coating prepared by plasma transferred arc scanning process, *Transactions of Nonferrous Metals Society of China*, *19*, 1180-1184.

[93] **Zhao, C., Tian, F., Peng, H.R., and Hou, J.Y.** (2002). Non-transferred arc plasma cladding of Stellite Ni60 alloy on steel, *Surface and Coatings Technology*, *155*, 80-84.

[94] **Sidhu, T.S., Prakash, S., and Agrawal, R.D.** (2006). Characterisation of NiCr wire coatings on Ni- and Fe-based superalloys by the HVOF process, *Surface and Coatings Technology*, *200*, 5542-5549.

[95] **Sidhu, T.S., Prakash, S., and Agrawal, R.D.** (2006). Evaluation of hot corrosion resistance of HVOF coatings on a Ni-based superalloy in molten salt environment, *Materials Science and Engineering A*, *430*, 64-78.

[96] **Li, Q., Fan, D., and Xuan, Y.** (2014). Thermal radiative properties of plasma sprayed thermochromic coating, *Journal of Alloys and Compounds*, *583*, 516-522.

[97] **Wood, R.J.K.** (2010). Tribology of thermal sprayed WC–Co coatings, *International Journal of Refractory Metals and Hard Materials*, *28*, 82-94.

[98] **Url-3** <http://www.fst.nl/hvof/>, date retrieved 25.12.2014.

[99] **Abioye, T.E., McCartney, D.G., and Clare, A.T.** (2015). Laser cladding of Inconel 625 wire for corrosion protection, *Journal of Materials Processing Technology*, *217*, 232-240.

[100] **Cinca, N. and Guilemany, J.M.** (2013). Structural and properties characterization of stellite coatings obtained by cold gas spraying, *Surface and Coatings Technology*, *220*, 90-97.

[101] **Url-4** <http://www.fst.nl/about-thermal-spray-process/>, date retrieved 25.12.2014.

[102] **Rojacz, H., Zikin, A., Mozelt, C., Winkelmann, H., and Badisch, E.** (2013). High temperature corrosion studies of cermet particle reinforced NiCrBSi hardfacings, *Surface and Coatings Technology*, *222*, 90-96.

[103] **Berger, L.M.** (2015). Application of hardmetals as thermal spray coatings, *International Journal of Refractory Metals and Hard Materials*, *49*, 350-364.

[104] **Hou, Q.Y., Huang, Z., and Wang, J.T.** (2011). Influence of nano-Al_2O_3 particles on the microstructure and wear resistance of the nickel-based alloy coating deposited by plasma transferred arc overlay welding, *Surface and Coatings Technology*, *205*, 2806-2812.

[105] **Yaedu, A.E., da Silva, P.S.C.P., and d'Oliveira, A.S.C.M. (**2002). Influence of dilution on microstructure and mechanical properties of a cobalt-based alloy deposited by Plasma Transferred Arc welding, *Universidade Federal do Paraná Thechnical Report,* Prazil.

[106] **Url-5** <http://www.sulzer.com/>, date retrieved 04.12.2014.

[107] **Wolfe, T.B.B.** (2010). Homogeneity of metal matrix composites deposited by Plasma Transferred Arc welding, (PhD Thesis*)*, University of Alberta, Canada.

[108] **Yarmuch, M.A.R.** (2005). Effect of welding parameters on Plasma Transffered Arc Welding (PTAW) process for autogenous beads and 410SS-WC overlays, (MSc Thesis*)*, University of Alberta, Canada.

[109] **Keranen, M.** (2010). Effect of welding parameters of plasma transferred arc welding method on abrasive wear resistance of 12V tool steel deposit, (PhD Thesis*)*, Aalto University, Finland.

[110] **Bharath, R.R., Ramanathan, R., Sundararajan, B., and Srinivasan, P.B.** (2008). Optimization of process parameters for deposition of Stellite on X45CrSi93 steel by plasma transferred arc technique, *Materials and Design*, *29*, 1725-1731.

[111] **Suban, M. and Tusek, J.** (2001). Dependance of melting rate in MIG/MAG welding on the type of shielding gas used, *Journal of Materials Processing Technology*, *119*, 185-192.

[112] **Menzel, M.** (2003). The influence of individual components of an industrial gas mixture on the welding process and the properties of welded joints, *Welding International*, *17*, 262-264.

[113] **Bao, J.** (2004). Study of abrasive waterjet nozzle materials and Plasma Transferred Arc welding coatings, (PhD Thesis*)*, University of Missouri-Rolla, USA.

[114] **Siva, K., Murugan, N., and Raghupathy, V.P.** (2009). Modelling, analysis and optimisation of weld bead parameters of nickel based overlay deposited by plasma transferred arc surfacing, *Archive of Computational Materials Science and Surface Engineering*, *1*, 174-182.

[115] **Balamurugan, S. and Murugan, N.** (2014). Deign of experiment and optimization of Plasma Transferred Arc hardfacing on structural steel with titanium carbide, *Research Journal of Applied Sciences, Engineering and Technology*, *7*, 2362-2370.

[116] **Dasgupta, B. and Mukherjee, S.** (2013). Optimisation of weld bead parameters of nickel based overlay deposited by plasma transferred arc surfacing, *International Journal of Modern Engineering Research*, *3*, 1330-1335.

[117] **Wang, L. and Li, D.Y.** (2003). Effects of yttrium on microstructure, mechanical properties and high-temperature wear behavior of cast Stellite 6 alloy, *Wear*, *255*, 535-544.

[118] **Radu, I. and Li, D.Y.** (2005). Investigation of the role of oxide scale on Stellite 21 modified with yttrium in resisting wear at elevated temperatures, *Wear*, *259*, 453-458.

[119] **Farnia, A., Ghaini, F.M., Rao, J.C., Ocelík, V., and Hosson, J.T.M.D.** (2012). Effect of Ta on the microstructure and hardness of Stellite 6 coating deposited by low power pulse laser treatments, *Surface and Coatings Technology*, *213*, 278–284.

[120] **Liu, R., Yao, J.H., Zhang, Q.L., Yao, M.X., and Collier, R.** (2015). Sliding wear and solid-particle erosion resistance of a novel high-tungsten Stellite alloy, *Wear*, *322-323*, 41-50.

[121] **Hou, Q.Y.** (2013). Microstructure and wear resistance of steel matrix composite coating reinforced by multiple ceramic particulates using SHS reaction of Al–TiO_2–B_2O_3 system during plasma transferred arc overlay welding, *Surface and Coatings Technology*, *226*, 113-122.

[122] **Just, C., Badisch, E., and Wosik, J.** (2010). Influence of welding current on carbide/matrix interface properties in MMCs, *Journal of Materials Processing Technology*, *210*, 408-414.

[123] **Amado, J.M., Tobar, M.J., Yáñez, A., Amigó, V., and Candel, J.J.** (2011). Crack free tungsten carbide reinforced Ni(Cr) layers obtained by laser cladding, *Physics Procedia*, *12*, 338-344.

[124] **Wu, Q., Li, W., Zhong, N., Gang, W., and Haishan, W.** (2013). Microstructure and wear behavior of laser cladding VC–Cr_7C_3 ceramic coating on steel substrate, *Materials and Design*, *49*, 10-18.

[125] **Pierson, H.O.** (1996). *Handbook of Refractory Carbides & Nitrides: Properties, Characteristics, Processing and Applications*: Elsevier Science.

[126] **Music, D., Kreissig, U., Mertens, R., and Schneider, J.M.** (2004). Electronic structure and mechanical properties of Cr_7C_3, *Physics Letters A*, *326*, 473-476.

[127] **Gassmann, R.C.** (1996). Laser cladding with (WC+W_2C)Co-Cr-C and (WC+W_2C)/Ni-B-Si composites for enhanced abrasive wear resistance, *Materials Science and Technology*, *12*, 691-696.

[128] **Lou, D., Hellman, J., Luhulima, D., Liimatainen, J., and Lindroos, V.K.** (2003). Interactions between tungsten carbide (WC) particulates and metal matrix in WC-reinforced composites, *Materials Science and Engineering A*, *340*, 155-162.

[129] **Wang, X.H., Zou, Z.D., Qu, S.Y., and Song, S.L.** (2005). Microstructure and wear properties of Fe-based hardfacing coating reinforced by TiC particles, *Journal of Materials Processing Technology*, *168*, 89-94.

[130] **Wang, X.H., Han, F., Qu, S.Y., and Zou, Z.D.** (2008). Microstructure of the Fe-based hardfacing layers reinforced by TiC-VC-Mo_2C particles, *Surface and Coatings Technology*, *202*, 1502-1509.

[131] **Frenk, A. and Kurz, W.** (1994). Microstructural effects on the sliding wear resistance of a cobalt-based alloy, *Wear*, *174*, 81-91.

[132] **Li, M.X., He, Y.Z., and Sun, G.X.** (2004). Laser cladding Co-based alloy/SiCp composite coatings on IF steel, *Materials and Design*, *25*, 355-358.

[133] **Nurminen, J., Näkki, J., and Vuoristo, P.** (2009). Microstructure and properties of hard and wear resistant MMC coatings deposited by laser cladding, *International Journal of Refractory Metals and Hard Materials*, *27*, 472-478.

[134] **Bartkowski, D., Młynarczak, A., Piasecki, A., Dudziak, B., Gościański, M., and Bartkowska, A.** (2015). Microstructure, microhardness and corrosion resistance of Stellite-6 coatings reinforced with WC

particles using laser cladding, *Optics & Laser Technology*, *68*, 191-201.

[135] **Stott, F.H.** (1998). The role of oxidation in the wear of alloys, *Tribology International*, *31*, 61-71.

[136] **Erck, R.A. and Ajayi, O.O.** (2001). Analysis of sliding wear rate variation with nominal contact pressure. *International Joint Tribology Conference*, San Francisco, USA, October 22-24.

[137] **Aoh, J.N. and Chen, J.C.** (2001). On the wear characteristics of cobalt-based hardfacing layer after thermal fatigue and oxidation, *Wear*, *250*, 611-620.

[138] **Nsoesie, S., Liu, R., Jiang, K., and Liang, M.** (2013). High-temperature hardness and wear resistance of cobalt-based Tribaloy alloys, *International Journal of Material and Mechanical Engineering*, *2*, 48-56.

[139] **Stott, F.H.** (2002). High-temperature sliding wear of metals, *Tribology International*, *35*, 489-495.

[140] **Jiang, J., Stott, F.H., and Stack, M.M.** (2004). A generic model for dry sliding wear of metals at elevated temperatures, *Wear*, *256*, 973-985.

[141] **Inman, I.A., Rose, S.R., and Datta, P.K.** (2006). Studies of high temperature sliding wear of metallic dissimilar interfaces II: Incoloy MA956 versus Stellite 6, *Tribology International*, *39*, 1361-1375.

[142] **Aoh, J.N., Jeng, Y.R., Chu, E.L., and Wu, L.T.** (1999). On the wear behavior of surface clad layers under high temperature, *Wear*, *225–229*, 1114–1122.

[143] **Persson, D.H.E., Jacobson, S., and Hogmark, S.** (2003). The influence of phase transformations and oxidation on the galling resistance and low friction behaviour of a laser processed Co-based alloy, *Wear*, *254*, 1134-1140.

[144] **Kashani, H., Amadeh, A., and Ghasemi, H.M.** (2007). Room and high temperature wear behaviors of nickel and cobalt base weld overlay coatings on hot forging dies, *Wear*, *262*, 800-806.

[145] **Opris, C.D., Liu, R., Yao, M.X., and Wu, X.J.** (2007). Development of Stellite alloy composites with sintering/HIPing technique for wear-resistant applications, *Materials and Design*, *28*, 581-591.

[146] **Birol, Y.** (2010). High temperature sliding wear behaviour of Inconel 617 and Stellite 6 alloys, *Wear*, *269*, 664-671.

[147] **Wood, P.D., Evans, H.E., and Ponton, C.B.** (2011). Investigation into the wear behaviour of Stellite 6 during rotation as an unlubricated bearing at 600 °C, *Tribology International*, *44*, 1589-1597.

[148] **Çelik, H. and Kaplan, M.** (2004). Effects of silicon on the wear behaviour of cobalt-based alloys at elevated temperature, *Wear*, *257*, 606-611.

[149] **Shivamurthy, R.C., Kamaraj, M., Nagarajan, R., Shariff, S.M., and Padmanabham, G.** (2009). Slurry erosion characteristics and erosive wear mechanisms of Co-based and Ni-nased coatings formed by laser

surface alloying, *Metallurgical and Materials Transactions A*, *41*, 470-486.

[150] **Kuzucu, V., Ceylan, M., Çelik, H., and Aksoy, I.** (1998). Phase investigation of a cobalt base alloy containing Cr, Ni, W and C, *Journal of Materials Processing Technology*, *78*, 137-141.

[151] **Hejwowski, T.** (2006). Sliding wear resistance of Fe-, Ni- and Co-based alloys for plasma deposition, *Vacuum*, *80*, 1326-1330.

[152] **Blau, P.J.** (2010). Elevated-temperature tribology of metallic materials, *Tribology International*, *43*, 1203-1208.

[153] **Inman, I.A. and Datta, P.S.** (2011). Studies of high temperature sliding wear of metallic dissimilar interfaces IV: Nimonic 80A versus Incoloy 800HT, *Tribology International*, *44*, 1902-1919.

[154] **Korashy, A., Attia, H., Thomson, V., and Oskooei, S.** (2015). Characterization of fretting wear of cobalt-based superalloys at high temperature for aero-engine combustor components, *Wear*, *330-331*, 327-337.

[155] **Łojewska, J., Knapik, A., Jodłowski, P., Łojewski, T., and Kołodziej, A.** (2013). Topography and morphology of multicomponent catalytic materials based on Co, Ce and Pd oxides deposited on metallic structured carriers studied by AFM/Raman interlaced microscopes, *Catalysis Today*, *216*, 11-17.

[156] **Li, Y.S., Wang, K., He, P., Huang, B.X., and Kovacs, P.** (1999). Surface-enhanced Raman spectroelectrochemical studies of corrosion films on implant Co-Cr-Mo alloy in biosimulating solutions, *Juornal of Raman Spectroscopy*, *30*, 97-103.

[157] **Herrera, J.E. and Resasco, D.E.** (2004). Loss of single-walled carbon nanotubes selectivity by disruption of the Co–Mo interaction in the catalyst, *Journal of Catalysis*, *221*, 354-364.

[158] **Salamanca, M., Licea, Y.E., Echavarría, A., Jr., A.C.F., and Palacio, L.A.** (2009). Hydrothermal synthesis of new wolframite type trimetallic materials and their use in oxidative dehydrogenation of propane, *Physical Chemistry Chemical Physics*, *11*, 9583-9591.

[159] **Geng, Z., Li, S., Duan, D.L., and Liu, Y.** (2015). Wear behaviour of WC–Co HVOF coatings at different temperatures in air and argon, *Wear*, *330-331*, 348-353.

[160] **Xing, X., Gui, Y., Zhang, G., and Song, C.** (2015). $CoWO_4$ nanoparticles prepared by two methods displaying different structures and supercapacitive performances, *Electrochimica Acta*, *157*, 15-22.

[161] **Muthamizh, S., Giribabu, K., Manigandan, R., Munusamy, S., Kumar, S.P., Suresh, R., and Narayanan, V.** (2015). Room Temperature Synthesis, Characterization, and Photocatalytic Property of Cobalt Tungstate Nanoparticles, *International Journal of Innovative Research in Science, Engineering and Technology*, *4*, 146-150.

[162] **Pyper, O., Kaschner, A., and Thomsen, C.** (2002). In situ Raman spectroscopy of the electrochemical reduction of WO_3 thin films in

various electrolytes, *Solar Energy Materials and Solar Cells*, *71*, 511-522.

[163] **Valova, E., Georgieva, J., Armyanov, S., Sotiropoulos, S., Hubin, A., Baert, K., and Raes, M.** (2010). Morphology, Structure and Photoelectrocatalytic Activity of TiO[sub 2]/WO[sub 3] Coatings Obtained by Pulsed Electrodeposition onto Stainless Steel, *Journal of The Electrochemical Society*, *157*, D309.

[164] **Bolelli, G., Berger, L.-M., Bonetti, M., and Lusvarghi, L.** (2014). Comparative study of the dry sliding wear behaviour of HVOF-sprayed WC–(W,Cr)2C–Ni and WC–CoCr hardmetal coatings, *Wear*, *309*, 96-111.

[165] **Al-Megren, H.A., González-Cortés, S.L., Xiao, T., and Green, M.L.H.** (2007). A comparative study of the catalytic performance of Co-Mo and Co(Ni)-W carbide catalysts in the hydrodenitrogenation (HDN) reaction of pyridine, *Applied Catalysis A: General*, *329*, 36-45.

[166] **Birks N, M.G., Pettit FS** (2006). *Introduction to the high temperature oxidation of metals*, New York: Cambridge University Press.

[167] **Birol, Y.** (2011). A novel C-free Co-based alloy for high temperature tooling applications, *Materials Science and Engineering: A*, *528*, 1117-1124.

[168] **Liu, R., Xi, S.Q., Kapoor, S., and Wu, X.J.** (2010). Effects of chemical composition on solidification , microstructure and hardness of Co-Cr-W-Ni and Co-Cr-Mo-Ni alloy, *International Journal of Research and Reviews in Applied Sciences*, *5*, 110-122.

[169] **Hu, P., Liu, R., Liu, J., McRae, G., Yao, M.X., and Collier, R.** (2014). Advanced Stellite alloys with improved metal-on-metal bearing for hip implants, *Materials & Design*, *60*, 424-432.

[170] **Liu, Y., Yang, H., Tan, G., Miyazaki, S., Jiang, B., and Liu, Y.** (2004). Stress-induced FCC ↔ HCP martensitic transformation in CoNi, *Journal of Alloys and Compounds*, *368*, 157-163.

[171] **Liu, Y., Yang, H., Liu, Y., Jiang, B., Ding, J., and Woodward, R.** (2005). Thermally induced fcc↔hcp martensitic transformation in Co–Ni, *Acta Materialia*, *53*, 3625-3634.

[172] **Wagner HJ, H.A. (**1962). The physical metallurgy of cobalt-base superalloys, Ohio.

[173] **Yuduo, Z., Zhigang, Y., Chi, Z., and Hao, L.** (2010). Effect of Rhenium Addition on Isothermal Oxidation Behavior of Tribaloy T-800 Alloy, *Chinese Journal of Aeronautics*, *23*, 370-376.

[174] **Wood, P.D., Evans, H.E., and Ponton, C.B.** (2010). Investigation into the wear behaviour of Tribaloy 400C during rotation as an unlubricated bearing at 600°C, *Wear*, *269*, 763-769.

[175] **Erdemir, A., Li, S., and Yuansheng Jin, Y.** (2005). Relation of certain quantum chemical parameters to lubrication behavior of solid oxides, *International Journal of Molecular Sciences*, *6*, 203-218.

[176] **Guo, C., Zhou, J., Chen, J., Zhao, J., Yu, Y., and Zhou, H.** (2011). High temperature wear resistance of laser cladding NiCrBSi and NiCrBSi/WC-Ni composite coatings, *Wear*, *270*, 492-498.

[177] **Zhang, P., Wang, X., Guo, L., Cai, L., and Sun, H.** (2011). Characterization of in situ synthesized TiB2 reinforcements in iron-based composite coating, *Applied Surface Science*, *258*, 1592– 1598.

[178] **Xibao, W.** (2005). The metallurgical behavior of B_4C in the iron-based surfacing alloy during PTA powder surfacing, *Applied Surface Science*, *252*, 2021–2028.

[179] **Url-6** <http://stellite.com/Home/tabid/36/Default.aspx>, date retrieved

[180] **Zikin, A., Hussainova, I., Katsich, C., Badisch, E., and Tomastik, C.** (2012). Advanced chromium carbide-based hardfacings, *Surface and Coatings Technology*, *206*, 4270-4278.

[181] **Li, S., Feng, D., and Luo, H.** (2007). Microstructure and abrasive wear performance of chromium carbide reinforced Ni3Al matrix composite coating, *Surface and Coatings Technology*, *201*, 4542-4546.

[182] **Zhang, D.-W. and Lei, T.C.** (2003). The microstructure and erosive–corrosive wear performance of laser-clad Ni–Cr3C2 composite coating, *Wear*, *255*, 129-133.

[183] **Xu, G., Kutsuna, M., Liu, Z., and Sun, L.** (2006). Characteristic behaviours of clad layer by a multi-layer laser cladding with powder mixture of Stellite-6 and tungsten carbide, *Surface and Coatings Technology*, *201*, 3385-3392.

[184] **Liu, L., Wu, S., Yu, G., and Chen, Y.** (2013). Oxidation behaviour and mechanism of a cobalt based superalloy between 1050 and 1250°C, *Applied Surface Science*, *283*, 590-598.

[185] **Yan, H.Y., Vorontsov, V.A., and Dye, D.** (2014). Effect of alloying on the oxidation behaviour of Co–Al–W superalloys, *Corrosion Science*, *83*, 382-395.

[186] **Engqvist, H., Hogberg, H., Botton, G.A., Ederyd, S., and Axen, N.** (2000). Tribofilm formation on cemented carbides in dry sliding conformal contact, *Wear*, *239*, 219–228.

[187] **Aristizabal, M., Ardila, L.C., Veiga, F., Arizmendi, M., Fernandez, J., and Sánchez, J.M.** (2012). Comparison of the friction and wear behaviour of WC–Ni–Co–Cr and WC–Co hardmetals in contact with steel at high temperatures, *Wear*, *280-281*, 15-21.

[188] **Varga, M., Rojacz, H., Winkelmann, H., Mayer, H., and Badisch, E.** (2013). Wear reducing effects and temperature dependence of tribolayer formation in harshenvironment, *Tribology International*, *65*, 190-199.

APPENDICES

APPENDIX A: Particle size distributions of powders used in PTA deposition process

APPENDIX B: 2-D profiles of the wear tracks and recorded friction coefficient curves of examined coatings at RT and elevated temperature

APPENDIX A

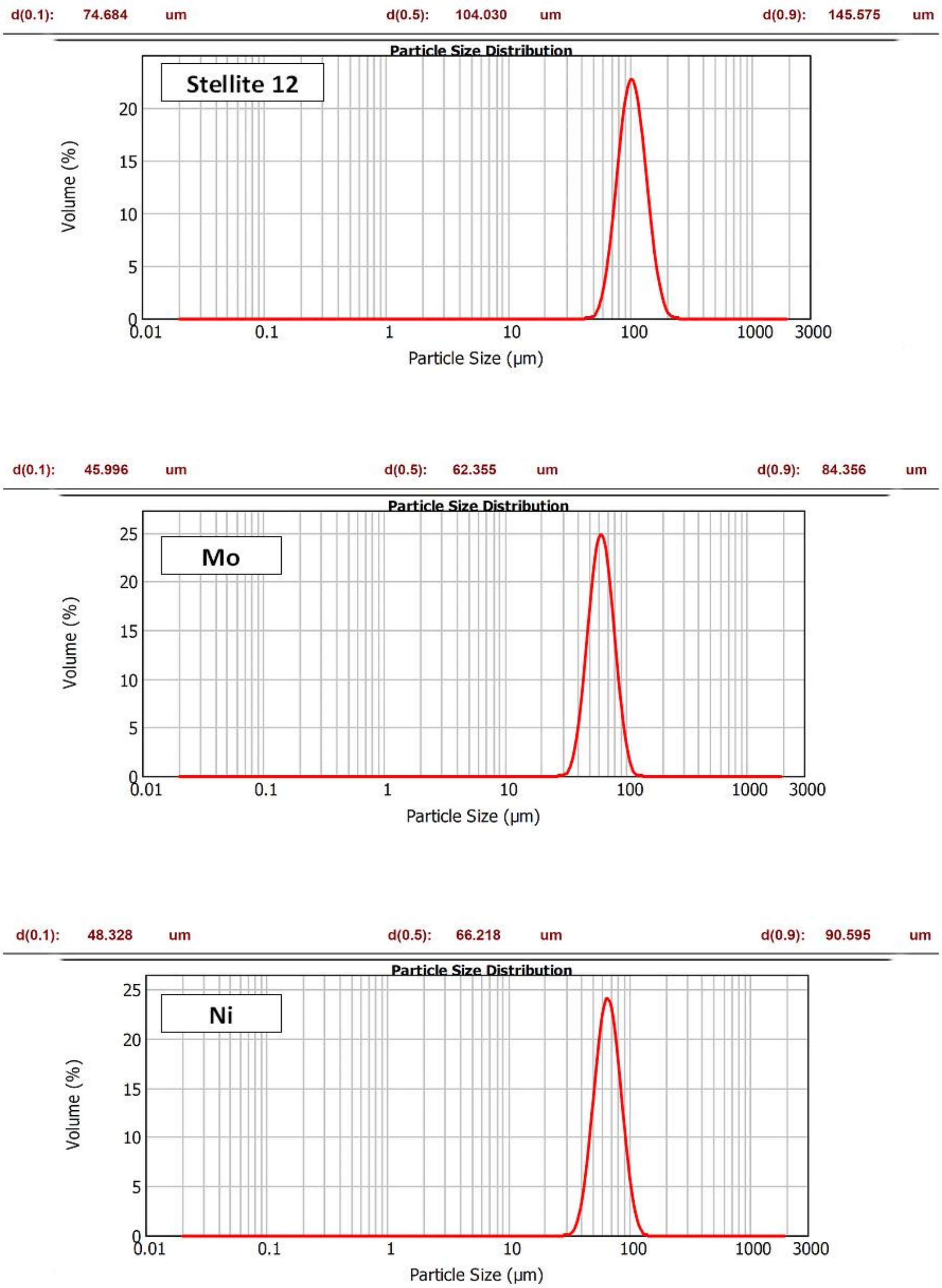

Figure A.1 : Particle size distributions of powders used in PTA deposition process.

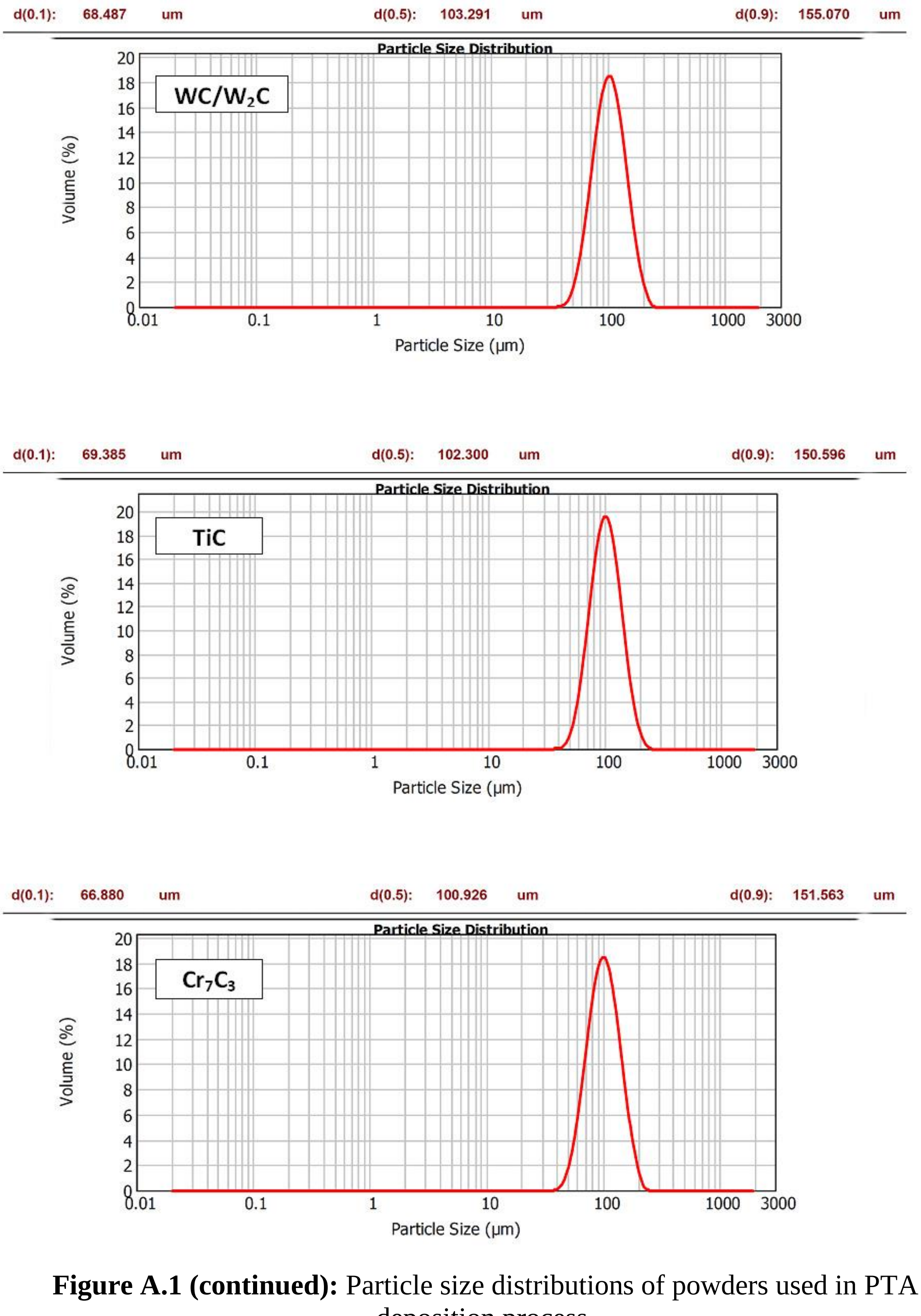

Figure A.1 (continued): Particle size distributions of powders used in PTA deposition process.

APPENDIX B

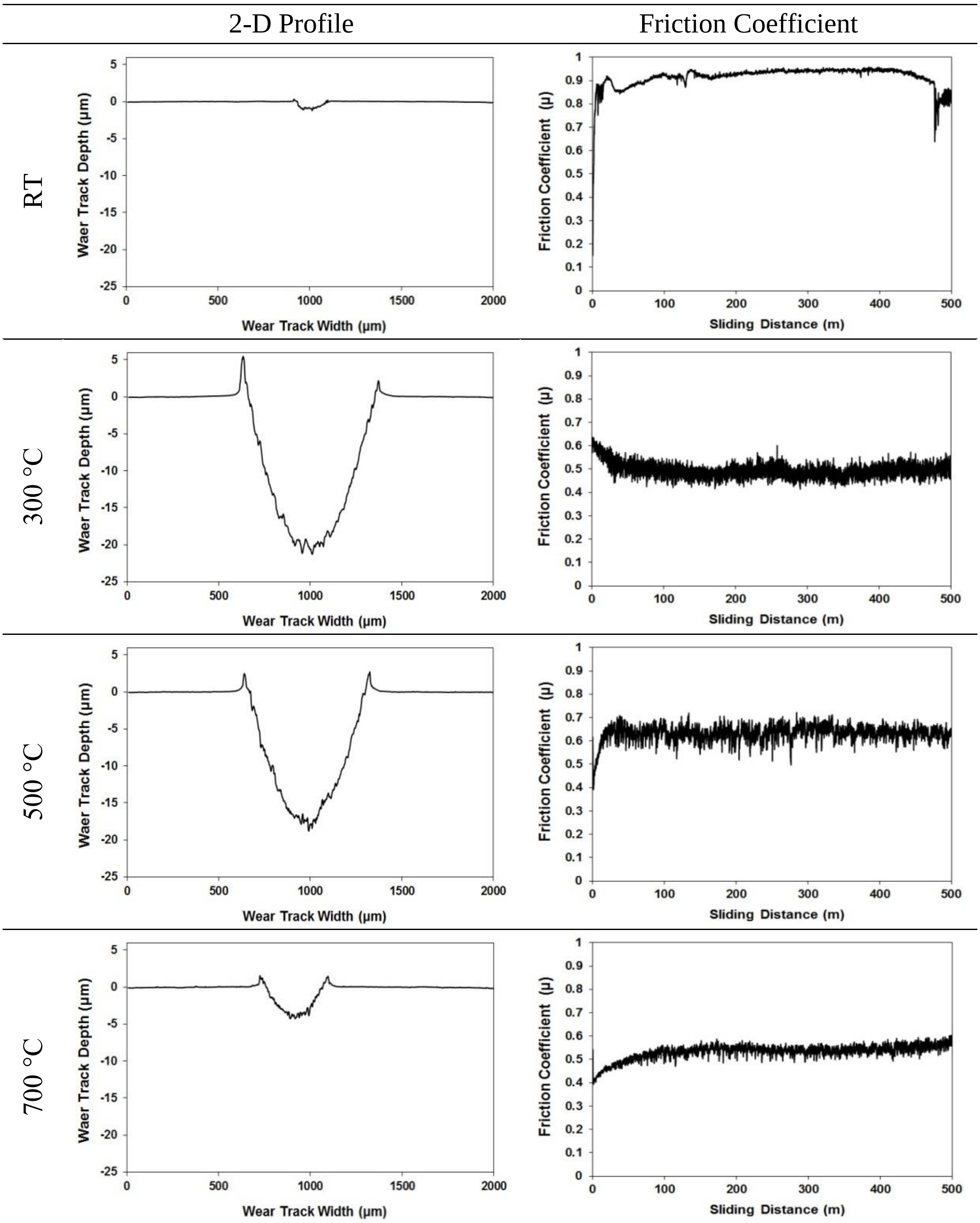

Figure B.1 : 2-D profiles of the wear tracks and friction coefficient curves of Stellite 12 coating tested at RT, 300, 500 and 700 °C.

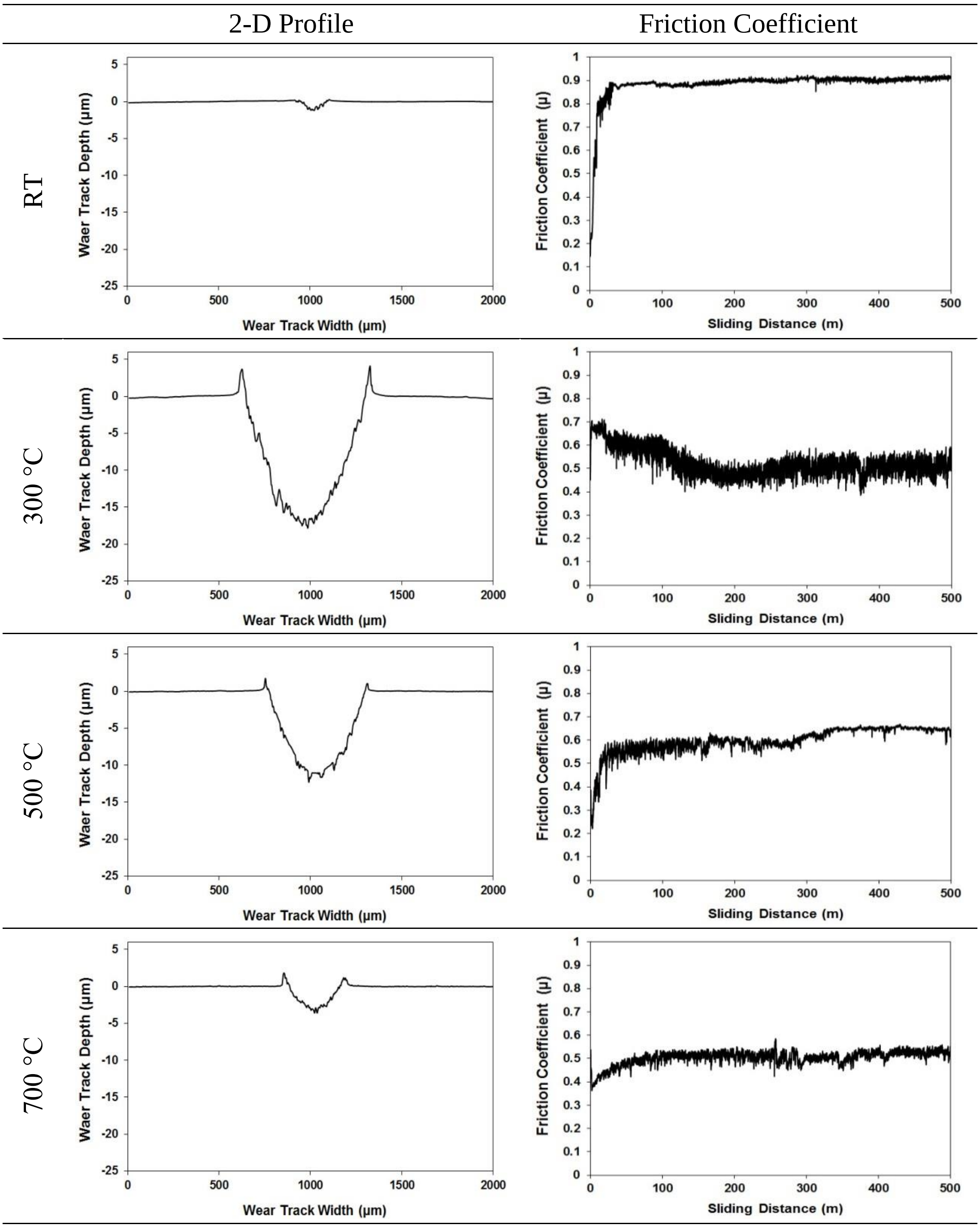

Figure B.2 : 2-D profiles of the wear tracks and friction coefficient curves of Stellite 12+2 wt% Mo coating tested at RT, 300, 500 and 700 °C.

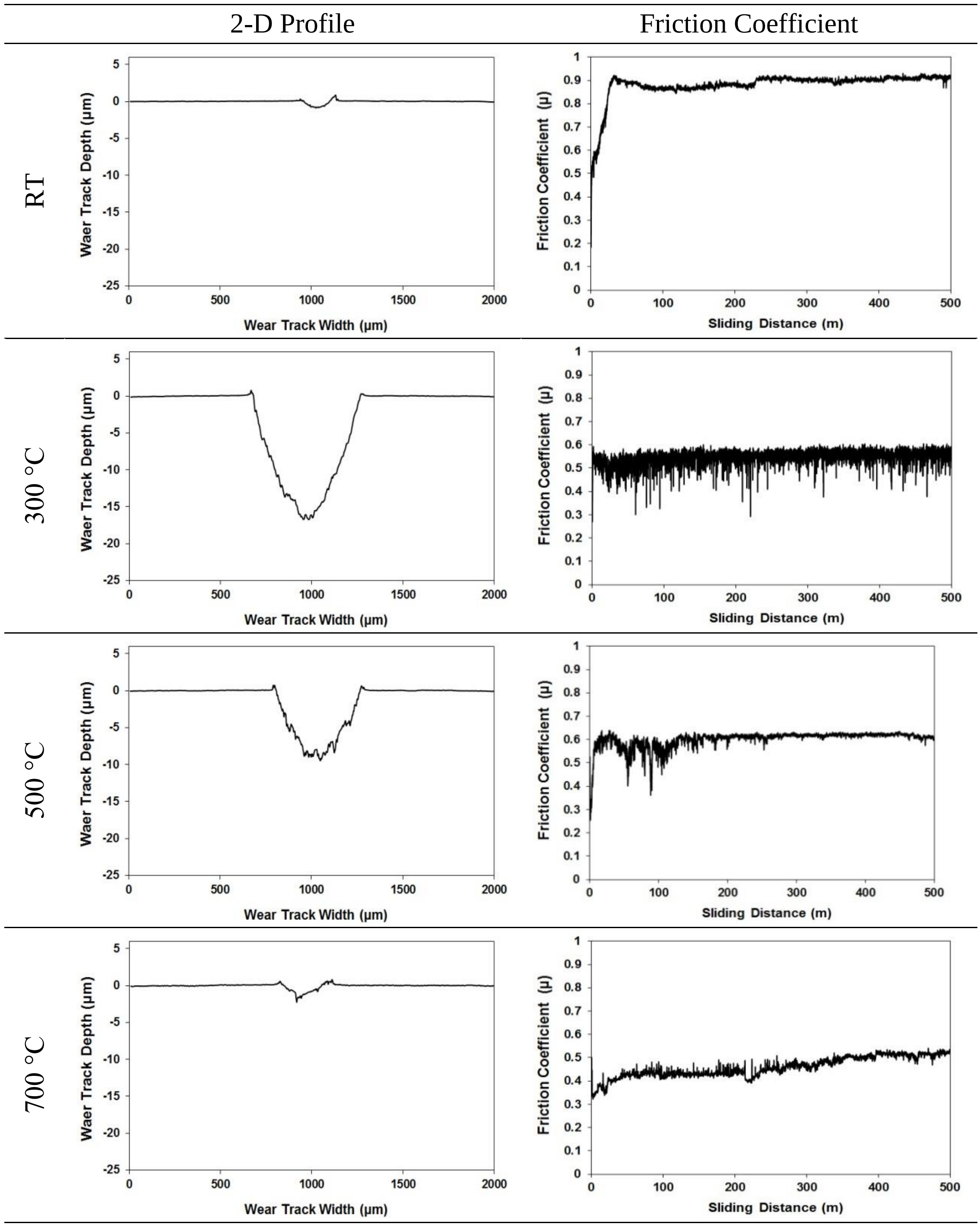

Figure B.3 : 2-D profiles of the wear tracks and friction coefficient curves of Stellite 12+6 wt% Mo coating tested at RT, 300, 500 and 700 °C.

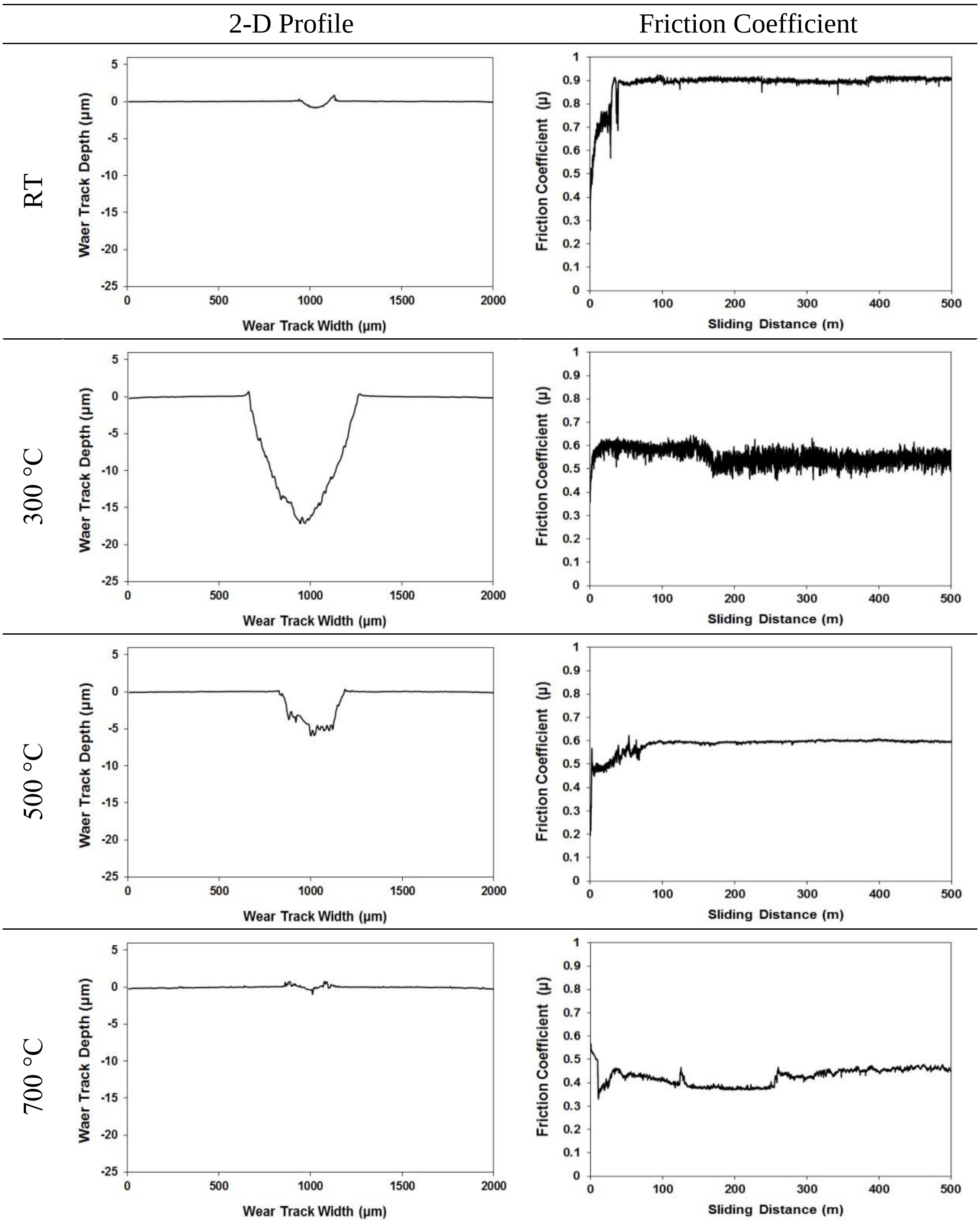

Figure B.4 : 2-D profiles of the wear tracks and friction coefficient curves of Stellite 12+10 wt% Mo coating tested at RT, 300, 500 and 700 °C.

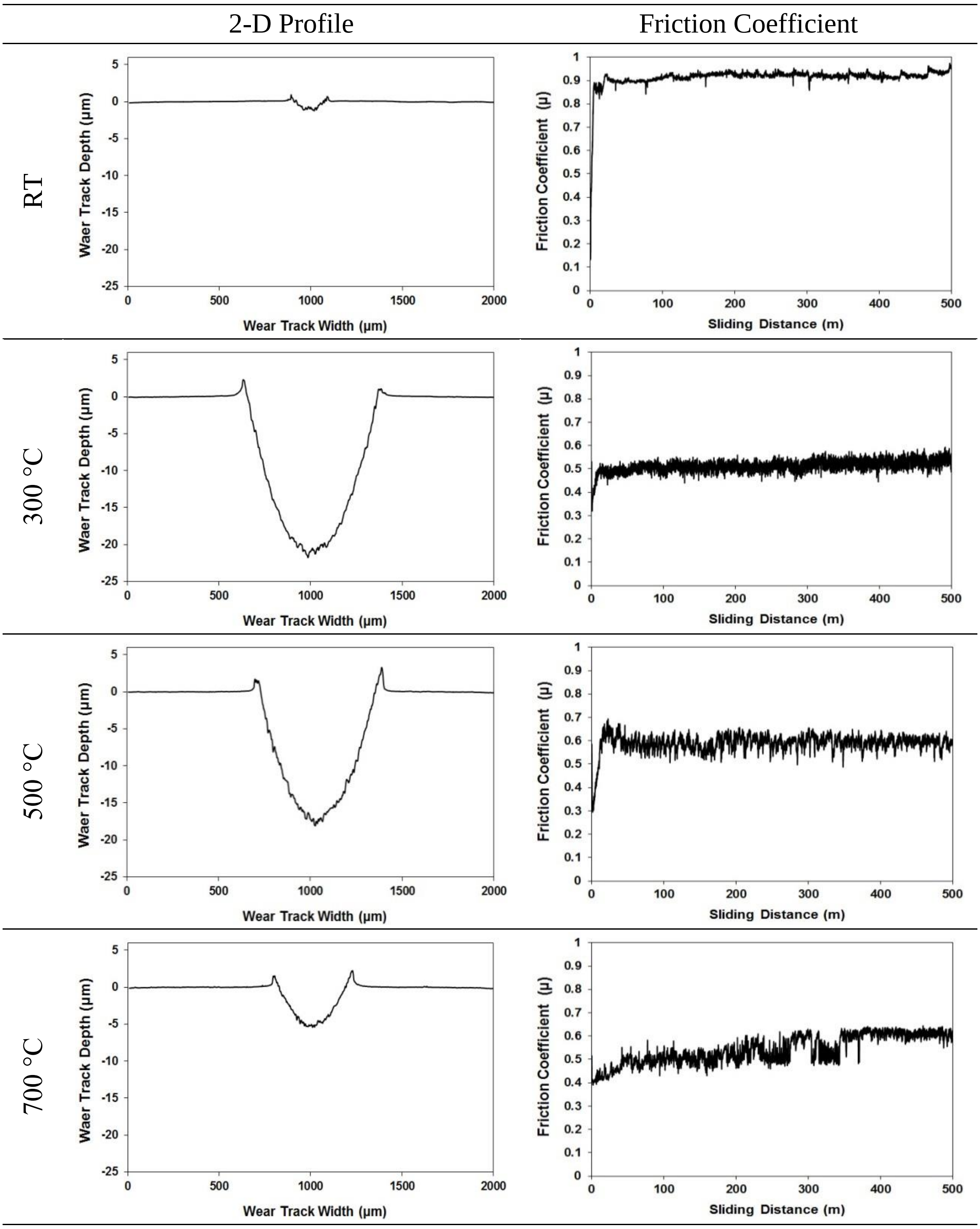

Figure B.5 : 2-D profiles of the wear tracks and friction coefficient curves of Stellite 12+2 wt% Ni coating tested at RT, 300, 500 and 700 °C.

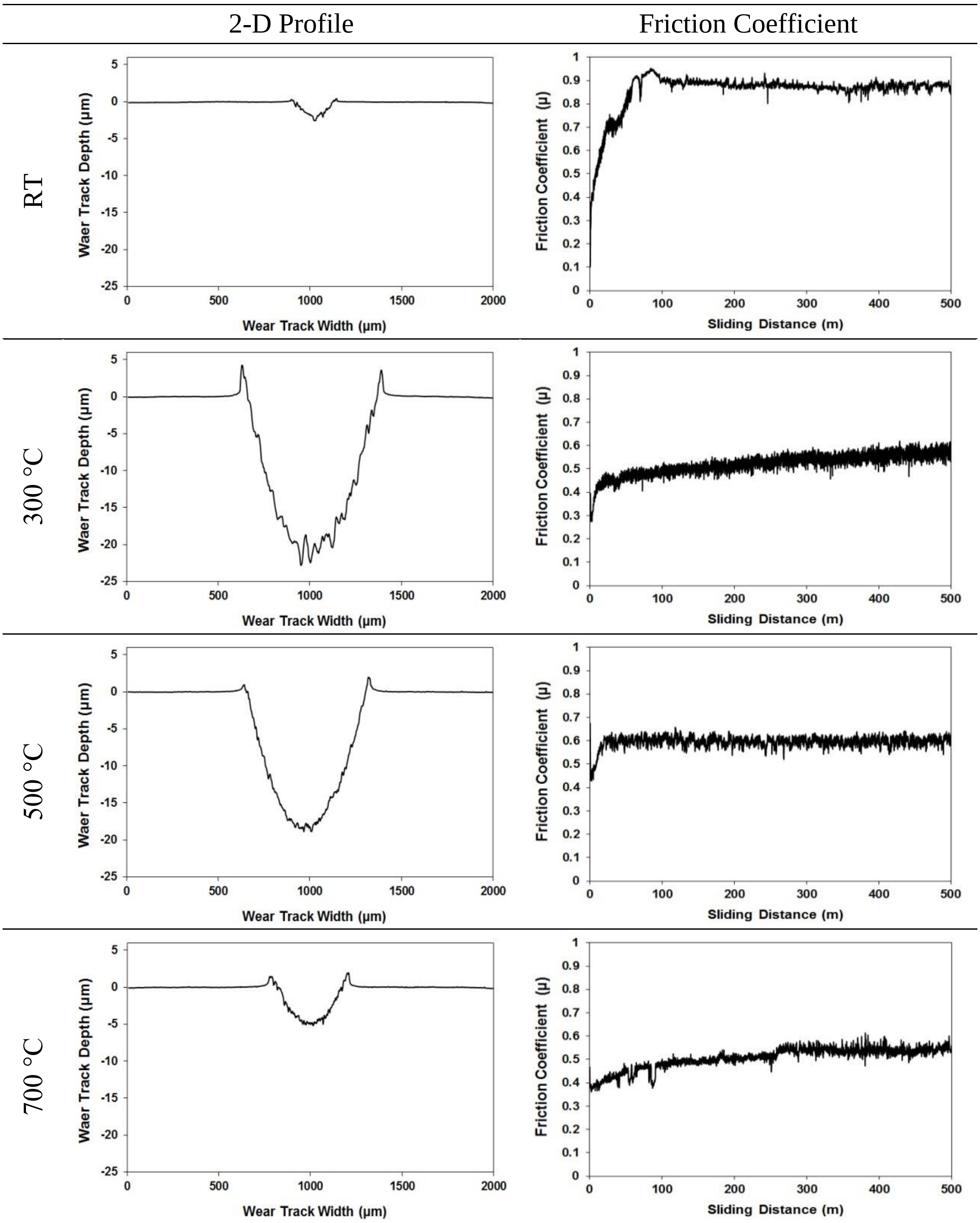

Figure B.6 : 2-D profiles of the wear tracks and friction coefficient curves of Stellite 12+6 wt% Ni coating tested at RT, 300, 500 and 700 °C.

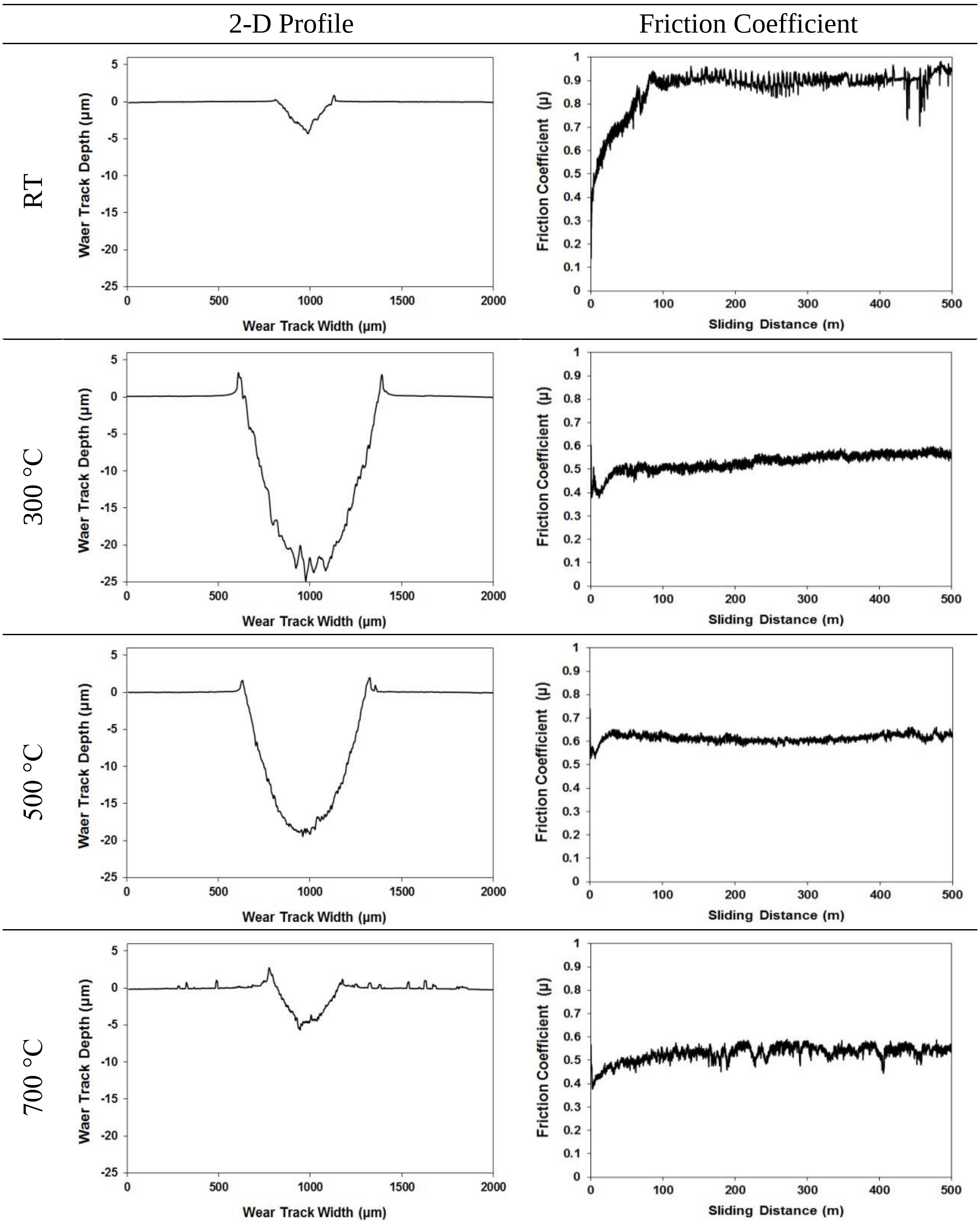

Figure B.7 : 2-D profiles of the wear tracks and friction coefficient curves of Stellite 12+10 wt% Ni coating tested at RT, 300, 500 and 700 °C.

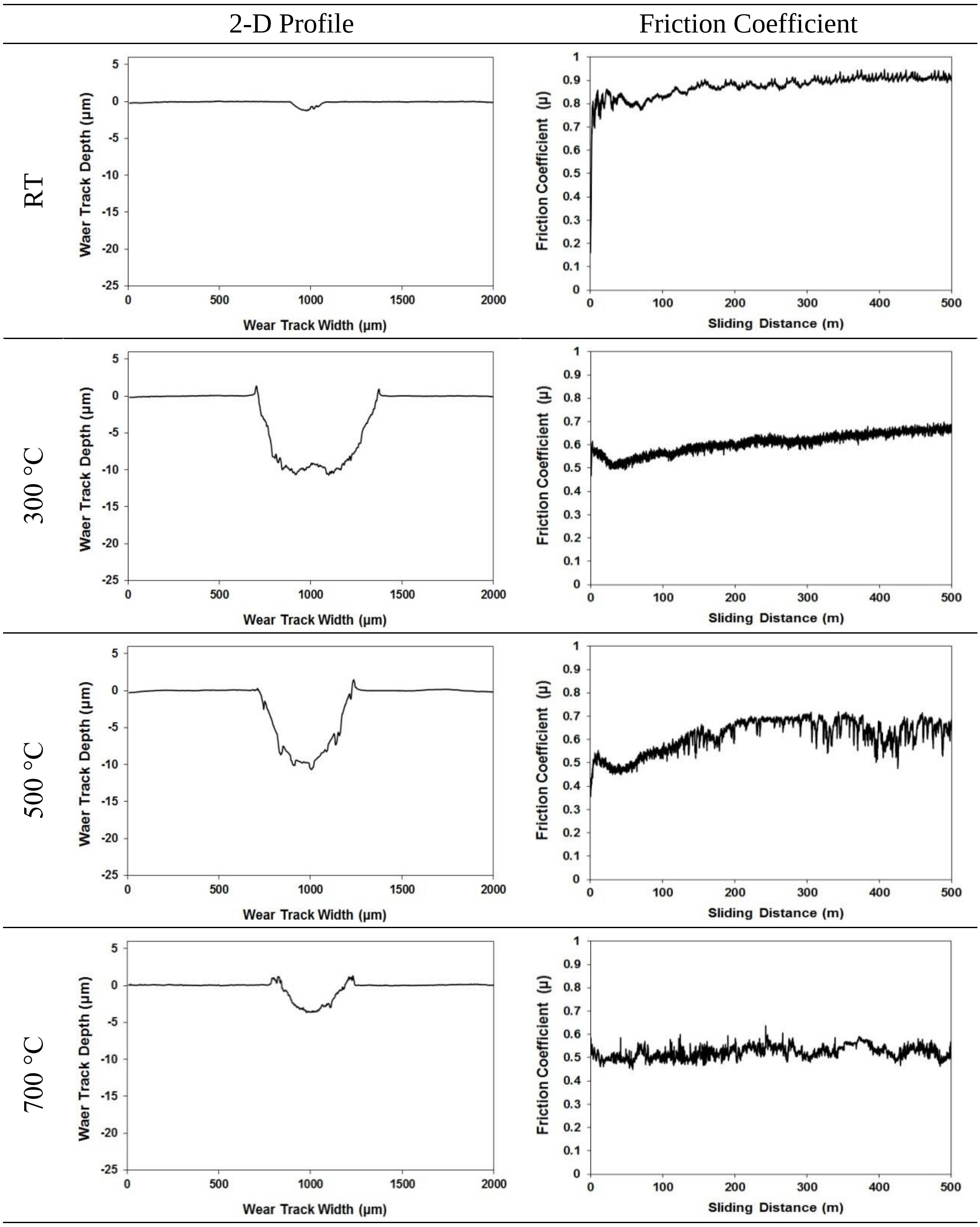

Figure B.8 : 2-D profiles of the wear tracks and friction coefficient curves of Stellite 12 + 2 vol% WC/W_2C coating tested at RT, 300, 500 and 700 °C.

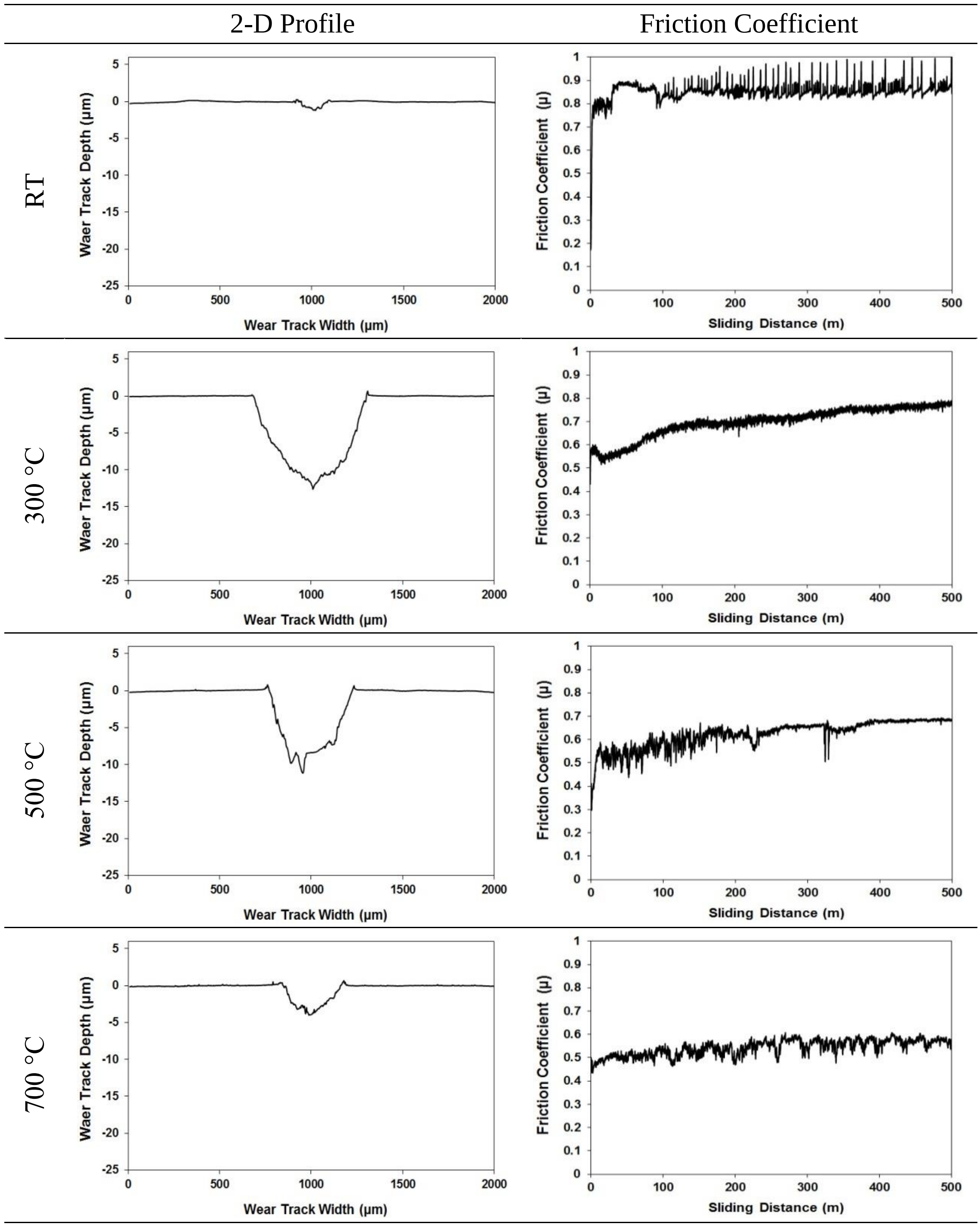

Figure B.9 : 2-D profiles of the wear tracks and friction coefficient curves of Stellite 12 + 6 vol% WC/W_2C coating tested at RT, 300, 500 and 700 °C.

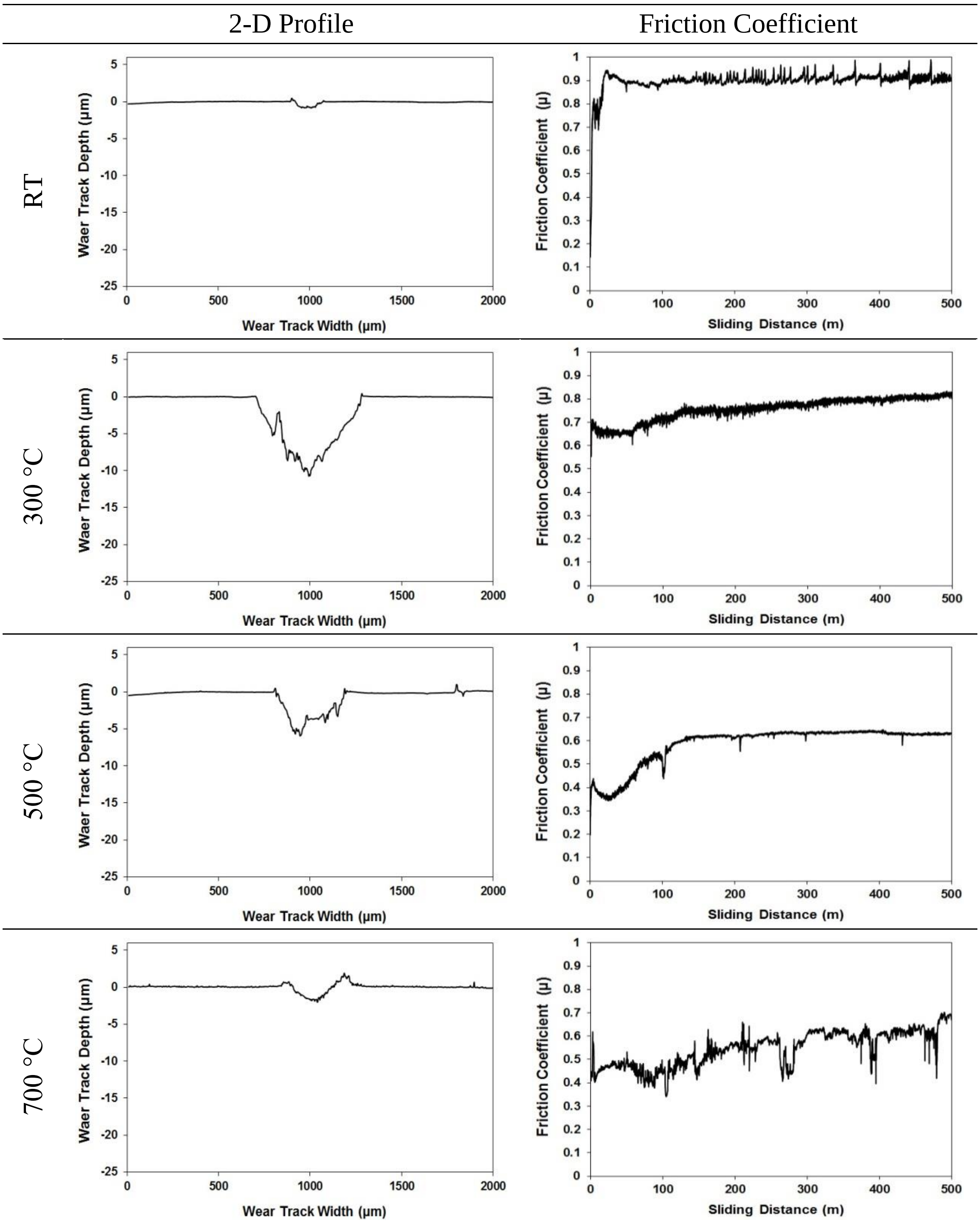

Figure B.10 : 2-D profiles of the wear tracks and friction coefficient curves of Stellite 12+10 vol% WC/W_2C coating tested at RT, 300, 500 and 700 °C.

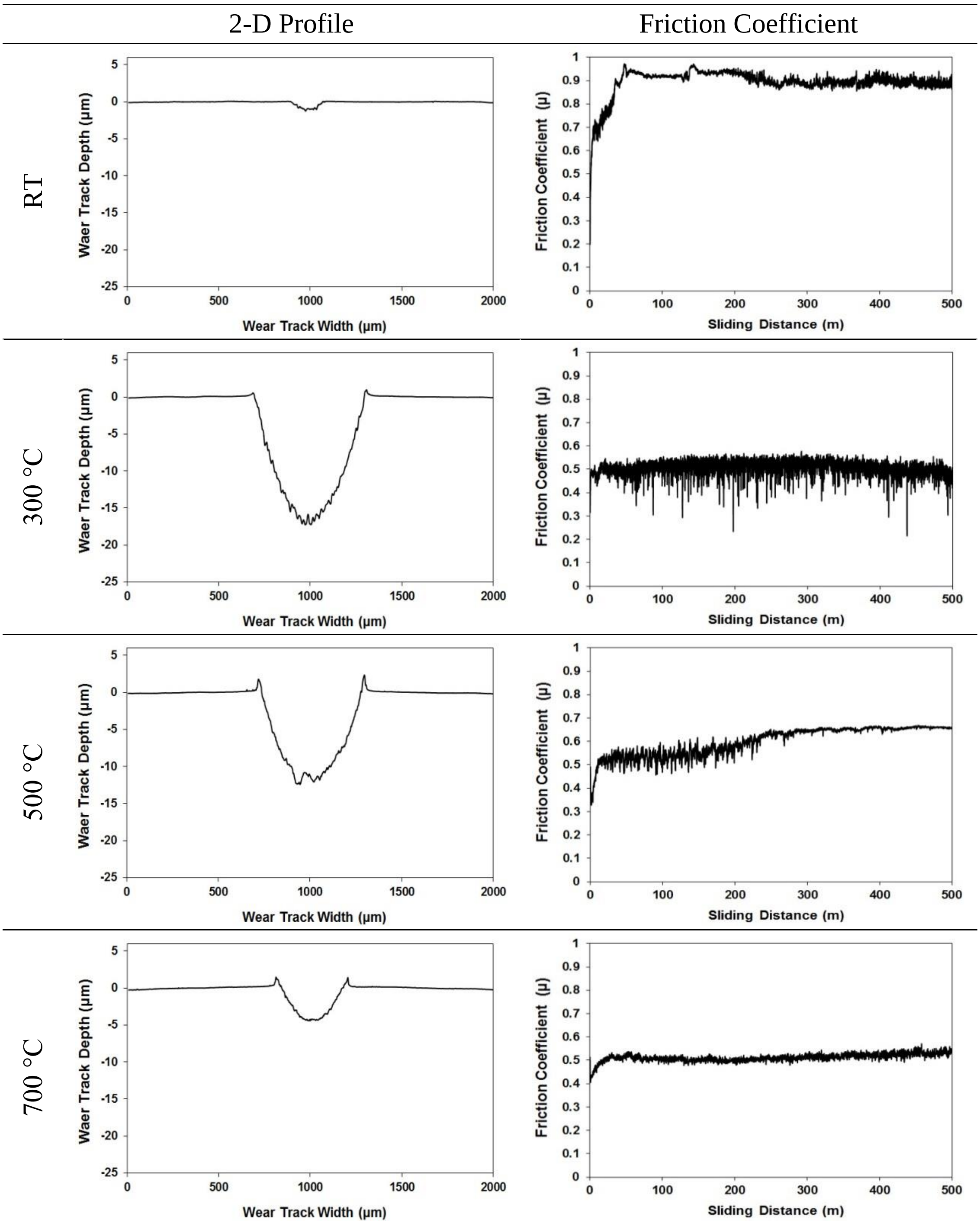

Figure B.11 : 2-D profiles of the wear tracks and friction coefficient curves of Stellite 12+2 vol% TiC coating tested at RT, 300, 500 and 700 °C.

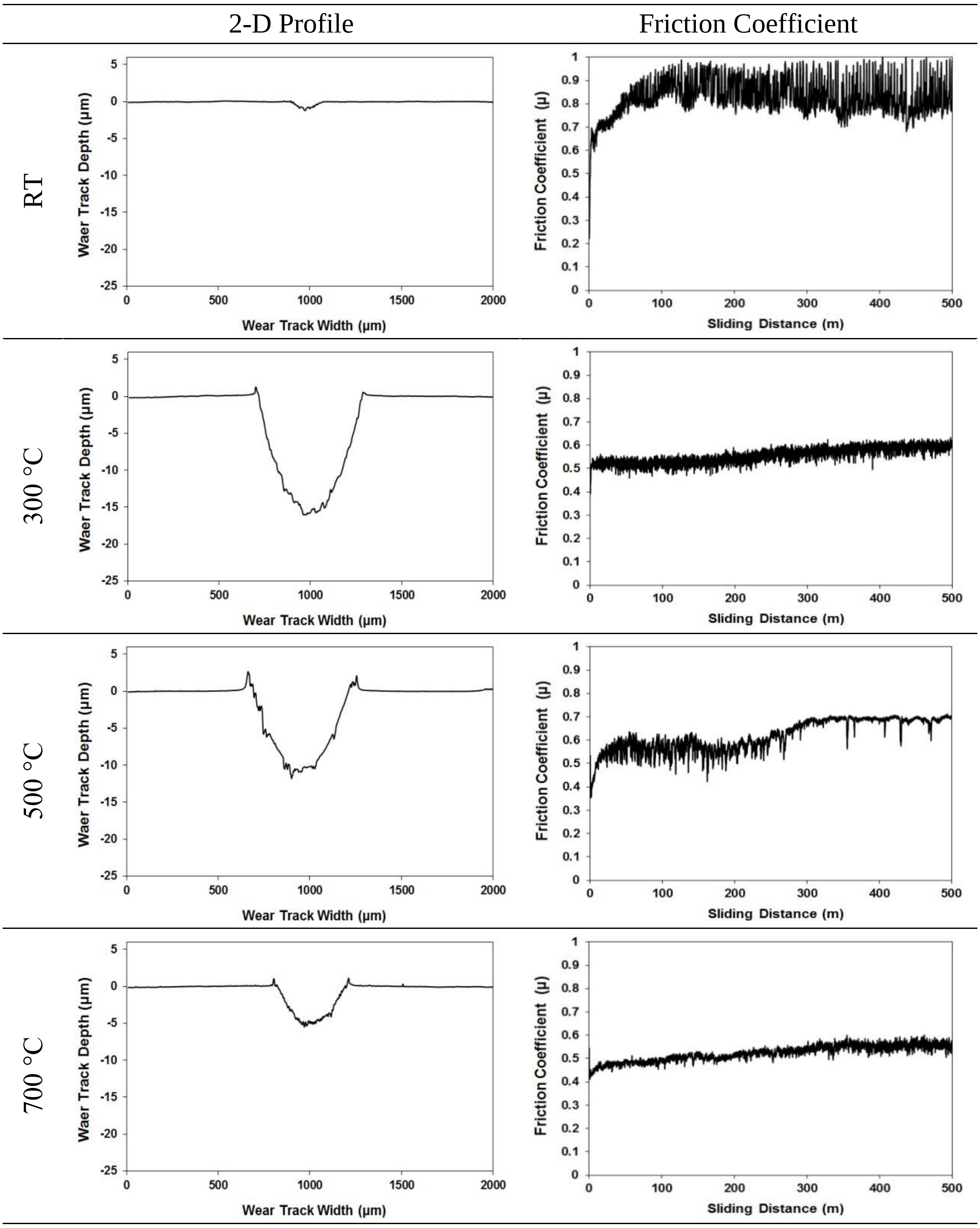

Figure B.12 : 2-D profiles of the wear tracks and friction coefficient curves of Stellite 12+6 vol% TiC coating tested at RT, 300, 500 and 700 °C.

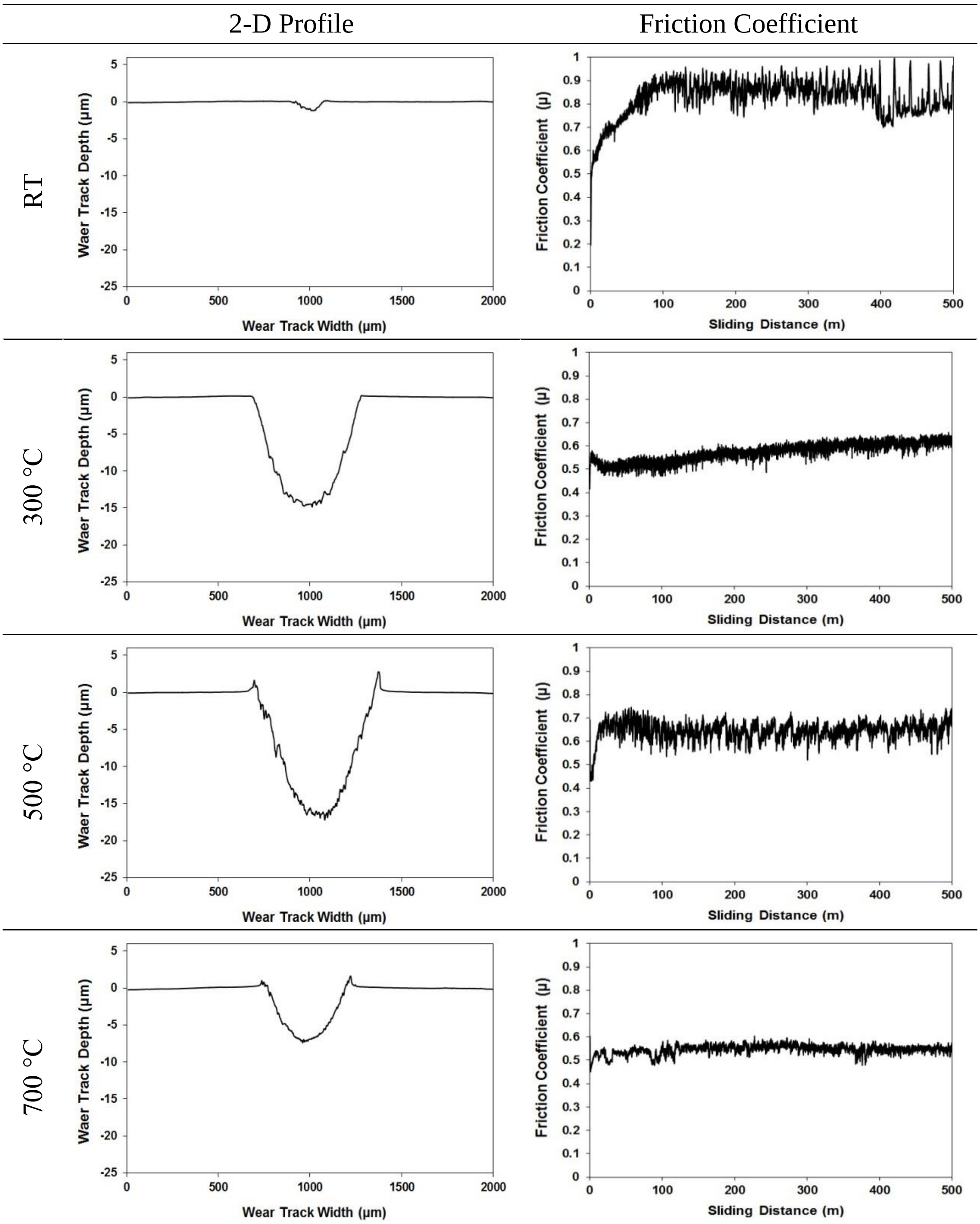

Figure B.13 : 2-D profiles of the wear tracks and friction coefficient curves of Stellite 12+10 vol% TiC coating tested at RT, 300, 500 and 700 °C.

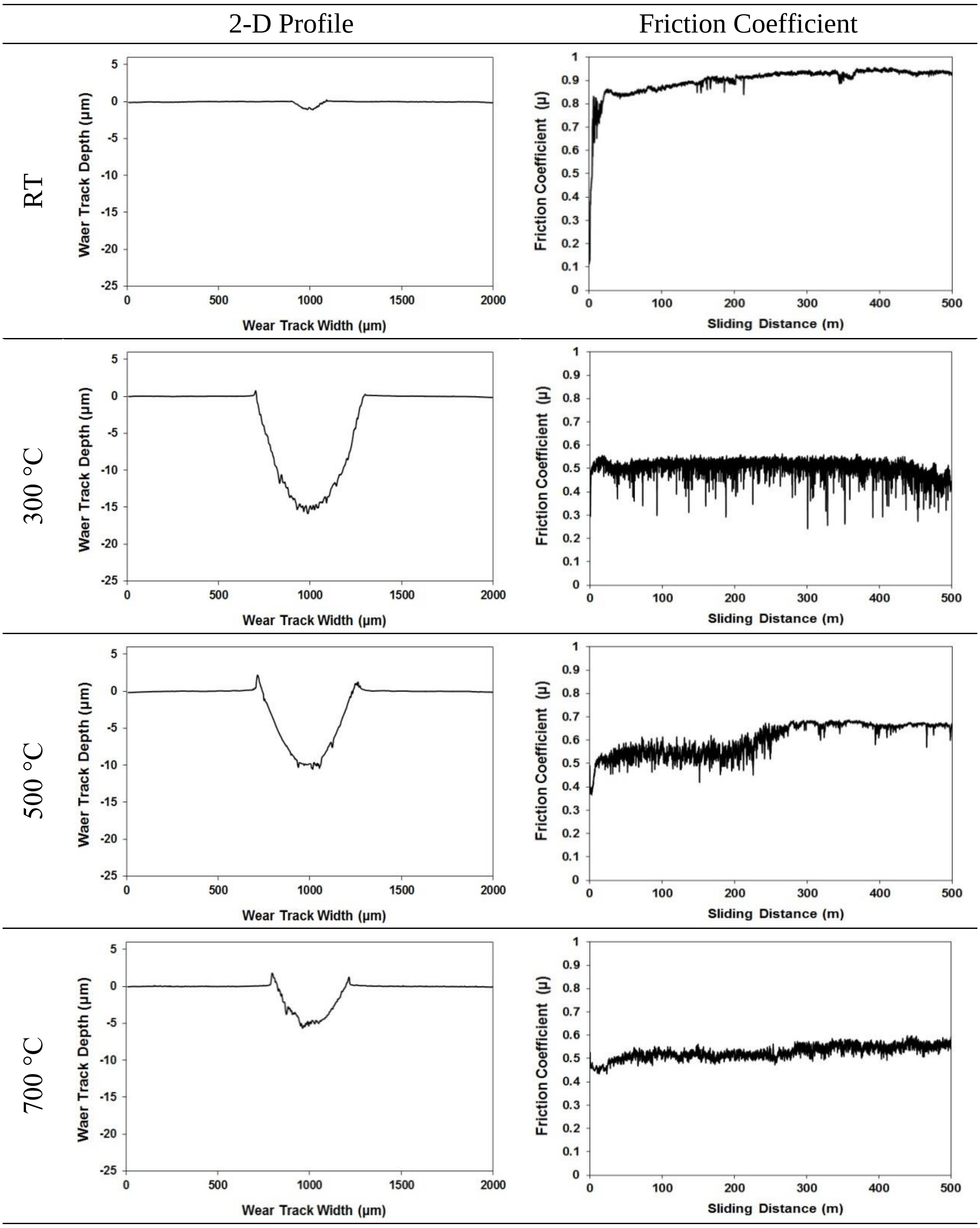

Figure B.14 : 2-D profiles of the wear tracks and friction coefficient curves of Stellite 12+2 vol% Cr_7C_3 coating tested at RT, 300, 500 and 700 °C.

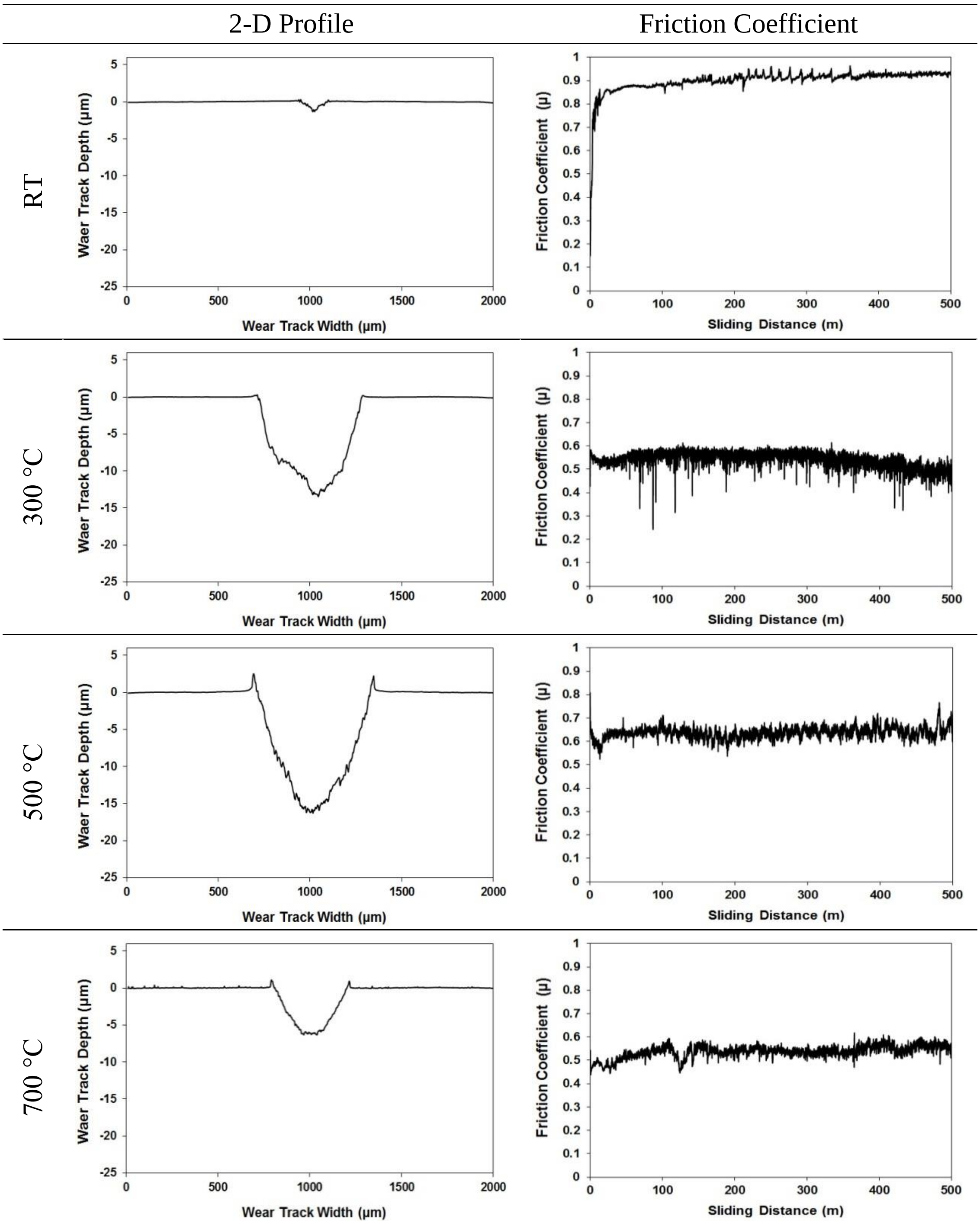

Figure B.15 : 2-D profiles of the wear tracks and friction coefficient curves of Stellite 12+6 vol% Cr_7C_3 coating tested at RT, 300, 500 and 700 °C.

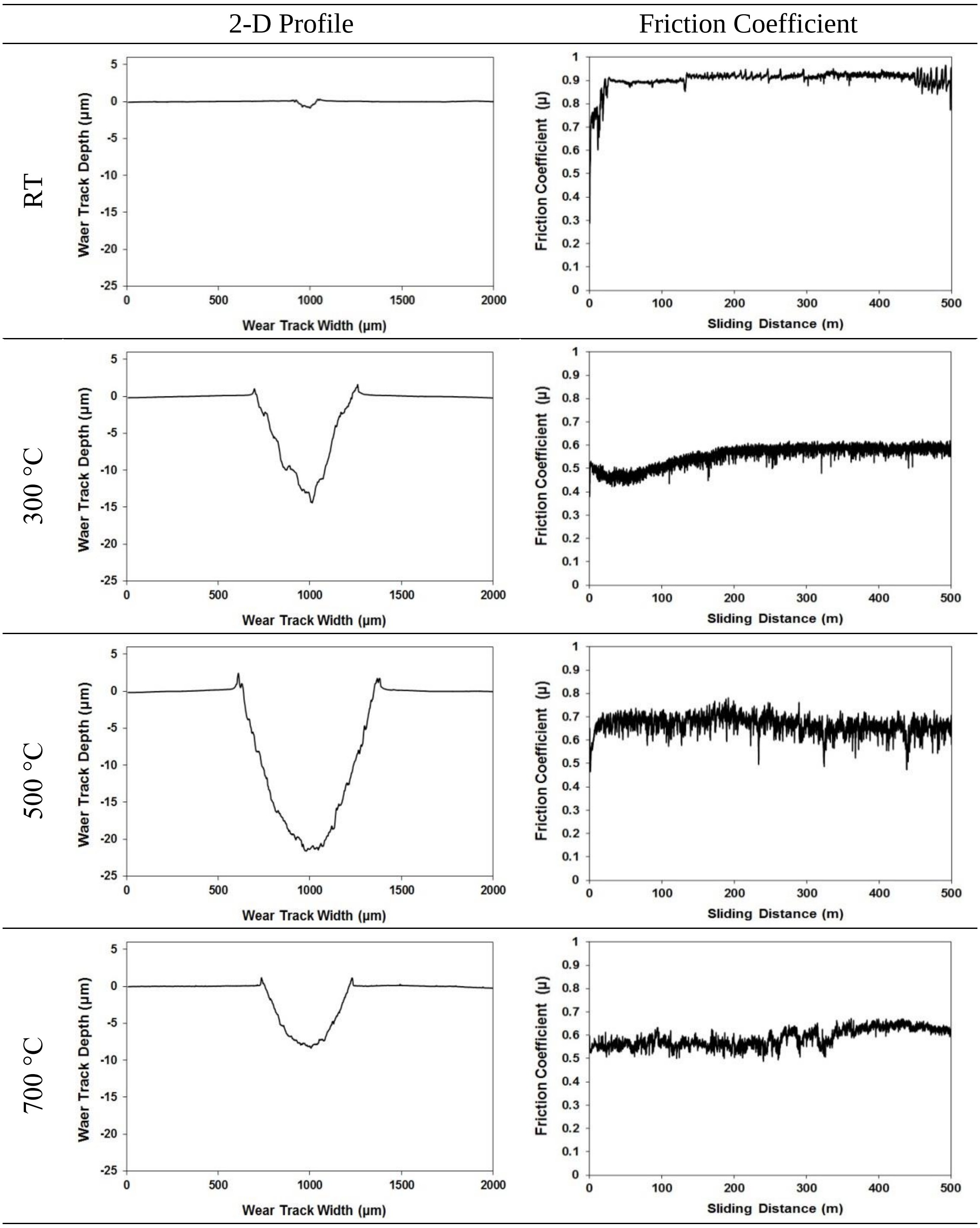

Figure B.16 : 2-D profiles of the wear tracks and friction coefficient curves of Stellite 12+10 vol% Cr_7C_3 coating tested at RT, 300, 500 and 700 °C.

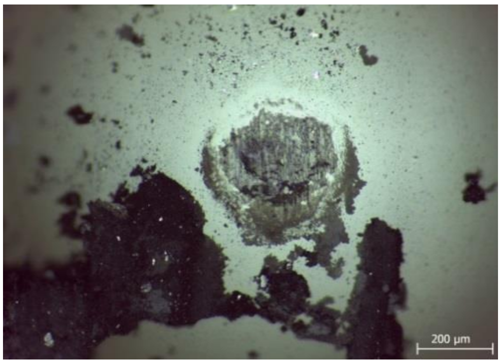

RT

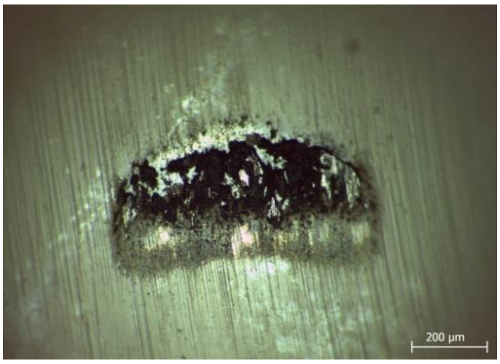

300 °C

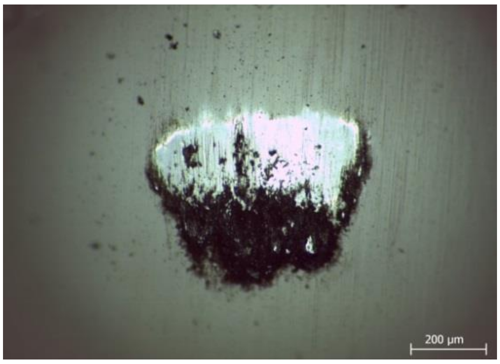

500 °C

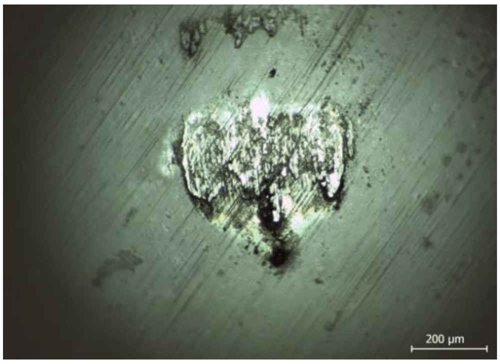

700 °C

Figure B.17 : Corresponding contact surface appearances of the Al_2O_3 ball after the wear testing of Stellite 12+10 vol% WC/W_2C coating.

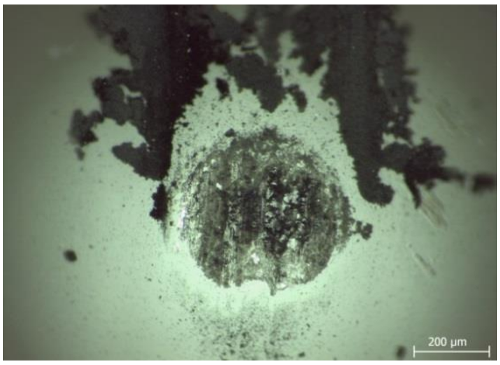

RT

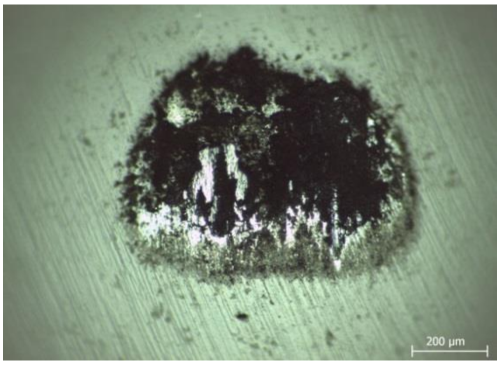

300 °C

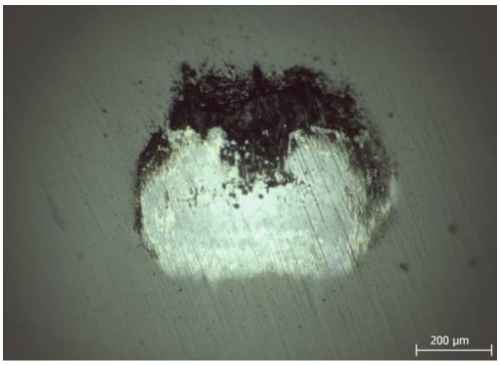

500 °C

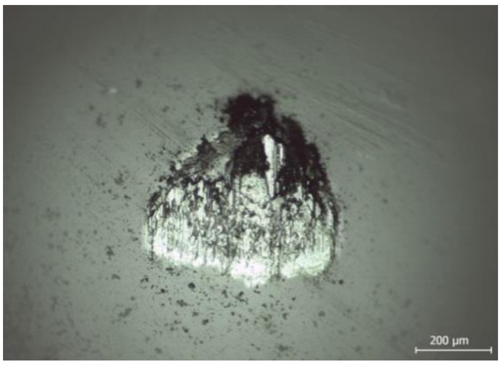

700 °C

Figure B.18 : Corresponding contact surface appearances of the Al_2O_3 ball after the wear testing of Stellite 12+10 vol% TiC coating.

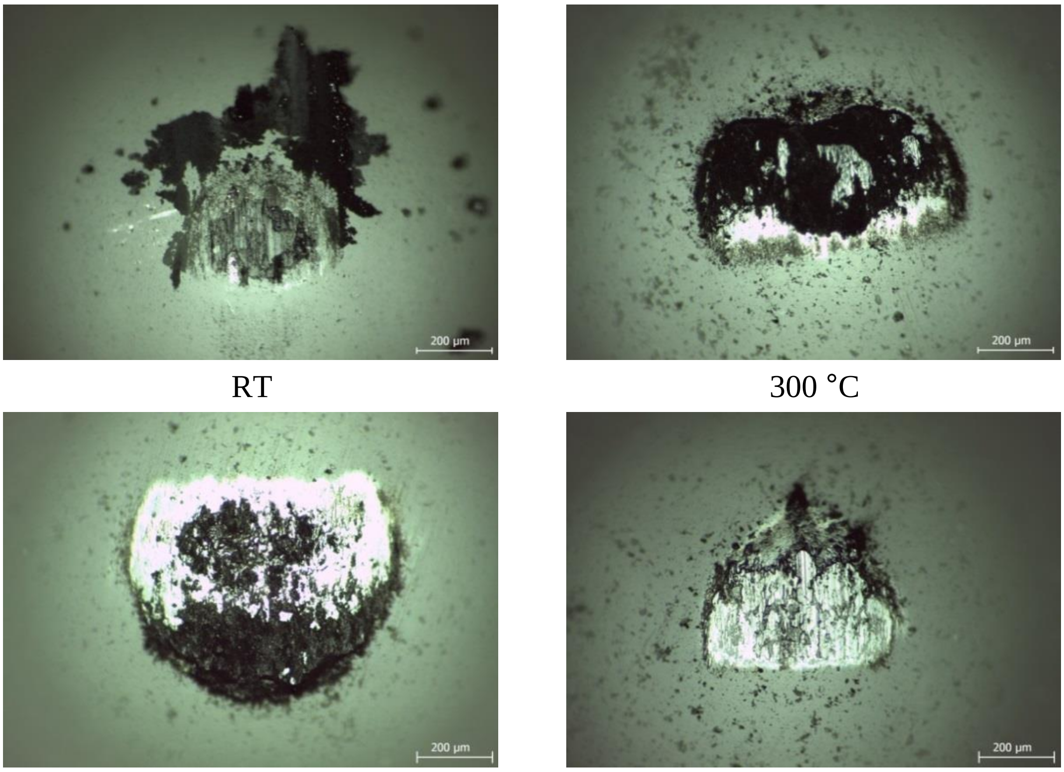

RT 300 °C

500 °C 700 °C

Figure B.19 : Corresponding contact surface appearances of the Al_2O_3 ball after the wear testing of Stellite 12+10 vol% Cr_7C_3 coating.

CURRICULUM VITAE

Name Surname: Amir Motallebzadeh

Place and Date of Birth: Tabriz, 31 January 1981

E-Mail: motallebzadeha@gmail.com

Address: Metallurgical and Materials Engineering Department
Chemical and Metallurgy Faculty
ITU Ayazaga Campus, Maslak 34469
Istanbul

B.Sc.: 1999-2003
University of Tabriz
Ceramic Engineering

M.Sc.: 2003-2006
University of Tehran
Materials and Metallurgical Engineering

PUBLICATIONS, PRESENTATIONS AND PATENTS ON THE THESIS:

Journal Articles (Covered by SCI)

- **Motallebzadeh, A.,** Atar, E. and Cimenoglu, H., (2015). Sliding wear characteristics of molybdenum containing Stellite 12 coating at elevated temperatures, *Tribology International*, Vol.91, 40-47.
- **Motallebzadeh, A.,** Atar, E. and Cimenoglu, H., (2014). The effect of nickel on sliding wear behaviour of cobalt-based hardfacing alloy at elevated temperature, *Archive of Materials Science and Engineering,* Vol.69, 81-87 (presented in IMSP’2014 conference).

International Conference Proceedings

- **Motallebzadeh, A.,** Atar, E. and Cimenoglu, H., “Microstructure and Tribological Properties of PTA Welded Stellite12 Coating on Steel Substrate”

Advances in Materials and Processing Technologies Conference (AMPT 2014), 16-20 November 2014, Dubai, UAE.

- **Motallebzadeh**, **A.**, Atar, E. and Cimenoglu, H., "Effect of Nickel on Sliding Wear Behavior of Cobalt Base Hardfacing Alloy at Elevated Temperature", 15th International Materials Symposium (IMSP'2014), 15-17 October 2014, Denizli, Turkey.

OTHER PUBLICATIONS, PRESENTATIONS AND PATENTS:

Journal Articles (Covered by SCI)

- **Motallebzadeh, A.,** Atar, E. and Cimenoglu, H., (2015). Evaluation of the Effect of Boride Layer Structure on the High Temperature Wear Behavior of Borided Steels", *Wear*, Vol 328-329, 110–114.
- Cimenoglu, H., Atar, E. and **Motallebzadeh, A.,** (2014). High Temperature Tribological Behaviour of Borided Surfaces Depending On the Phase Structure of the Boride Layer, *Wear*, Vol 309, 152–158.

International Conference Proceedings

- **Motallebzadeh, A.,** Dilektasli, E., Baydogan, M., Atar, E. and Cimenoglu, H., "Elevated Temperature Wear Behavior of Paste Borided 42CrMo4 and X20Cr13 Steels", The Second International Iron and Steel Symposium, 1-3 April 2015, Karabuk, Turkey.
- **Motallebzadeh, A.,** Yurekturk, Y., Bostanci, B., Atar, E. and Cimenoglu, H., "Nitriding Effect on High Temperature Wear Resistance of High Speed Tool Steels", The Second International Iron and Steel Symposium, 1-3 April 2015, Karabuk, Turkey.
- **Motallebzadeh, A.,** Dilektasli, E., Cimenoglu, H., and Atar, E., "High Temperature Tribological Behavior of 4140 and 1050 Steels", Innovative Materials and Structures Technologies Conference (METECH '13), 11-14 September 2013, Istanbul, Turkey.
- Dinc, H., **Motallebzadeh**, **A.**, Baydogan, M. and Cimenoglu, H., "Thermochemical Boriding of Inconel 718 Superalloy", IJAS Conference, June 2013 Prague, Czech Republic.